



HAL
open science

The effect of a partial nanocrystallization on the transport properties of amorphous/crystalline composites

Amani Tlili

► **To cite this version:**

Amani Tlili. The effect of a partial nanocrystallization on the transport properties of amorphous/crystalline composites. Material chemistry. Université de Lyon, 2017. English. NNT : 2017LYSE1322 . tel-01772887

HAL Id: tel-01772887

<https://theses.hal.science/tel-01772887>

Submitted on 20 Apr 2018

HAL is a multi-disciplinary open access archive for the deposit and dissemination of scientific research documents, whether they are published or not. The documents may come from teaching and research institutions in France or abroad, or from public or private research centers.

L'archive ouverte pluridisciplinaire **HAL**, est destinée au dépôt et à la diffusion de documents scientifiques de niveau recherche, publiés ou non, émanant des établissements d'enseignement et de recherche français ou étrangers, des laboratoires publics ou privés.



N° d'ordre NNT : xxx

THÈSE DE DOCTORAT DE L'UNIVERSITÉ DE LYON

opérée au sein de

l'Université Claude Bernard Lyon 1

École Doctorale ED34

Matériaux

Spécialité de doctorat : Physique de la matière condensée

Discipline : Physique

Soutenue publiquement le 21/12/2017, par :

Amani Tlili

The effect of a partial nanocrystallization on the transport properties of amorphous/crystalline composites

Devant le jury composé de :

De Boissieu Marc, Directeur de recherche CNRS, SIMaP

Monaco Giulio, Professeur, Université de Trento

Blandin Jean-jacques, Professeur, SIMaP

Chapuis Pierre Olivier, Chargé de recherche CNRS, Insa de Lyon

Vouagner Dominique, Maître de conférence, UCBL

Giordano Valentina, Chargée de recherche CNRS, Institut Lumière Matière

Tanguy Anne, Professeur, Insa de Lyon

Pailhès Stéphane, Chargé de recherche CNRS, Institut Lumière Matière

Rapporteur

Rapporteur

Examineur

Examineur

Examinatrice

Directrice de thèse

Co-directrice de thèse

Invité

Remerciement

Je n'aurais jamais pu faire seule l'ensemble de ce travail de thèse, je suis donc reconnaissante à plusieurs personnes qui y ont contribué.

Tout d'abord, je tiens à remercier sincèrement mes deux directrices de thèse Valentina Giordano et Anne Tanguy, pour m'avoir aidée à avancer, m'avoir indiqué les bonnes routes à suivre durant ces trois ans avec beaucoup de rigueur scientifique d'enthousiasme et de bienveillance. J'ai énormément apprécié travailler avec vous au quotidien. Que ce soit sur le plan scientifique ou humain et je vous dois la majeure partie de ce que j'ai appris.

Je tiens aussi à exprimer ma gratitude à Marc De Boissieu et Giulio Monaco qui ont accepté d'évaluer ce manuscrit. Je remercie aussi Pierre Olivier Chapuis et Dominique Vouagner de prendre part à ce jury. Je tiens également à remercier vivement Jean Jacques Blandin qui a accepté de présider ce jury.

J'aimerais aussi remercier l'ensemble de l'Institut Lumière Matière qui m'a accueillie et où j'ai toujours pu trouver des personnes professionnelles et disponibles lorsque j'en avais besoin. Je remercie également le laboratoire SIMaP de Grenoble et le CEA LETI qui m'ont permis d'élaborer mes échantillons au sein de leurs locaux. Je tiens aussi à remercier le laboratoire LAMCOS ainsi que le PSMN de m'avoir permis d'effectuer des simulations numériques grâce à leurs machines de calcul. Je souhaiterais également remercier toutes les personnes des services de secrétariat pour leur aide dans les démarches administratives. Je remercie également la région Rhône-Alpes pour le financement de ce projet.

Je souhaiterais exprimer ma gratitude à tous les membres de l'équipe "Nano-matériaux pour l'énergie" de l'ILM. Merci de m'avoir généreusement encouragée et aidée pendant toutes mes répétitions de présentations ou pré-conférences. Vos conseils et vos remarques ont été primordiaux pour ma formation et m'ont toujours permis d'avancer.

Je voudrais remercier particulièrement Stéphane Pailhès qui ne faisait pas parti de l'encadrement officiel mais qui a participé d'une manière déterminante à me faire avancer dans ce travail. C'était une chance pour moi de travailler avec une personne aussi bienveillante et dont les idées sont toujours pertinentes. Merci pour tous les moments qu'on a pu passer ensemble, je n'oublierai pas tes messages d'encouragement et de soutien.

Je voudrais aussi remercier Régis Debord qui a été très présent pour moi pendant ces trois ans. Au-delà de son implication dans le développement et l'avancement de mes manipulations, ses conseils et ses remarques m'ont beaucoup aidé. Merci de m'avoir toujours encouragée et soutenue et pour toutes les discussions scientifiques (ou autres) qui m'ont beaucoup apporté.

Je remercie vivement Samy Merabia qui m'a formée à utiliser LAMMPS et qui a été très impliqué dans l'interprétation des résultats, toujours dans la bonne humeur. Mes remerciements vont également à Sébastien Gravier et à Pierre Noé pour m'avoir accueillie à plusieurs reprises et qui m'ont formée à la préparation des échantillons.

Je remercie aussi Nicolas Blanchard, sans qui nous n'aurions pas eu de si jolies images TEM et Remy Fulcrand pour avoir gentiment accepté de m'aider à réaliser les gravures sous HF.

Je voudrais aussi souligner le travail remarquable de Jean Yves Raty qui nous a fourni les calculs de DFT ainsi que pour son implication dans le projet et pour les discussions fructueuses.

Mes remerciements vont également à Séverine Gomès et Ali Assy qui ont permis de réaliser les mesures de conductivité thermique au CETHIL.

Je remercie aussi les scientifiques de ligne ID28 à l'ESRF Luigi Paolasini et Alexei Bosak pour leur aide pendant les manip d'IXS ainsi que Ruben Vera du centre de diffractométrie de Lyon pour les mesures de diffraction des rayons X.

Je salue aussi tous les doctorants que j'ai pu croiser pendant cette aventure dans tous les laboratoires où j'ai pu travailler, et comme je risque d'en oublier quelques uns: merci à tous.

Je voudrais remercier tous mes amis qui m'ont beaucoup soutenue et aidée et qui se reconnaîtront. Merci à mes parents qui m'ont toujours poussée vers l'avant et donné la liberté de choisir. Enfin, merci à François dont le soutien moral et même les points de vue scientifiques ont été essentiels pendant ces trois ans de thèse.

Contents

Introduction	1
1 Glasses and composites: an overview	3
1.1 Physics of Glasses	4
1.1.1 The glassy state	4
1.1.2 Electronic transport in amorphous materials	7
1.2 Interest of composites	12
1.2.1 Thermal properties of nanocomposites	12
1.2.2 Electronic properties of nanocomposites	14
2 Experimental and theoretical methods	16
2.1 Experimental Methods	17
2.1.1 Sample Preparation	17
2.1.2 Physical Characterization	21
2.1.3 Transport Measurements	21
2.2 Numerical Study	29
2.2.1 Molecular Dynamics (MD)	30
2.2.2 Sample Preparation	30
2.2.3 Dynamical Matrix	31
2.2.4 Dynamical Structure Factor	32
2.2.5 Propagation of a Wave-Packet	32
2.2.6 Thermal conductivity calculations: Green-Kubo Method	33
3 Transport properties in metallic amorphous/crystalline composites	35
3.1 Bulk Metallic Glasses (BMG)	36
3.2 Sample Characterization	37
3.3 Thermal transport in metallic composites	38
3.4 Electrical contribution	39
3.5 Phonons contribution	41
3.5.1 The high frequency dynamics of the metallic glass	43
3.5.2 Phonon dynamics in amorphous/nanocrystalline composites	44
3.6 Total Thermal conductivity	47
3.7 Discussions and conclusion	49
4 Transport properties in chalcogenide amorphous/crystalline composites	51
4.1 Chalcogenide Glasses	52
4.1.1 GeTe compound	52

4.1.2	Carbon-doped GeTe (GeTeC)	53
4.1.3	Electronic properties	54
4.1.4	Thermal properties	54
4.1.5	Vibrational properties	55
4.1.6	PCM as potential thermoelectric materials	55
4.2	Sample preparation and characterization	56
4.2.1	Sample preparation	57
4.2.2	Structural characterization	57
4.3	GeTe Versus carbon-doped GeTe	60
4.3.1	Electrical properties	60
4.3.2	Thermoelectric potential of GeTeC nanocomposites	65
4.4	Effect of a partial crystallization	66
4.4.1	Electrical properties	67
4.4.2	Phonons transport	68
4.5	Conclusion	74
5	Thermal transport in amorphous/crystalline composites: numerical simulations	76
5.1	Density of Vibrational States	77
5.2	Dynamical Structure Factor	80
5.2.1	Longitudinal Modes	81
5.2.2	Transverse Modes	84
5.2.3	Discussion	86
5.3	Propagation of a Wave-Packet	87
5.4	Thermal conductivity	90
5.5	Summary	92
	Conclusion	94
	Bibliography	97

Introduction and aim of this work

The ever increasing need for multifunctional solutions has induced a growing interest in developing new structural materials with specific properties, able to push the limits of the traditional ones. Therefore, an active research playground has focused on developing novel strategies allowing to synthesize, characterize and produce novel materials. In the last few years, nanocomposites have aroused as a promising alternative to conventional materials, exploiting the combination of properties from the parent constituents in a single material. Their widespread is intimately linked to their multidisciplinary applications, such as aircraft devices, catalysis, data storage, bioseparation, and environmental treatment.

Understanding the physics of this new class of materials is an important and fundamental task, in order to expand our basic knowledge and predict new applications possibilities.

In this thesis, we focus on a precise kind of nanocomposite, where conductive crystalline nanoinclusions are embedded in a glassy host matrix. Such nanocomposites are expected to show a very low thermal conductivity, but a good electrical one, which make them good candidates for a number of applications such as thermal barriers or thermoelectric devices.

In this work, we present a fundamental investigation of the transport properties in composites made of nanocrystalline inclusions embedded in an amorphous matrix with different contrasts of properties between the two components. To this aim, we have performed a coupled experimental and theoretical investigation. For the experimental work, we have selected two composites, based on a metallic and a chalcogenide glass, where crystalline inclusions were directly obtained from the glass temperature-induced recrystallization. These composites are thus very easy to prepare, and do not require any complex material processing for obtaining nanocrystals embedded in an amorphous matrix. Simple controlled thermal protocols allow to tune the crystalline content and inclusion size.

The choice of these two families allows us to explore systems with very different electric and elastic contrast between amorphous and crystalline phase. While in the metallic glass composite, the two phases have almost no contrast of properties, in the chalcogenide glass composite both electric and elastic properties are very different. We go from an electrically insulating amorphous phase to a semiconducting crystalline phase, and the speed of sound increases with crystallization. Therefore, such choice allows us to investigate the effect of contrast of properties on transport mechanisms in nanocomposites.

For the theoretical work, we have investigated the changes in phonon dynamics and thermal conductivity while changing not only the crystalline inclusion size but also the elastic contrast between inclusion and matrix, in order to get a microscopic understanding of our experimental observations.

The structure of this manuscript is the following:

In chapter 1, we provide a background to the physical and transport properties of glasses in general with a focus on the most prominent theoretical models describing the electronic and thermal transport in

metallic and chalcogenide glasses, which are investigated in this thesis. Starting from those properties, we illustrate the interest of amorphous/crystalline nanocomposites and report the current state of the art of investigations of their electronic and thermal transport properties.

Chapter 2 is devoted to the presentation of all experimental and theoretical techniques used for the preparation of nanocomposites and their characterization. Chapter 3 and 4 present our experimental investigation of a metallic based and a chalcogenide based composite respectively, while theoretical results are reported in chapter 5. Finally, we conclude, summarizing all results and giving some perspectives for future work.

Chapter 1

Glasses and composites: an overview

1.1 Physics of Glasses

1.1.1 The glassy state

Glasses, or amorphous materials, are known since many centuries and today are ubiquitous in our daily life, exploited in various technological applications. They are solids characterized by a disordered atomic structure which lack the long range order, characteristic of crystals.

There are many ways to produce an amorphous system, from the application of pressure, to high energy milling, to sputtering. Still, the most common way is cooling a liquid with cooling rates high enough to avoid crystallization and freeze the system in a disordered structure [1].

Cooling down a liquid below its melting temperature can induce two different phenomena. The first process is the crystallization which takes place at the melting point T_m . The crystal is formed through a process of nucleation and growth, where atoms or molecules rearrange to form a long range periodic structure.

This transformation is a first order transition, characterized by discontinuities in thermodynamic quantities such as volume and entropy. This is schematically shown in Fig. 1.1 where the crystallization represents an abrupt drop of the volume occurring at T_m . However, if the cooling rate is high enough, the crystallization can be avoided and the liquid can be supercooled below T_m . By further lowering the temperature, the viscosity of the liquid increases and the system falls out of equilibrium until it eventually freezes in a solid disordered state. The temperature at which this happens is called glass transition temperature T_g and its value depends on the used cooling rate. The slower is the cooling rate, the lower is the glass transition temperature and the larger is the supercooled region (see Fig. 1.1).

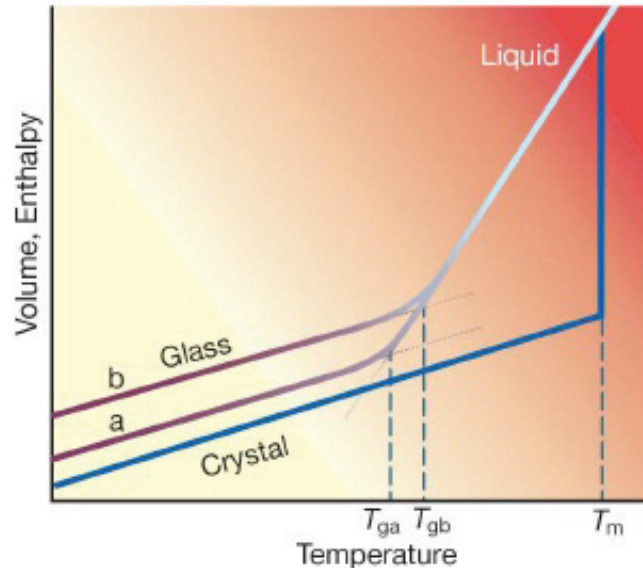


Figure 1.1: Evolution of the volume or enthalpy as a function of temperature at constant pressure. T_m denotes the crystallization temperature characterized by an abrupt contraction of the volume and T_g is the glass transition temperature around which the slope changes. T_{ga} and T_{gb} describe the effect of the cooling rate on the glass transition temperature, slower or faster, respectively [2].

Depending on the chemical composition, we distinguish many families of glassy materials such as oxide, chalcogenide, fluoride, bromide and metallic glasses. In the next sections we focus on presenting the

fundamental properties of two specific types of glasses, namely metallic and chalcogenide glasses which are the subject of our study. We describe more specifically the thermal properties and the electronic transport in such glasses. Indeed, the disordered structure substantially alters all physical properties, being at the basis of glassy-specific mechanisms in thermal and electronic transport.

1.1.1.1 Thermal properties

The thermal conductivity is the sum of two contributions, one coming from the electrons, k_{el} , and the other from the atomic vibrations, k_{at} .

The electronic contribution can be estimated using the Wiedemann-Franz law such as: $k_{el} = \frac{LT}{\rho}$, with $L = 2.45 \times 10^{-8} \text{ W } \Omega \text{ K}^{-2}$ the Lorenz number, T and ρ temperature and electrical resistivity respectively. It is important to remind here that the Lorenz number is not a universal constant. The validity of the electronic contribution to thermal conductivity via the Wiedemann-Franz law is in fact strongly dependent on the nature of the material and on its electronic band structure, and it is generally limited only to high temperature. More details will be given on this issue in the next chapters.

The atomic vibrations contribution is assured by quasi-particles called phonons, characterized by a wavevector q (or wavelength $\lambda = 2\pi/q$), an energy $E = \hbar\omega$ and a lifetime τ (or phonon broadening $\Gamma = 1/\tau$). In its lifetime, a phonon with velocity $v = \hbar\omega/q$ transports over its mean free path $l = v\tau$ a quantum of heat equal to its velocity times its energy.

Using the Boltzmann approach, the total vibrational contribution can be expressed as an integral over all phonon frequencies [3, 4]:

$$k_{at} = 1/3 \int_0^{\omega_{max}} C_v(\omega)v(\omega)^2\tau(\omega)g(\omega)d\omega \quad (1.1)$$

with $C_v(\omega)$ and $g(\omega)$ the phonon specific heat and density of states. The integration upper limit ω_{max} is defined for each phonon branch by the condition of density of states normalization in the first Brillouin zone: $\int_0^{\omega_{max}} g_j(\omega)d\omega = 1$, where $g_j(\omega)$ represents the contribution of the branch j to the density of states.

Such formulation, developed in the framework of the relaxation time approximation of the Boltzmann transport theory in crystalline systems, can still be used in amorphous systems, as it has been derived by Allen and Feldman [5, 6], provided that the calculation is limited to low energy phonons, which are not over-damped and can still be considered as propagative modes. When the phonon mean free path becomes comparable with the phonon wavelength, $l \approx \lambda/2$ (Ioffe-Regel limit), the phonon stops to be propagative and thermal transport becomes diffusive.

In this case Eq. 1.1 changes and can be written as:

$$k = \int C(\omega)D(\omega)g(\omega)d\omega \quad (1.2)$$

With $D(\omega)$ the phonon diffusivity. At small ω , when the Debye approximation can be used, and modes are still propagative, $D(\omega) = \frac{v(\omega)l(\omega)}{3}$ and Eq. 1.2 comes back to Eq. 1.1.

A striking feature of glasses is that they exhibit anomalous behaviors in some thermodynamic properties such as specific heat and thermal conductivity. These behaviors take place at low temperature and are markedly different from their crystalline counterparts.

Heat capacity

The first thermal anomaly common to all glassy materials consists in the different low temperature behavior of the specific heat (C_p). The first report dates back to 1971 and concerned glassy silica, compared to crystalline quartz [7]. C_p in crystals is predicted by the Debye model and its temperature dependence follows $\sim T^3$ at low temperature. As for glasses, C_p is found to increase much more slowly with temperature and can be described adding a linear term as:

$$C_p \sim aT + bT^3 \quad (1.3)$$

At very low temperature (≤ 1 K), $C_p(T)$ vary linearly with T. Glassy materials exhibit an excess of heat capacity around 10 K and present a bump in C_p/T^3 . A peak in C_p/T^3 is actually observed in crystalline materials as well but at higher temperature and is usually related to the effect of transverse acoustic vibrational excitations near the boundary of the first Brillouin zone.

Thermal conductivity

In a crystal the thermal conductivity (k) is dominated by the heat capacity and behaves as T^3 at very low temperatures. At higher temperatures, anharmonic phonon-phonon scattering processes settle in (Umklapp scattering), reducing the phonon mean free path and giving raise to a decrease of the thermal conductivity with T^{-1} , thus resulting in a peak, the so-called Umklapp peak.

In a glass, the situation is different: at low temperature (≤ 1 K) k shows a T^2 temperature dependence. Contrary to crystals no peak is observed in k , instead a plateau region occurs at ~ 10 K and k behaves approximately as T^2 , rather than T^3 .

The anomalous properties of k and C_p at low temperature were explained in the framework of the "Two level states" model [8] which suggests the existence of atoms or small groups of atoms which can tunnel between two configurations of very similar energy (two-level systems, TLS). The intrinsic structural disorder of glassy solids would produce a random distribution of these in terms of their asymmetry and tunneling parameters which is able to explain phenomenologically most of the low-temperature properties of glasses based on the scattering of low energy phonons from the TLS.

1.1.1.2 Vibrational anomalies

Historically, vibrational properties in glasses have been first explored by means of optical spectroscopy, giving access to optic modes, or neutron time of flight spectroscopy, allowing to measure the whole vibrational density of states.

Density of states measurements revealed the existence of a vibrational anomaly with respect to crystals: an excess of modes at an energy of ~ 1 THz, with respect to the predictions of the Debye model [9]. Such excess, called Boson Peak (BP) is ubiquitous in all glasses, and has been related to the thermal anomalies presented above, and a strong scattering of sound waves [10, 11].

Its origin has long been matter of debate and many theories have been developed, identifying the excess modes with quasi-localized soft-modes [12, 13], or ascribing the scattering to elastic constants heterogeneities on the nanometer scale [14, 15, 16, 17].

The most recent experimental results indicate that the BP is nothing else than the disordered-modified transverse acoustic Van Hove singularity of the corresponding solid phase and no excess of modes is present [18]. Due to this long-standing open question, great interest has been devoted to the experimental investigation of phonon dynamics in the THz range. Inelastic neutron scattering measurements of the collective dynamics in a simple NiZr metallic glass have played a pioneering role [19]. In these exper-

iments, it was possible to prove the existence of a pseudo-Brillouin-zone with clear zone boundaries at an exchanged momentum q close to half the position of the first sharp diffraction peak.

However, properties of the collective excitations such as the low- q dispersion relation, the wave-vector and energy transfer dependence of the velocity of sound remained still inaccessible. This was because of the kinematic constraints of inelastic neutron scattering, making it impossible to measure in the first zone collective excitations with high speed of sound, as is typically the case of glasses. This problem was solved with the development of Inelastic X-ray scattering (IXS) technique which, being free from any kinematic constraint, has made accessible the low- q low-energy region.

For the first time, the acoustic phonons responsible for the BP, as well as for the plateau of the thermal conductivity, could be investigated. A strong scattering regime, with a sound attenuation proportional to q^4 was expected, to explain the thermal conductivity plateau. Scopigno et al [20] provided the first measurements on a glassy $\text{Ni}_{24}\text{Zr}_{76}$ in the region, where the acoustic excitations are still very well defined. In this work, it was reported that at low q , the sound attenuation exhibits a q^2 behavior, with no hint of a possible transition towards a q^4 dependence.

Thanks to the continuous improvement of IXS, the q^4 behavior was finally reported in a number of very different glasses, from glycerol [21], to silica [22], to sorbitol [23], and found to be systematically accompanied by an anomalous bending of the sound velocity, dubbed "negative dispersion". This phenomenology could be reproduced as well in molecular dynamics simulations of a Lennard-Jones glass [24], and was later ascribed to a modification of the whole dynamics due to nanometric elastic heterogeneities [25, 26, 27, 28]. Similar observations were reported for many metallic glasses, where however a positive rather than negative dispersion of the sound velocity was found, e.g. a hardening with respect to the macroscopic value [29, 30]. In this case, it was explained with a microstructural model for metallic glasses, based on the coexistence of strongly and weakly bonded regions, e.g., once again, the existence of elastic heterogeneities on the nanometric scale.

1.1.2 Electronic transport in amorphous materials

Electron transport in disordered materials is still considered as one of the most challenging topics in condensed matter physics contrary to the case of crystals, where the description of transport can be exactly done by exploiting the long range order of the structure. The periodicity present in crystals allows to describe electrons as Bloch waves. The electrical resistivity is then due to the scattering of electrons from crystalline imperfections, such as impurities, vacancies, dislocations, or from other electrons or phonons. Such description works very well as far as the crystal can be considered only weakly disordered. When however disorder is heavily present, the Bloch theorem fails. In disordered solids, the lack of periodicity and long range order makes a Bloch-based description impossible. Many theories have been proposed for interpreting electric transport in amorphous materials, which depend on the localized character of conduction electrons, as well as on the strength of the electron-phonon scattering. Here we present the theoretical models able to describe the systems investigated in our work, e.g. a specific Zr-based metallic glass and chalcogenide glasses.

1.1.2.1 Metallic glasses

Mizutani provided a classification of metallic glasses into five groups based on their electronic and magnetic properties [31, 32]. Non-magnetic metallic glasses were classified as groups 4 and 5, the former having the Fermi level in the d band, the latter in the sp band. We focus now on metallic glasses of group 4, our sample belonging to this one.

For these systems, the electronic transport can be described by the Baym-Meisel-Cote model based on the Boltzmann transport equation, which explicitly takes into account the electron-phonon interaction contribution to the electrical resistivity [33]. The temperature dependence of this latter can be approximated as:

$$\rho = [\rho_0 + \Delta\rho(T)] \exp[-2W(T)] \quad (1.4)$$

where ρ_0 is the resistivity at $T = 0$ K, called residual, $\Delta\rho(T)$ is a term arising from the inelastic electron-phonon interaction and the exponential term $\exp[-2W(T)]$ represents the so-called Debye-Waller factor.

The temperature dependence of electrical resistivity can be described using the temperature coefficient of resistivity $\text{TCR} = \frac{1}{\rho} \left(\frac{\partial \rho}{\partial T} \right)$ whose sign is determined by the interplay between the two quantities: $\Delta\rho(T) \exp[-2W(T)]$ and $\rho_0 \exp[-2W(T)]$. We can thus identify four different regimes:

- In the case of MG in which the residual resistivity is lower than about 50-60 $\mu\text{Ohm cm}$, the term $\Delta\rho(T)$ dominates and the electrical resistivity shows a T^2 dependence below 20 K and $+T$ above 30 K. Therefore, the TCR is positive over the whole temperature range 2-300 K.
- For $60 < \rho_0 < 100 \mu\text{Ohm cm}$, the Debye-Waller starts to dominate the temperature dependence. Therefore, the electrical resistivity follows a $+T^2$ dependence at low temperature and $(1 - \beta T)$ at high temperatures giving rise to a maximum of resistivity at intermediate temperature. This maximum tends to lower temperatures with increasing ρ_0 until vanishing.
- for $100 < \rho_0 < 150 \mu\text{Ohm cm}$, the Debye-Waller factor dominates electronic transport in the whole temperature range, The electrical resistivity follows then its temperature dependence, which is $(1 - \alpha T^2)$ at low temperatures and $(1 - \beta T)$ at high temperatures. The crossover between the two regimes is at several tens of degrees. This case is characterized by a negative TCR over the whole temperature range.
- Going from low resistivity (50 $\mu\text{Ohm cm}$) to $\approx 200 \mu\text{Ohm cm}$ the electron mean free path decreases, until it is equal to the average interatomic distance for glasses with $\rho > 200 \mu\text{Ohm cm}$. Here electrons are mostly localized and the TCR is negative in the whole temperature range.

1.1.2.2 Chalcogenide glasses

In chalcogenide glasses, localized trap states play an important role in the electronic transport properties. We focus in the following paragraphs on describing their physical origin and their influence on the electronic transport.

Trap states

In perfect crystals, the electronic transport is insured by extended states which have non-localized wave functions. Carriers occupying extended states are called free carriers. In contrast to crystals, electronic states which are subject to an aperiodic potential can turn into space-localized states due to high disorder in the atomic structure [34, 35]. These localized states are denoted as trap states and show an exponential decaying wave function due to the destructive interference introduced by the disorder.

The notion of trap states exists already in crystals but becomes fundamental in amorphous materials where the disorder is ubiquitous and dominates all properties.

Depending on their physical origin, trap states can be classified into defect band and band tail states. Defect band states (Fig. 1.2 (a)) can be caused by over or under coordinated atoms and thus can be

present in crystals as well. In this case, localized energetic states are created and in case of a high defect concentration their overlap can result in a band of defect-induced states.

In glasses, the lack of long range order induces additional localized states located in the band tails. The existence of a large distribution of bond lengths and angles results indeed in spatial fluctuations of the band edges. As a consequence, there exist regions within the band, where charge carriers can be trapped. As shown in Fig. 1.2 (b) the usually sharp band edges are replaced by a broad tail extending into the forbidden gap. States within the band tail are thus separated in localized and extended states by the so-called mobility edge, E_c and E_v for conduction and valence band respectively.

At zero temperature only charge carriers above E_c (or below E_v) are mobile and contribute to transport, similarly to a crystal but with shorter mean free path. Charge carriers within the localized band tails (e.g. within the mobility gap) will be able to move only by thermally activated hopping. The valence band tail will have a donor character against an acceptor character for the conduction band tail.

In disordered systems the mobility band gap is in general not equal to the optical band gap in contrast to crystalline systems.

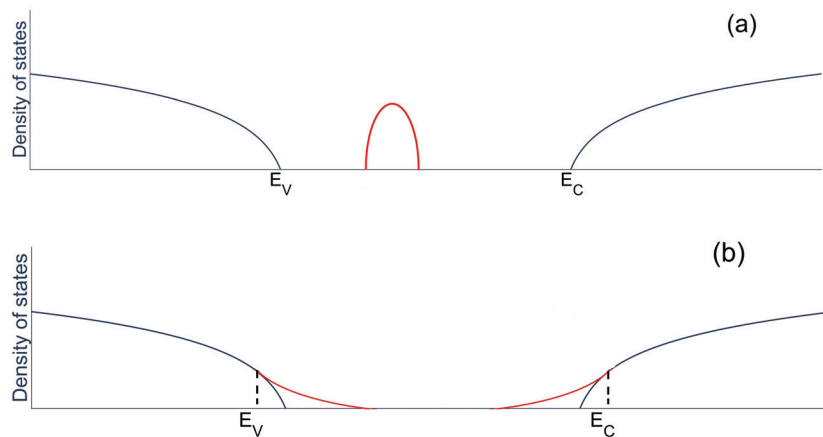


Figure 1.2: (a): Schematic representation of defect bands which can be caused by imperfections in the structure. (b): Schematic representation of band tail states which exhibit an exponentially decaying behavior reaching from the mobility edges E_v and E_c into the gap. The trap states are shown in red in both figures.

Defect states

There exist several band models for describing defect states in chalcogenide glasses. We report here the Cohen-Fritzsche-Ovshinsky (CFO) [36] and the Valence-Alternation-Pair model (VAP) [37] which are the most largely renowned. Both of them demonstrate that the Fermi level E_F is pinned at mid gap. A sketch of the electronic band structure as assumed by the two models is reported in Fig. 1.3.

The CFO-model is based on the assumption that the tails of the valence and conduction bands overlap, e.g. an electron with a given energy in such overlapping range can be in a valence band in some point of the material and still have a higher energy than an electron in a conduction band in another point of the material.

It can be thought that empty states in the valence band tail give raise to a randomly distributed positive charge, while electronic-occupied states in the conduction band tail to a corresponding negative charge.

The requirement of charge neutrality pins then the Fermi energy level at the center of the gap, where the density of states is minimum.

In contrast to the CFO model, the VAP model proposes the presence of defects resulting from over or under-coordination, respectively. Chalcogen atoms present lone pair electrons, that, in an amorphous structure, are randomly oriented, resulting in wide range of lone-pairs interactions. As a consequence of their electronic structure, dangling bonds are energy-expensive defects, and tend to be absent, while the conversion of a lone-pair into a bonding/anti-bonding pair costs very little energy, giving to the glassy structure a high degree of flexibility.

Divalent chalcogenides would ideally stay in the bonding state C_2^0 , where C stands for the chalcogenide atom, the subscript gives the covalent coordination and the superscript the charge state. The lowest energy defect is thus not a dangling bond, which would be C_1^0 , but a three-fold coordinated atom, C_3^0 which costs lower energy. Still it is found that this latter is not stable, and actually the lowest-energy defect consists in a pair of neighboring differently coordinates states (VAP), a three-fold over-coordinated, positively charged defect C_3^+ and a negatively charged, one fold undercoordinated defect C_1^- .

The donor-like defects C_3^+ create a defect band energetically located above the Fermi energy E_F . The defect C_1^- creates a band of acceptor states located below the Fermi energy E_F . Valence-Alternation Pairs are estimated to give rise to a large defect concentration in the range of 10^{17} to 10^{20} cm^{-3} in chalcogenide glasses. The creation of a VAP costs a total energy which is given by the balance between the coulomb repulsion between two electrons on the same site, the coulomb attraction between the two sites with opposite charge, and a lattice relaxation energy due to the atomic rearrangements induced by the VAP creation. The energy balance gives the correlation energy of the defect U . When U is negative, the Fermi level is pinned within the gap, e.g. it does not change with defect states occupancy.

In contrast, if defects are characterized by a positive U , the Fermi level strongly depends on the trap occupancy and thus is expected to shift significantly with temperature or doping concentration.

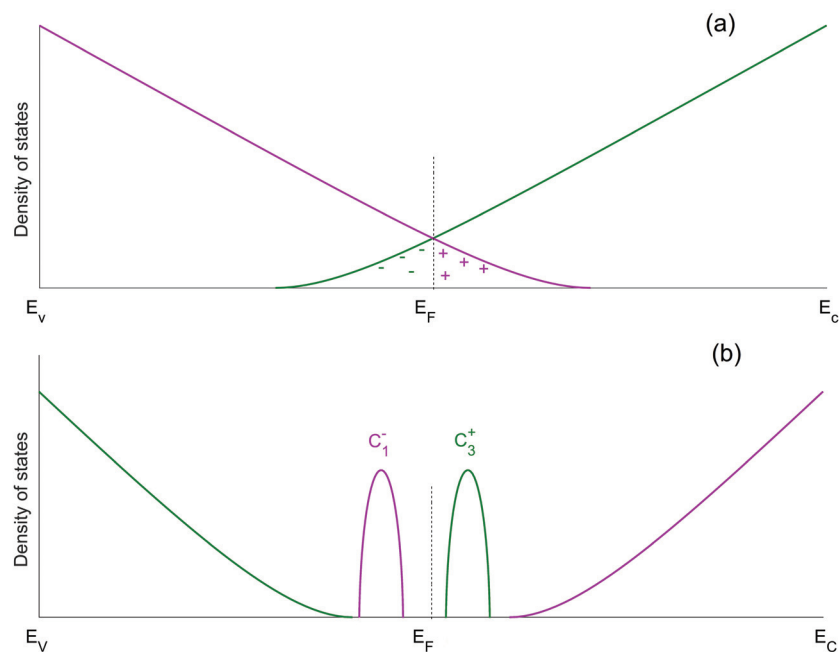


Figure 1.3: (a): Schema of the CFO model: overlapping valence and conduction band tails give rise to compensated local space charges. (b): Schema of the VAP model: structural defects result in charged defects known as C_3^+ and C_1^- .

Hopping transport models

Chalcogenide glasses are quite typical amorphous semiconductors, e.g. they show a mostly Arrhenius-like activated conductivity with an activation energy E_a which is equal to half the mobility gap, e.g. the position of the pinned Fermi energy. The Arrhenius conductivity is thus given as a function of temperature T by:

$$\sigma(T) = \sigma_0 \exp\left(-\frac{E_a}{k_B T}\right) \quad (1.5)$$

Where k_B is the Boltzmann constant and σ_0 is in the 150-600 $\Omega \text{ cm}^{-1}$ range. This thermally activated conduction mechanism is dominant at room temperature and is called "band-conduction", as it involves band states.

Another possible conduction mechanism is hopping between localized states within the gap. Hopping conduction can be described using the Mott formalism.

If we consider two localized states spatially separated by a distance R_{ij} , the probability for hopping from a localized state i to an empty localized state j will be: $P_{ij} = \exp(-2\alpha R_{ij} - \frac{E_j - E_i}{K_B T})$ for $E_j > E_i$, otherwise $P_{ij} = \exp(-2\alpha R_{ij})$ for $E_j < E_i$. Here α is a localization parameter, E_i and E_j are the energies of the localized states i and j . It can thus be seen that the hopping probability depends on the spatial and energetic distance between the two states, that is, it will change in a 4-dimensional hopping space, given by the real space and the energy. When localized states are randomly distributed in space and energy, the highest hopping probability will be for hopping to nearest neighboring sites in the 4-dimensional hopping space.

Hopping to nearest neighbors in the 3-dimensional physical space will take place when the first term dominates in the exponential, e.g. when $\alpha R_0 \gg 1$, with R_0 the average spatial distance to the nearest neighboring empty localized state. Such condition corresponds to a strong localization and/or low concentration of localized states. The hopping distance will thus be R_0 and the conduction mechanism is called nearest neighbor hopping (NNH). The temperature dependence of the electrical conductivity will be $\sigma = \sigma_0 \exp((\frac{-T}{T_0})^{1/4})$.

In the opposite case, αR_0 comparable with unity, or in all cases at sufficiently low temperature, the second term will dominate the exponential, and hops can take place to sites that are further away in space but closer in energy. This is the variable range hopping (VRH) process, where the temperature dependence of the electrical conductivity turns out to be: $\sigma = \sigma_0 \exp(\frac{-W}{K_B T})$ with $W = E_i - E_j$.

Poole-Frenkel model

The Poole Frenkel model describes electric transport due to trapped carriers in presence of an electric field [38, 39]. In the absence of an electric field, a trapped electron at energy E_T has to overcome an activation barrier of $E_C - E_T$ to be excited to the band of conduction and the number of released carriers n_c from traps can be estimated as:

$$n_c \sim \exp\left(-\frac{E_C - E_T}{K_B T}\right) \quad (1.6)$$

Poole and Frenkel modified this equation by considering the fact that the activation barrier can be lowered in presence of an electric field E [40]. Traps can be viewed as isolated if their concentration is low so that they do not influence each other. In this case, the electrical conductivity can be described by the so-called Poole-Frenkel field [39]:

$$\sigma_{PF} \sim \exp\left(-\frac{(E_C - E_T) + \beta\sqrt{E}}{K_B T}\right) \quad (1.7)$$

Where β is a constant.

However, in amorphous chalcogenides the trap state density is expected to be very high so that the nearest neighbor traps may interact with each other. Consequently, the lowering of the potential due to an electric field can be enhanced further and the electrical conductivity increases exponentially with the electric field as predicted by the so-called Poole's law [39]:

$$\sigma_{PF} \sim \exp\left(-\frac{(E_C - E_T) + \beta' E}{K_B T}\right) \quad (1.8)$$

where β' is a constant.

1.2 Interest of composites

Face to the growing technological demands in the modern society, the need has arisen of developing novel multifunctional materials, able to simultaneously insure different functions. To solve this issue, many strategies have been addressed to enhance and improve the properties of existing conventional classes of materials. Recently, advances in the ability to characterize, produce and manipulate nanometer-scale materials have led to nanocomposites. This new route exploits the combination of properties from the parent constituents in a single material, allowing to access new optimized properties compared to traditional materials.

Nowadays nanocomposites are used in a large number of applications in many domains ranging from biomedical to energy harvesting such as medical prosthesis, thermoelectric materials, solar cells, thermal barriers etc...

We focus here on a precise kind of nanocomposite, where crystalline nanoparticles are embedded in an amorphous host matrix. Such composites have already proved to display enhanced properties, such as optical [41] or mechanical [42, 43, 44, 45, 46].

The usually huge contrast of thermal and electric properties between ordered and disordered phases suggests that such nanocomposites could be of great interest for applications where a low thermal conductivity but a good electrical conductivity are needed, such as in microelectronics, where reduced heat dissipation is sought, or thermoelectric energy conversion [47].

From a microscopic point of view, the presence of order/ disorder interfaces is expected to play a major role, scattering the charge and heat carriers and thus further lowering the conductivity. Such effect should however be length-scale dependent, due to the presence of different characteristic lengths, such as the phonon or electron mean free path and wavelength, the nanoparticle size and distance.

In this thesis, we present a fundamental study of thermal and electronic properties in crystalline/amorphous nanocomposites with the aim of shedding light onto the microscopic mechanism governing the heat and electronic conduction.

In the next paragraphs, we report some electrical and thermal properties of amorphous/crystalline nanocomposites. Finally, we briefly review some models that can be used for transport properties prediction, based both on macroscopic and microscopic approaches.

1.2.1 Thermal properties of nanocomposites

There is a general agreement that the thermal conductivity can be reduced through nanostructuring. This idea has proved its effectiveness particularly in the case of nanocomposites. The main reason be-

hind this reduction is an increased phonon scattering through the grain boundaries depending on the size of the added particle in the parent matrix. This scattering mechanism takes place when the grain size is smaller than the acoustic phonon mean free path and comparable with its wavelength.

Recently, Wang et al [48] reported that a significant decrease in the thermal conductivity can be obtained with a particle size of ≈ 10 nm.

If the size reduction has been found to significantly affect the thermal conductivity in crystalline materials, the combination of a naturally low conducting amorphous phase with a crystalline phase has also shown to be promising. This was indeed reported in nanocomposites made of Si/SiO_x core-shell nanoparticles, where the amorphous oxide shell is shown to further reduce the thermal conductivity with respect to a material made only of silicon nanoparticles [49, 50]. In one case a thermal conductivity close to the amorphous limit for silicon was observed [49].

Another remarkable thermal conductivity reduction has also been reported in the case of GeTe based nanocomposite [51] obtained by partial crystallization from the amorphous bulk phase. The presence of nanocrystals of 4-8 nm of size leads to a conductivity of 0.6 W/m K instead of 4.2 W/m K in its crystalline counterpart.

1.2.1.1 Effective thermal conductivity of composites

Maxwell was the first to propose analytical expressions for the effective conductivity of heterogeneous media in the framework of his work on electricity and magnetism. His theory describes the case of spherical particles of conductivity k_1 embedded in a uniform matrix of conductivity k_m , where thermal interactions between filler particles are ignored. The effective thermal conductivity is then given by [52]:

$$\frac{k_{eff}}{k_m} = 1 + \frac{3\phi}{\left(\frac{k_1 + 2k_m}{k_1 - k_m} - \phi\right)} \quad (1.9)$$

Where ϕ is the volume fraction of the filler. However, Equation 1.9 was found to be valid only for low volume fractions (lower than 25%). Later, models were developed to describe composites with higher volume fractions. One of the most important models, from the historical and practical point of view is the Effective Medium Theory (EMT) or Effective Medium Approximation (EMA) and belongs to the class of mean field-theories. They are highly relevant to predict the macroscopic properties of heterogeneous materials such as composites.

The effective medium theory (EMT) was first introduced by Bruggeman in 1935 [52] in order to calculate the dielectric constants and polarizabilities for heterogeneous crystalline materials. This theory assumes that a composite made of several phases can be described as an effective homogeneous medium with effective properties, depending only on the phases volume fractions and specific properties, and not on their actual spatial distribution or particle shape.

In particular, they have successfully been exploited to predict the thermal conductivity of composites. In the presence of two phases the EMT theory gives the following formula:

$$\phi_1 = \frac{\lambda_1 - \lambda_e}{\lambda_1 + 2\lambda_e} + \frac{\lambda_2 - \lambda_e}{\lambda_2 + 2\lambda_e} \quad (1.10)$$

Where ϕ_1 is the volume fraction of the phase 1 and λ_1, λ_2 are the two phases thermal conductivities. λ_e denotes the effective medium thermal conductivity.

1.2.1.2 The acoustic mismatch model

The acoustic mismatch model describes the physics of heat transfer through interfaces at low temperatures at a microscopic scale. It was historically developed first by Kapitza [53] and later by Khalatnikov [54] at a microscopic level. In the acoustic mismatch model, the interface is treated as a planar continuous interface and the phonons as plane waves.

Due to such assumptions, this model is only relevant if the phonons wavelength is much greater than the interatomic spacing and as such only for low frequency phonons (<100 GHz).

Within such approximation, when the phonon impinges onto the interface, it could be transmitted or specularly reflected. The transmission probability can be calculated depending on the incidence angle, anisotropy of the interface and phonon modes.

In the particular case of an isotropic interface between two homogeneous media numbered 1 and 2, and normal incidence, the transmission will be:

$$\alpha = \frac{4Z_2Z_1}{(Z_1 + Z_2)^2} \quad (1.11)$$

The subscripts 1 and 2 correspond to the solid 1 and the solid 2 respectively. Z denotes the acoustic impedance given by the product: $Z = \rho c$, where ρ is the mass density and c is the phonon velocity. It can be then seen that the transmission coefficient will depend on the phonon mode only through the frequency dependence of its sound velocity. The acoustic impedance mismatch is given by the ratio: Z_1/Z_2 .

1.2.1.3 The diffuse mismatch model

Eisenmenger et al [55] demonstrated that the assumptions of a continuous planar interface and specular reflectivity breaks down for high energy phonons (> 100 GHz).

Instead, all phonons are diffusely scattered at the interface because of its physical and chemical roughness. This led Swartz and Pohl to propose the diffuse mismatch model, which assumes that phonons lose their memory after reaching the interface and that the probability of transmission to either side of the interface depends on the ratio between the densities of states of the two media. The diffuse transmission is thus defined as:

$$T = \frac{D_1}{D_1 + D_2} \quad (1.12)$$

Where D_1 and D_2 denote the phonon density of states of the medium 1 and 2 respectively.

1.2.2 Electronic properties of nanocomposites

It is largely known that the electrical resistivity of glasses decreases with crystalline fraction. This has been reported in many different systems such as metallic glasses [56, 57, 58] and chalcogenides [59] where the resistivity continuously decreases during crystallization. Such behavior corresponds to a lack of any enhanced electron scattering at amorphous/crystalline interfaces.

Depending on the electrical contrast between glass and nanocrystalline grains, the resistivity decrease with crystallization can be extremely large, up to several orders of magnitude in the case of chalcogenide glasses. Indeed, composites made of electrically insulating glasses with conductive crystalline particles have been shown to exhibit a strongly reduced electrical resistivity [60, 61, 62].

However, some studies [63, 64, 65] reported the appearance of a non monotonic evolution of the electrical resistivity where this latter shows a sharp increase in the early stages of crystallization, then followed

by the usual decrease. This behavior was also observed in thermopower measurements and was understood as due to a strong scattering effect at the amorphous/crystalline interfaces when a large concentration of very small crystallites is present. The effect would then decrease with the on-going crystallization due to the crystallites growth.

Amorphous/crystalline composites have also shown an enhancement of the Seebeck coefficient. This was reported for $(\text{Bi}_2\text{Te}_3)_{0.2}(\text{Sb}_2\text{Te}_3)_{0.8}$ containing SiO_2 nanoparticles [66] and partially crystallized CrSi [63, 64]. Such enhancement was ascribed to an energy dependent strong scattering of charge carriers at the amorphous/crystalline interfaces [64].

1.2.2.1 Effective medium theory for electrical conductivity prediction

In 1952, Landauer [67] derived in an EMT approach the equation for predicting the electrical conductivity in multi-phasic metallic media. For a composite made of two phases with volume fractions ϕ_1 and ϕ_2 and electrical conductivities σ_1 and σ_2 , similarly to the case of the thermal conductivity, it is found:

$$\phi_1 = \frac{\sigma_1 - \sigma_e}{\sigma_1 + 2\sigma_e} + \frac{\sigma_2 - \sigma_e}{\sigma_2 + 2\sigma_e} \quad (1.13)$$

σ_e denotes the effective medium electrical conductivity.

Chapter 2

Experimental and theoretical methods

2.1 Experimental Methods

Two systems have been investigated in this thesis: a composite made starting from a metallic glass (MG), $Zr_{52.5}Cu_{27}Al_{10}Ni_8Ti_{2.5}$, and one made from a chalcogenide glass, carbon doped GeTe (C-GeTe). In the first section we present the methods used for preparing the amorphous/crystalline nanocomposites, from the glass synthesis to the crystallization thermal treatments. The techniques used for monitoring the crystallization, and investigating crystalline fraction and grain size distribution are described in the second section. Finally in the last section, we describe the electrical transport and phonon dynamics measurement techniques used in this thesis.

2.1.1 Sample Preparation

2.1.1.1 Glass Synthesis

The preparation of an amorphous system requires to cool down the liquid fast enough to be able to overcome crystallization and freeze the system in a disordered structure. Depending on the system, the critical cooling rate for vitrification can change by orders of magnitude. A system which vitrifies easily, with quenching rates lower than 100 K/s, is defined as good glass former. This is usually the case of multi-component alloys, such as the bulk metallic glass investigated here. $Zr_{52.5}Cu_{27}Al_{10}Ni_8Ti_{2.5}$ is well known for having a very good glass forming ability, so that a quite low cooling rate is needed for glassyfyng the melted alloy and bulk samples can be obtained.

Indeed, we could synthesize rods 8 mm long and 3 mm wide, by arc-melting the pure elements in stoichiometric concentration under argon atmosphere and quenching the master alloy in a water-cooled copper mold. Discs up to 2 mm thick were cut from the as-prepared rods for further characterization and nanocomposite preparation.

The second system studied in this thesis was prepared by our collaborators at the CEA LETI (Grenoble). 100 nm thick films of pure GeTe and Carbon doped GeTe were prepared by cosputtering of the pure elements on a silicon substrate, topped with 500 nm thick thermal oxide. After deposition, the thin films were capped with a 10 nm thick layer of SiO_2 in order to prevent any oxidation. Three doping were prepared, with an atomic carbon content of 4, 9 and 16% at.



Figure 2.1: a) Half of the copper mold on the left and crucible on the right used for casting 3mm diameter cylinders of bulk metallic glasses. b) The as casted metallic glass rod.

2.1.1.2 Thermal Protocols

A glass is by definition an out-of-equilibrium system. When fast cooled, from the liquid the system falls out of equilibrium, meaning that it is trapped in a local minimum of the potential energy, from which it will slowly evolve with time towards the equilibrium state. When the atoms are provided extra energy, for example by means of annealings, they will be able to rearrange in a more equilibrium configuration, ultimately leading to crystallization. This can be achieved by two different annealing protocols: either a linear annealing, with constant heating rate, either an isothermal annealing.

When the crystallization process is abruptly interrupted by a fast quench, before total crystallization can be completed, an amorphous/crystalline composite will be obtained, meaning an amorphous matrix with embedded crystalline inclusions.

In a multicomponent system, crystallization mainly takes place through the precipitation of crystalline grains with a different stoichiometry. As a consequence, the grains remain nanometric in size, as, for growing, an important atomic diffusion is needed, the surrounding being depleted of the corresponding atoms. During an annealing, a competition exists then between the crystals' nucleation and their growth, ruled by the heating rate and annealing time. It is thus possible, with a controlled thermal protocol, to prepare composites with a finely controlled grain size and crystallization fraction.

In this work we prepared MG composites by means of an isothermal annealing, and C-GeTe composites by means of a linear annealing. Different experimental techniques were used to monitor crystallization and tune the annealing time depending on the aimed crystalline fraction.

Metallic glasses composites preparation

The amorphous/crystalline composites were prepared by isothermally annealing the glass at a temperature lying between the glass transition and the crystallization temperature, monitoring the crystallization by the differential scanning calorimetry (DSC) which is a technique used to study the thermal properties of materials.

It measures the heat flux between the sample and the environment, thus giving a measurement of the exchanged enthalpy. It allows thus to track phase transitions which appear as peaks in the enthalpy change as a function of temperature. Specifically, the DSC measures the heat flux as compared with the one of a reference sample, for which we used an empty sample holder. When heating a glass, the DSC allows thus to observe the glass transition temperature and the crystallization, the former giving rise to a change in the slope of the enthalpy change, and the latter manifesting as an exothermal peak. For our DSC measurements, we used the Diamond apparatus from Perkin Elmer.

Discs 300 μm to 2 mm thick were cut from the the MG rod, then polished and cleaned with ethanol. The obtained masses were between 40 and 90 mg. In order to hinder the crystalline growth and get nanometric crystalline grains, the highest available heating ramp was used, 100 K/min, for which a glass transition (T_g) and crystallization (T_x) temperature of 724 K and 800 K have been respectively measured as it can be seen in Fig. 2.2. On the basis of this information, we have chosen as target temperature for the partial crystallization protocol $T_a=740$ K and performed an isothermal DSC experiment to first characterize the whole crystallization process.

In the case of a single crystallization process (e.g. precipitation of a single crystalline phase), the area underlying the crystallization peak in a DSC scan can be considered as linear with the crystalline fraction, so that, during an isothermal annealing, at each time t the crystalline fraction can be calculated as

$$x(t) = \frac{\int_{t_1}^t H(t') dt'}{\int_{t_1}^{t_2} H(t') dt'} \quad (2.1)$$

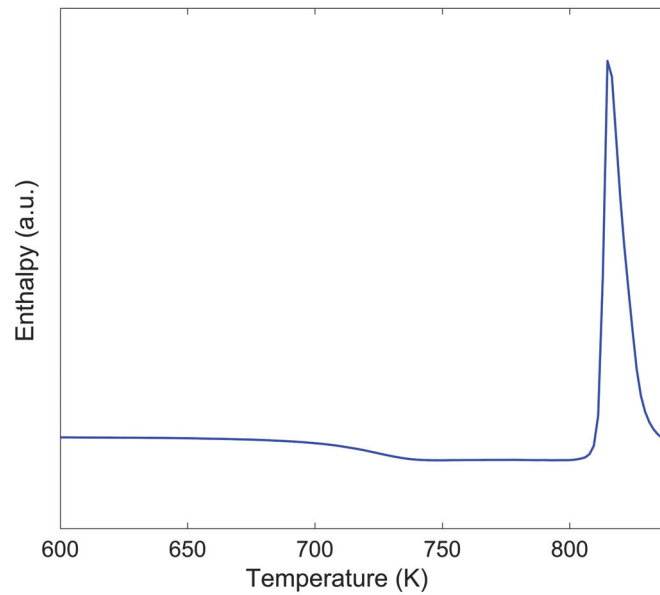


Figure 2.2: Enthalpy change measured by DSC during the annealing of the MG sample with a ramp rate of 10 K/min. The glass transition temperature T_g and the crystallization temperature T_x are defined respectively by the change of the slope around $T=724$ K and the beginning of the exothermal peak around $T=800$ K

where t_1 and t_2 mark the time at which the crystallization peak starts and ends. Similarly, for an annealing with a constant rate (linear annealing), $x(t)$ will be

$$x(T(t)) = \frac{\int_{T_1}^{T(t)} H(t') dt'}{\int_{T_1}^{T_2} H(t') dt'} \quad (2.2)$$

where, again, T_1 and T_2 correspond to the starting and ending temperatures of the crystallization peak. As a first approximation, such formulas can be used also when a primary crystalline phase dominates the crystallization process, despite the presence of secondary phases.

Using Eq. 2.1 we have thus been able to extract the annealing time dependence of the crystalline fraction from the calorimetric signal (see Fig. 2.3), as done in Ref. [68], and use it as a guide for preparing amorphous/nanocrystalline composites with different crystalline fractions, by changing the annealing time at $T=T_a$, while following the calorimetric signal.

Chalcogenide glasses composites preparation

The crystallization of chalcogenide samples was monitored using two methods.

The first one consists in measuring the reflectivity during the sample annealing. Indeed, the amorphous phase is characterized by a lower reflectivity than the crystalline phase, so when the phase transformation occurs, the measured reflectivity value increases, allowing to track crystallization (see Fig. 2.4 (a)). Samples were placed in a vacuum chamber and their reflectivity measured with a red laser beam ($\lambda=670$ nm). A linear annealing was then performed with a heating rate of 20 K/m. The fraction of crystallization was determined by normalizing the measured reflectivity to the difference of the reflectivity between the start and the end of crystallization.

The second method was used to monitor full crystallization without getting any quantitative measure-

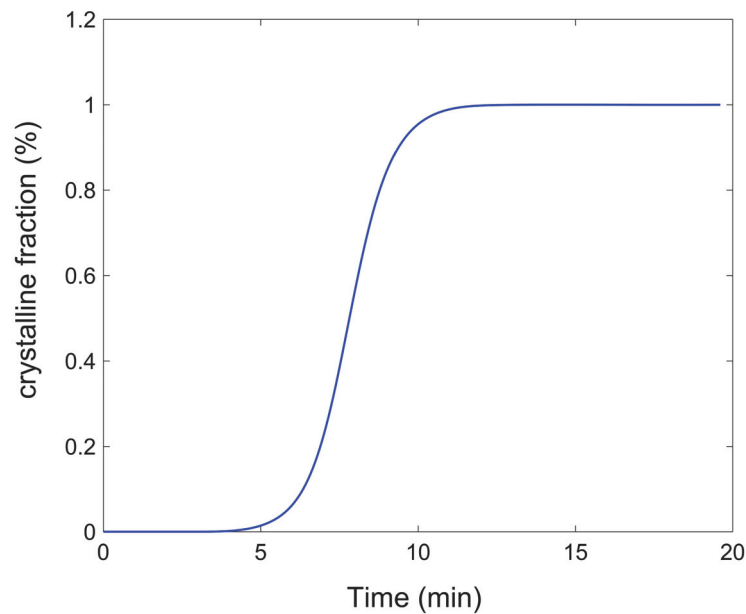


Figure 2.3: A typical crystallization fraction curve as a function of time obtained from the integration of the crystallization peak, at $T=740$ K.

ment of the crystalline fraction. It consists in measuring the electrical resistivity by means of a four points probe during a linear annealing, with a heating rate of 20 K/m. It can be seen in Fig. 2.4 (b) that the electrical resistivity spans many orders of magnitude during crystallization. The advantage of this method is that not only we check that we are in the fully crystallized sample, but at the same time we get its electrical characterization at high temperature during cooling down.

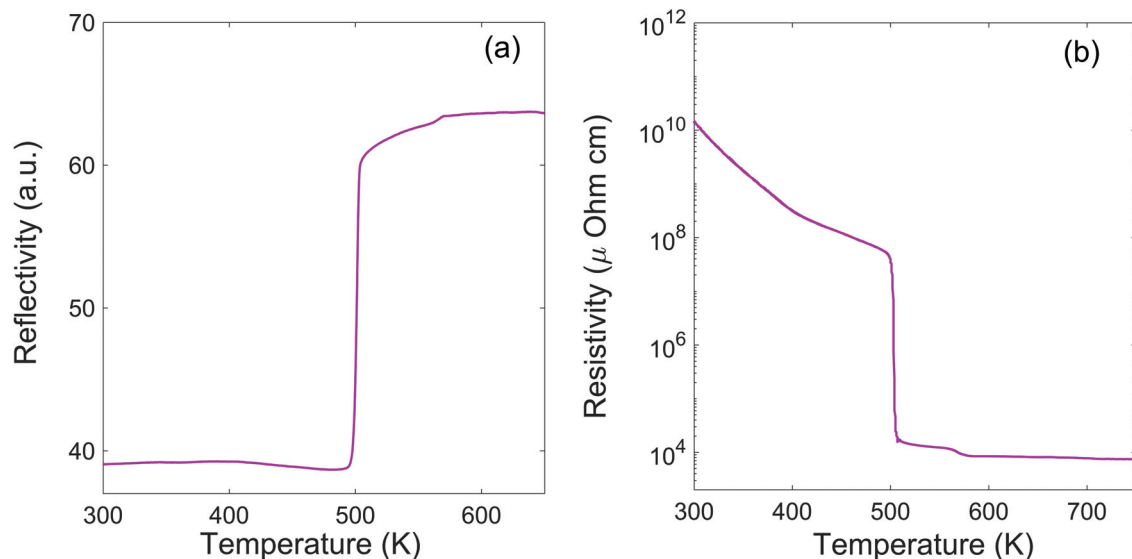


Figure 2.4: Crystallization of a pure GeTe sample monitored by reflectivity (a) and electrical resistivity measurements (b).

2.1.2 Physical Characterization

In this section we describe the experimental techniques used for characterizing the nanocomposites structure.

2.1.2.1 Transmission Electron Microscopy (TEM)

The most powerful tool for characterizing the crystalline fraction and grain size distribution is the Transmission Electron Microscopy (TEM), which however, requires a lengthy and careful preparation of the sample. Here we only describe the TEM measurements that we performed on MG samples, as TEM in C-GeTe samples was done by our collaborators at the CEA. Prior to TEM measurements, MG samples were subject to a two steps polishing. First, discs 100-300 μ m have been mechanically polished down to a thickness of less than 60 μ m. Second, they have been ion-polished using PIP Gatan 691 model in top-bottom mode at 2.5 kV with a milling angle of $\pm 4^\circ$.

These instrumental parameters have been chosen in order to hinder any possible ion beam induced crystallization, after having tested the resistance of the amorphous phase against crystallization with several different angles and tensions [69, 70, 71]. TEM was performed using a JEOL 100 JEM2100 equipped with a LaB6 thermionic electron gun and a High Tilt objective pole piece. The microscope was operated at 200 keV with a point-to-point resolution of 0.25 nm. The samples were mounted on a double-tilt beryllium sample holder and the images were recorded on a Gatan Orius SC1000 bottom mount CCD camera with 4008×2672 pixels with a physical size of 9 μ m each.

2.1.2.2 X-Ray Diffraction (XRD)

In order to characterize the amorphous/crystalline nature of the samples and get structural information, we have performed X ray diffraction at the X-ray diffraction center Henry Loncharbon in Lyon, using a D8 advanced diffractometer in Bragg-Brentano Geometry with $\lambda=1.541 \text{ \AA}$. In Fig. 2.5 we report the typical spectrum as measured on an as-cast MG sample, showing no Bragg peaks, but only a broad peak, indicating the non-crystalline nature of the material. The XRD pattern of a partially or fully crystallized sample is made of Bragg peaks, which allow for the identification of the crystalline phases, and the estimation of crystalline fraction and grain size distribution, as will be explained in chapter 3 with the experimental results.

2.1.3 Transport Measurements

2.1.3.1 Van Der Pauw (vdp)

One of the effective techniques to measure the electrical resistivity of a thin sample is the Van Der Pauw method (vdp), whose advantage is that it allows to eliminate the influence of the contacts resistance and of the geometry of the sample by using a four points probe. This technique requires that the sample is thin with respect to its lateral dimension, homogeneous in thickness and without holes. If these conditions hold, then its surface is simply connected using peripheral contacts sufficiently small, ideally point-like or with a negligible size with respect to the sample size.

By using two different measurement configurations, as described in Fig. 2.6, two resistance values R_A and R_B can be obtained, from which the sheet resistance is calculated as:

$$\rho = \frac{\pi \cdot d}{\ln(2)} \cdot \frac{R_A + R_B}{2} \cdot f \quad (2.3)$$

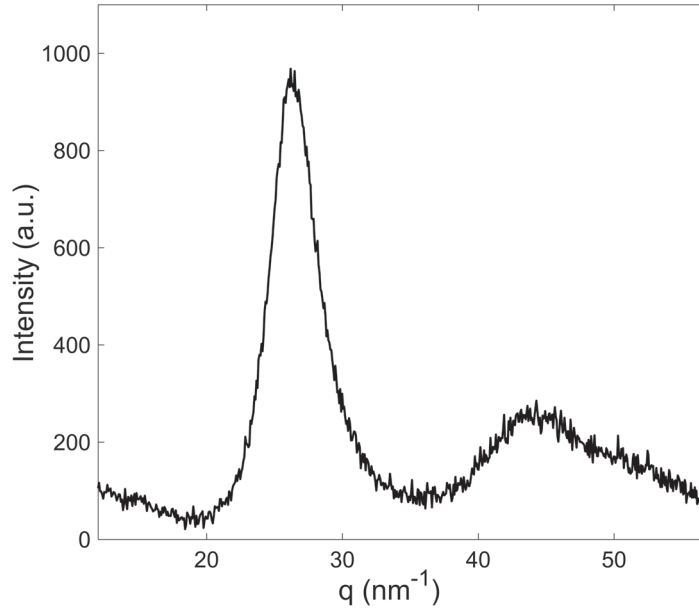


Figure 2.5: Diffraction pattern collected on an as-cast MG sample with $\lambda=1.541 \text{ \AA}$ after background subtraction. No sharp peak can be observed confirming that the sample is fully amorphous

where f is the correction function which depends on the ratio $x = \frac{R_A}{R_B}$ and can be calculated as follows:

$$\frac{x-1}{x+1} = \frac{f}{\ln(2)} \cdot \arccos\left(\frac{\exp(\ln(2)/f)}{2}\right) \quad (2.4)$$

Its dependence on the $\frac{R_A}{R_B}$ ratio is reported in Fig. 2.7. The vdp measurement setup was mounted on the cold-finger of a displax cryostat, able to get down to 10 K. MG samples have been contacted using electrically conductive silver paste, which is designed specifically for such measurements and works down to cryogenic temperatures. In the case of C-GeTe samples, the procedure was more sophisticated. First, the SiO_2 capping was removed using a HF bath and the surface was plasma-cleaned, then 300 nm thick Chromium coatings were deposited by thermal evaporation on four points of the surface, properly masked. Finally these contacts were connected to the tension and current wires of the measuring apparatus via Aluminium wire bonding.

2.1.3.2 Seebeck coefficient

In a thermoelectric material, the application of a temperature gradient at the sample borders results in a voltage between them. The Seebeck coefficient is then defined as the ratio between the arisen voltage ΔV and the applied temperature gradient ΔT :

$$S = \frac{-\Delta V}{\Delta T} \quad (2.5)$$

To measure S we need to measure two quantities exactly at the same points on the sample, namely the temperature T and the electrical voltage V . In our setup, the sample is glued on a copper holder, with an edge in contact with an isolated heater. Two thermocouples of type "T", made of Cooper and Constantin,

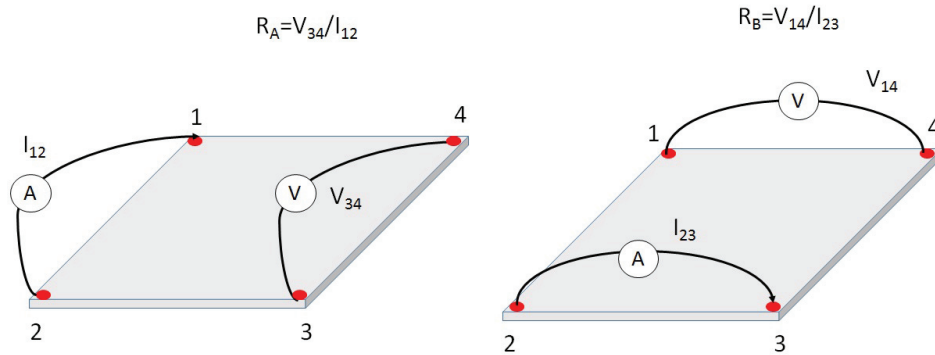


Figure 2.6: The two measurement configurations used in the Van Der Pauw method for measuring the sheet resistance of a thin sample.

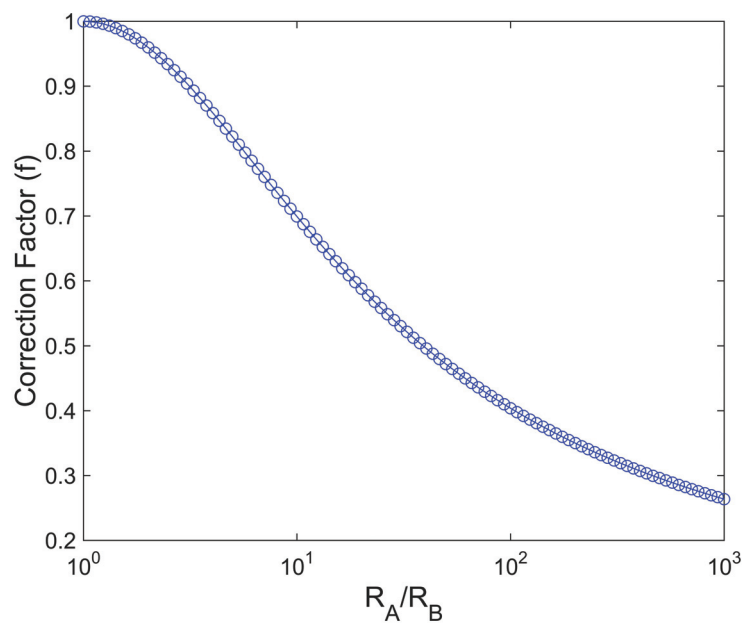


Figure 2.7: Van der Pauw Correction factor as a function of the ratio between the resistances R_A and R_B measured in the two configurations in a vdp measurement.

are soldered on two metallized spots located as close and as far as possible from the heater. However, this can result in the formation of further interfaces on the surface of the sample inducing thus additional electrical and thermal resistances which may hinder the precision of the measurement. For this reason, it is important to use very thin layers for metallization: in our case we have glued on the sample surface two thin gold layers using a thin and uniform silver paste. The contact sheet was about 200μ in lateral size. Our Seebeck measurements were conducted using a home-build set-up mounted on a liquid nitrogen flux cryostat and operating between 70 and 300 K and employing the differential method [72] in which a variable temperature gradient is applied, growing linearly with time.

The typical electric scheme is illustrated in Fig. 2.8, The measured voltage ΔV , given by the difference $U_{DC} - U_{AB}$ and the temperature gradient $T_C - T_H$ allow to measure the Seebeck coefficient S of the sample by fitting linearly the quantity $-\frac{\Delta V}{\Delta T}$, as it is reported in Fig. 2.9 where an example of measurement performed on a Nickel sample is shown. It is important to say that in order to reliably extract the sample Seebeck coefficient, it is necessary to take into account the contributions to the measurement from the Seebeck coefficients of the thermocouple wires, as well as from the voltage offsets at the con-

tacts A,B,C,D. These factors affect the temperature reading done with the thermocouples, and thus the ΔT , as well as the total measured voltage, and thus ΔV . In order to get rid of the errors associated, we have taken into account all these factors in the ΔT calculation. At this point the slope of $-\frac{\Delta V}{\Delta T}$ is only related to the Seebeck coefficient of the sample.

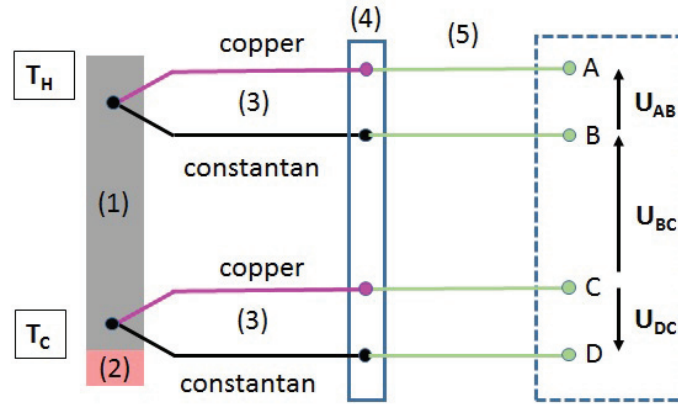


Figure 2.8: Schematic representation of a Seebeck coefficient measurement. The sample (1) is subject to a temperature gradient $T_C - T_H$ generated by a heater (2) glued on one side of it. The measurement is insured by a pair of thermocouples (3) made of copper and constantan and both of them are fixed to an isothermal junction, in order to reduce experimental errors related to the Seebeck coefficient of the wires (4). The thermocouples are finally connected to copper wires and the voltage measured at points A,B,C and D (5).

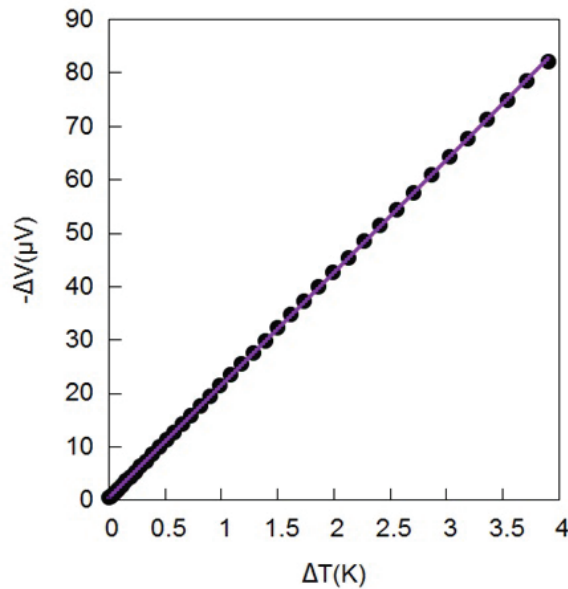


Figure 2.9: Example of Seebeck coefficient S measurement on a Nickel sample. The Seebeck coefficient is obtained by the linear fitting of $-\frac{\Delta V}{\Delta T}$. Here $S = -18 \mu V/K$

2.1.3.3 Scanning Thermal Microscopy (SThM)

Thermal conductivity of MG samples has been measured using Scanning Thermal Microscopy (SThM) technique which is mainly based on an Atomic Force Microscopy (AFM) set-up with a miniaturized sensitive thermal probe [73, 74]. The thermal probe that we have used is a bended Pt 90%/Rh 10%

wire coated by a silver shell [75], called Wollaston point (see Fig. 2.10). The tip is mounted on a force sensitive cantilever and the feedback loop is used in order to maintain a constant tip-surface force while scanning across the sample surface. The tip is heated to a higher temperature than the sample and put in contact with it. The heat transfer between the tip and the surface changes the sensor temperature leading to change in the tip resistance. The tip's temperature change is thus measured and used as an input in models of the heat flux from the tip to the sample, which allows to estimate the sample thermal conductivity. Prior to the measurements, a calibration of the probe has been performed on standard samples spanning a thermal conductivity range from $1.5 \text{ W K}^{-1}\text{m}^{-1}$ (SiO_2) to $58.6 \text{ W K}^{-1}\text{m}^{-1}$ (Ge). A critical point of this setup is the quality of the tip-sample contact, and thus the surface roughness. For this, we polished our samples with $0.5 \mu\text{m}$ diamond powder, which was our best possibility but still left a residual roughness larger than needed resulting in a larger measurement uncertainty.

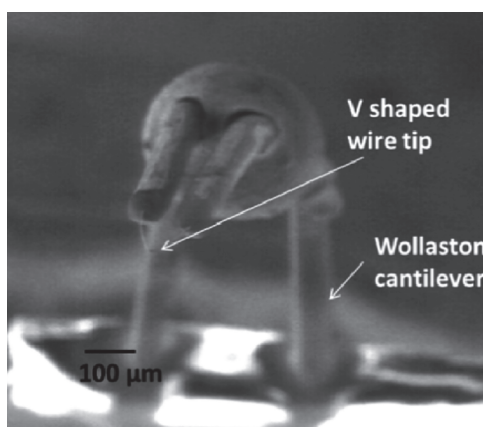


Figure 2.10: Scanning electron microscopy image of a Wollaston wire probe[75].

2.1.3.4 Inelastic X-rays Scattering (IXS)

IXS is an inelastic technique which allows to probe the excitations of matter, from atomic to electronic, depending on the probed range of energy transfer. This is illustrated in Fig. 2.11: at high energy transfers, electronic excitations are probed, while in the meV range atomic vibrations can be investigated. Here we focus onto this latter range, for accessing which we need a meV resolution. We briefly report the theory of IXS and present a description of the experimental set-up with reference to Beamline ID28 at the European Synchrotron Radiation Facility (ESRF).

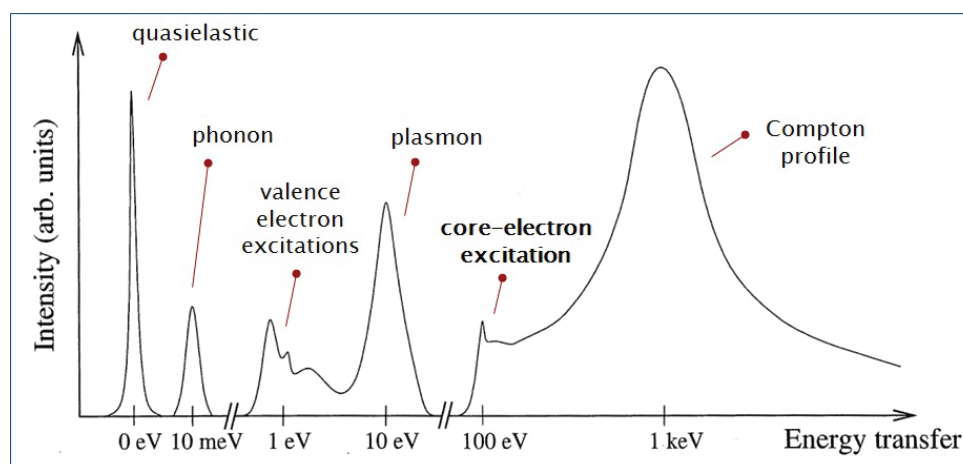


Figure 2.11: Conceptual schematic of excitations that may be probed using IXS.

Theory of the IXS experiment

In Fig. 2.11 we report a sketch of a typical inelastic scattering experiment. When an incident photon, characterized by an energy $\hbar\omega_i$, a wave-vector \vec{k}_i and polarization $\hat{\varepsilon}_i$, impinges on a sample, it is scattered by it and collected at an angle 2θ within a solid angle $d\Omega$.

The scattered photon energy, wave-vector and polarization are denoted by: $\hbar\omega_f$, \vec{k}_f and $\hat{\varepsilon}_f$, respectively. The incoming beam can interact with the sample, by exchanging an energy $\hbar\omega$ and a momentum \vec{q} with it, and exciting thus phonons or electrons. Such exchange is ruled by the conservation laws, such that: $\hbar\omega = \hbar(\omega_f - \omega_i)$ and $\hbar q = \hbar(k_f - k_i)$. In the case of elastic scattering, where there is no energy transfer between the incoming photons and the sample, the exchanged momentum is entirely governed by the scattering angle 2θ , and it is given by:

$$q = 2k_i \sin(2\theta/2) \quad (2.6)$$

This is the case, for instance, of x-ray diffraction. When an inelastic scattering process takes place, the exchanged energy is given by the difference in energy between outgoing and incoming beam. As for the exchanged momentum \vec{q} , it is given by the $\vec{k}_f - \vec{k}_i$ difference. However, at the X-ray energies used, it is $\|\vec{k}_f\| \simeq \|\vec{k}_i\|$, so that \vec{q} remains completely determined by \vec{k}_i and θ , as in Eq. 2.6.

The scattered intensity is proportional to the differential cross section $\frac{d^2\sigma}{d\Omega d\omega_f}$, defined as the ratio between the scattered and the initial flux of photons and which is related to the dynamical structure factor through the relation Eq. 2.7.

$$\frac{d^2\sigma}{d\Omega d\omega_f} = \frac{k_f}{k_i} r_0^2 |\hat{\varepsilon}_f \cdot \hat{\varepsilon}_i|^2 S(q, \omega) \quad (2.7)$$

Where $r_0 = e^2/mc^2$ is the classical electron radius and $S(q, \omega)$ is the dynamical structure factor.

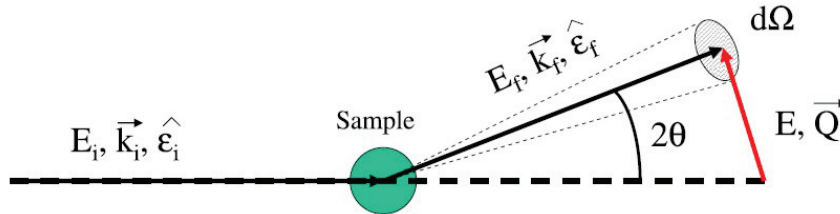


Figure 2.12: Kinematics of a scattering experiment.

Description of the Beamline ID28 at the ESRF

In this section the IXS beamline ID28 at the European Synchrotron Radiation Facility (ESRF) in Grenoble will be briefly described. The experimental strategy used for IXS measurements with meV energy resolution (thus suitable to study the high frequency collective excitations) resembles that of a triple axis neutron spectrometer (see Fig. 2.13). The first axis is the backscattering monochromator crystal which selects the energy $\hbar\omega_i$ of the incident photons. The second axis is located at the sample position, and determines the momentum transfer by selecting the scattering angle. Finally the third axis corresponds to the analyser crystal, which selects the scattered photon energy, $\hbar\omega_f$ and focuses the scattered radiation on the detector. The ID28 beamline is equipped with 9 analyzers crystals which allow for the collection of 9 different IXS spectra, corresponding to 9 different exchange momenta, at the same time.

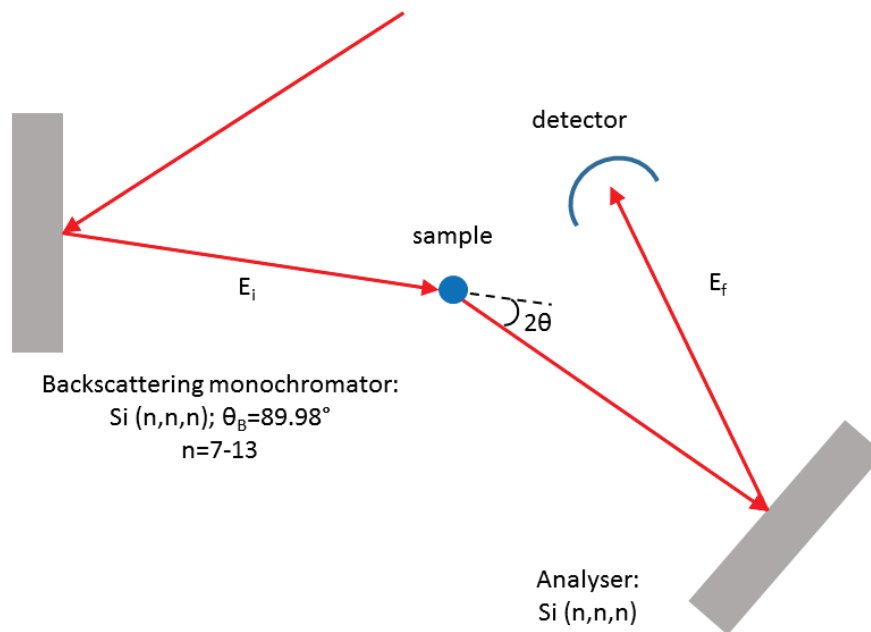


Figure 2.13: Principle of an inelastic X-ray spectrometer

The optical layout of the triple axis inelastic x-ray spectrometer is reported in Fig. 2.14. The X-ray source consists of three undulators with a magnetic period in the 26 mm 35 mm range and a total length of 4.8 m, placed in a straight section of the electron storage ring. Undulators alternate polarity, imposing a sinusoidal motion to the electrons, which then emit monochromatized X rays at the highest and lowest points of the sinusoidal trajectory. At this stage, the beam has a spectral bandwidth $\Delta E/E \sim 10^{-2}$.

The X-ray beam from the undulators is pre-monochromatized to a bandwidth $\Delta E/E \approx 10^{-4}$ using a silicon [111] double crystal monochromator kept in vacuum and cooled by liquid nitrogen. The main role of the pre-monochromator is to reduce the heat load impinging on the main monochromator. This is mandatory in order to keep the thermal deformation of the silicon crystal below the limits for which the energy resolution starts to deteriorate.

The X-ray photons from the pre-monochromator impinge onto the high energy resolution backscattering monochromator, consisting of an asymmetrically cut silicon crystal oriented along the [111] direction, operating at a Bragg angle of 89.98° .

This extreme backscattering geometry insures the minimization of geometrical contributions to the total energy resolution. The spectral angular acceptance, the so-called Darwin width, is larger than the X-ray beam divergence, and, therefore, all the photons within the desired energy bandwidth are transmitted.

Moreover, the energy resolution depends at this stage only on the monochromator crystalline quality. High order Bragg reflections and perfect crystals are required in order to obtain the necessary energy resolution of $\Delta E/E \sim 10^{-7} \div 10^{-8}$. For this reason, the silicon monochromator is used at [n n n] reflections, with $n = 7, 8, 9, 11, 12, 13$.

The backscattered beam goes then through different optical elements in order to be focused on the sample.

Two focusing schemes are routinely used at ID28, giving a focus of $250 \times 100 \mu\text{m}^2$ (H \times V) FWHM obtained with a toroidal mirror, and a focus of $30 \times 100 \mu\text{m}^2$ (H \times V) FWHM obtained with a multilayer mirror.

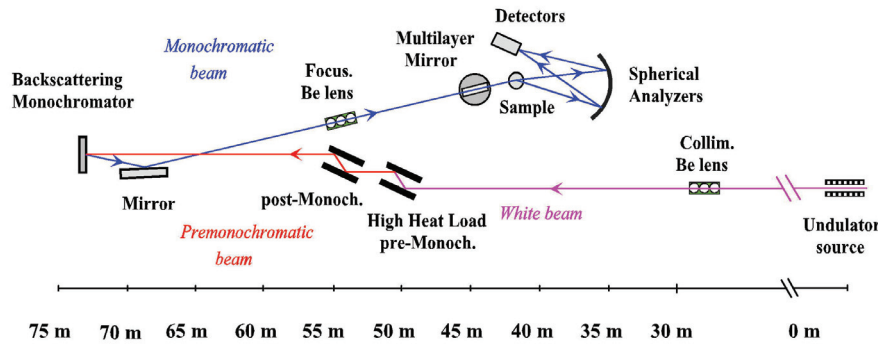


Figure 2.14: Optical layout of the beamline ID28 at the ESRF taken from Ref. [76].

The photons scattered by the sample are then energy-analyzed by the nine spherical analyzers which are mounted in a horizontal spectrometer at 7 m from the sample. The detectors (Peltier-cooled silicon diodes) are mounted close to the sample, slightly vertically shifted from the horizontal scattering plane. Sample, analyzers and detectors lie on a circle, the so-called Rowland circle. Analyzers are spherical to accept the isotropically scattered intensity, and fully remain on the Rowland circle. They operate similarly to the backscattering monochromator (e.g. in a near backscattering configuration and at the same reflection order as the backscattering monochromator). Although the problems connected to the energy resolution are conceptually the same for the monochromator and for the analyzers, the required angular acceptance is very different. The monochromator can be realized using a flat perfect crystal. For the analyzer crystals the optimal angular acceptance is dictated by the desired momentum resolution. Considering values of δq in the range of $0.1 \div 0.5 \text{ nm}^{-1}$, the corresponding angular acceptance of the analyzers crystals must be $\sim 10 \text{ mrad}$ or higher, a value much larger than the Darwin width. In addition the analyzers system has to preserve the single crystal perfection necessary to obtain the desired energy resolution. This constrain automatically excludes the possibility to consider elastically bent crystals. The solution adopted at beamline ID28 consists of laying a large number of undistorted perfect flat crystals on a spherical surface such that the desired energy resolution is not degraded. These analyzers consist of ~ 12000 silicon perfect single crystals of surface size $0.6 \times 0.6 \text{ mm}^2$ and a thickness of 3 mm, glued on a spherical substrate of a radius equal to the length of the spectrometer arm.

The analyzers are positioned in two rows with a fixed angular offset from each other of $\sim 0.75^\circ$, mounted on a 7 m long arm that can rotate around the vertical axis passing through the scattering sample in the 0° to 45° angular range. This configuration allows for recording 9 IXS spectra at the same time, with a nearly constant q-offset.

Differently from traditional triple axis spectrometers, as a consequence of the extreme backscattering geometry, the energy difference between analyzers and monochromator cannot be varied modifying the Bragg angle of one of the two crystals. The energy scans are therefore performed by changing the relative temperature ΔT of the monochromator with respect to the analyzers. This induces a relative variation of the lattice parameter, $\Delta d/d = \alpha(T)\Delta T$, and therefore a relative variation of the diffracted energy, $\Delta E/E = -\Delta d/d$, is induced as well. Considering for the thermal expansion coefficient, α , a value of $\sim 2.58 \cdot 10^{-6} \text{ K}^{-1}$ at room temperature, the required energy resolution of 10^{-7} - 10^{-8} implies an accuracy in the temperature control of the monochromator crystal in the mK range. This task is achieved with a carefully designed temperature bath, and an active feedback system, which insures a temperature control with a precision of 0.2 mK in the temperature region around 295 K. In order to convert the temperature

scale into the energy, the following temperature dependence of the thermal expansion is used:

$$\alpha(T) = \alpha_0 + \beta\Delta T \quad (2.8)$$

where $\alpha_0 = 2.581 \pm 0.002 \cdot 10^{-6} \text{ K}^{-1}$, $\beta = 0.016 \pm 0.004 \cdot 10^{-6} \text{ K}^{-2}$, $\Delta T = T - T_0(22.5) \text{ }^\circ\text{C}$. From Eq. 2.8 one can precisely calculate the variation of lattice constants at the temperature T:

$$\Delta d/d_0 = \int_{T_0}^T \alpha_0 + \beta(T' - T_0)dT' = (\alpha_0 - \beta T_0)\Delta T + \frac{1}{2}\beta(T^2 - T_0^2) \quad (2.9)$$

Finally, the variation of the diffracted energy, $\Delta E/E = -\Delta d/d$, is easily calculated.

Data Analysis

In general, the IXS spectra from a disordered sample can be formally expressed as:

$$I(q, \omega) = A(q)\omega^{\frac{n(\omega)+1}{k_B T}} S_L(q, \omega) \cdot R(\omega) + b(q) \quad (2.10)$$

where ω is the energy expressed in meV, $S_L(q, \omega)$ is the dynamic structure factor corresponding to the longitudinal modes, $n(\omega)$ is the Bose factor, $A(q)$ is a normalization factor mainly reflecting the q dependence of the atomic form factor and $b(q)$ is a baseline accounting for background noise. In Eq. 2.11 the product $A(q)\omega^{\frac{n(\omega)+1}{k_B T}} S_L(q, \omega) \cdot R(\omega)$ represents the convolution of the theoretical model with the instrumental resolution. This latter is generally measured by performing an inelastic scan on a plexiglass sample at a q corresponding to the maximum of its static structure factor and at low temperature. In such conditions the phonon contribution is extremely weak and only the elastic scattering is thus measured. As in a glass the elastic scattering has no intrinsic width, thus should be a delta function, the shape of the elastic peak thus measured is fully determined by the instrument resolution. The $S_L(q, \omega)$ can be modeled as the sum of a delta function to describe the elastic line and a damped harmonic oscillator model (DHO) for the inelastic component:

$$S_L(q, \omega) = S(q)[f_q \delta(\omega) + (1 - f_q) \frac{1}{\pi} \frac{\Omega(q)^2 \Gamma(q)}{[\omega^2 - \Omega(q)^2]^2 + \omega^2 \Gamma(q)^2}] \quad (2.11)$$

In this expression the parameter f_q is the non-ergodicity factor and corresponds to the elastic to the total integrated intensity ratio. In our analysis procedure, we have convoluted the model directly with the measured instrumental resolution rather than a fit of it. This allows to take into account the asymmetry of the resolution function.

2.2 Numerical Study

In this section, we present the numerical methods that we have used in molecular dynamics for investigating the vibrational and thermal transport properties of a model composite system, made of a nanocrystalline particle of variable size embedded in an amorphous matrix. Sections 2.2.2, 2.2.3 and 2.2.4 detail the methods for preparing the atomic system, calculating the vibrational density of states and dynamical structure factor respectively. Section 2.2.5 illustrates how we have generated and followed the propagation of a wave-packet of given energy in the system, for getting insight into the phonon mean

free path and finally section 2.2.6 describes the Green-Kubo method used for calculating the thermal conductivity of the investigated composites.

2.2.1 Molecular Dynamics (MD)

Molecular dynamics (MD) is a numerical method which allows to simulate real systems at the atomic scale. It provides a temporal description of the atomic positions by solving the Newton's equation of motion for all particles. Among the different algorithms developed to this purpose, the Verlet algorithm [77] is the most largely used thanks to its stability and the assured energy conservation:

$$x(t + dt) = x(t) + v(t)dt + \frac{1}{2m}F(t)dt^2 + o(dt^3) \quad (2.12)$$

$$v(t + dt) = v(t) + \frac{1}{2m}[F(t) + F(t + dt)]dt + o(dt^3) \quad (2.13)$$

Where x, v and F represent respectively the position, the velocity and the forces which describe the dynamics.

2.2.2 Sample Preparation

Our MD simulations were conducted on silicon model systems using homemade FORTRAN programs. The global sizes of the produced samples were between 30 and 100 Å. The large sizes have been used for accessing low phonons wave-vectors and energies, in order to well describe the acoustic vibrational properties. The smallest size was selected to provide a correct diagonalization of the dynamical matrix which requires a small number of atoms (≤ 111). Periodic boundary conditions have been used on the 3 dimensions of space to prevent size effects or evaporation of molecules at the sample boundaries. There exist several potentials describing the covalent bonding such as the Tersoff and the Stillinger-Weber (SW) potentials. In our study, we have chosen the SW potential [78], which is the most suitable one for describing the mechanical properties of silicon [79]. It is based on a two-body term and a three-body term where the total energy of the system can be written as:

$$E = \sum_{i,j} \sum_{i < j} V_2(r_{ij}) + \sum_{i,j,k} \sum_{i \neq j} \sum_{j < k} V_3(r_{ij}, r_{ik}, r_{jk}) \quad (2.14)$$

Where

$$V_2(R_{ij}) = (A_{ij}r_{ij}^{-p_{ij}} - B_{ij}r_{ij}^{-q_{ij}}) \exp\left(\frac{\delta_{ij}}{r_{ij} - a}\right) \quad (2.15)$$

$$V_3(r_{ij}, r_{ik}, r_{jk}) = \lambda_{ijk} \exp\left(\frac{\gamma_{ij}}{r_{ij} - a} + \frac{\delta_{ik}}{r_{ik} - a}\right) (\cos(\theta_{jik}) + \frac{1}{3})^2 \quad (2.16)$$

The angle θ_{jik} is the angle between the bonds that link particles ij and ik . a is the cutoff radius corresponding to $V_2(r_{ij} \geq a) = 0$ and $V_3(r_{ij}, r_{ik} \geq a) = 0$. In this potential, $\cos(\theta_{jik}) = -1/3$, which is the value corresponding to energetically favored positions in diamond-like tetrahedral structure.

To obtain an amorphous matrix, a silicon crystal of 262 144 particles was first melted at a temperature of 3500 K. From the melted state, the liquid was then cooled down to 10K at a quenching rate of 10^{12} K/s. When the sample achieved the right temperature, the energy was minimized using damped dynamics that we describe later in this paragraph. Afterwards, a cubic box was cut from the parent amorphous structure with the desired size. A spherical hole was then created in its center to be filled by the inclu-

sion. In parallel, we prepared a crystalline sphere via the repetition of a diamond like primitive cell. Finally, we merged both amorphous box and crystalline inclusion into a composite structure. At this stage, the bounds at the amorphous/ crystal boundaries were not still established, nor were the new atom positions in the final composite system. For this reason, the sample was thus annealed at 100 K during 100 ps and the energy was minimized once more by means of damped dynamics.

Energy minimization and stabilization The energy minimization is performed using the damped Verlet algorithm, where the particle movements are reduced thanks to the presence of damping forces. The damped dynamics is performed all along the simulation length (several thousand of steps) and allows the whole system to get into a close local minimum of the energy basin. The equation of motion reads:

$$x(t + dt) = 2x(t) - x(t - dt) + \frac{dt^2}{m} F(x(t)) - \gamma v(x) + o(dt^4) \quad (2.17)$$

where γ is the damping parameter, which in our case is $\gamma=0.61$ THz. This value insures the stability of the system and an efficient minimization of energy.

2.2.3 Dynamical Matrix

The dynamical matrix is a harmonic description of the interactions between the particles which constitute the structure. Its eigenvectors and eigenvalues give the normal modes of vibration of the system. In a MD simulation, the equation of motion can be written as:

$$m_i \frac{\partial^2 u_i^\alpha}{\partial t^2} = - \frac{\partial E_{pot}}{\partial x_i^\alpha} \quad (2.18)$$

Where u_i^α denotes the displacement of the i^{th} particle in the direction α and E_{pot} is the potential describing the multi-body interaction, which is a function of the position of all particles: $E_{pot}(x_1 \dots x_N)$. For small particles movements, the force term can be expanded in a Taylor series around the equilibrium positions of all particles x_i^{eq}

$$- \frac{\partial E_{pot}(x_1^x, \dots, x_N^z)}{\partial x_i^\alpha} = - \frac{\partial E_{pot}(x_1^{eq}, \dots, x_N^{eq})}{\partial x_i^\alpha} + \sum_i \sum_\beta - \frac{\partial E_{pot}(x_1^{eq}, \dots, x_N^{eq})}{\partial x_i^\alpha \partial x_j^\beta} (x_j^\beta - x_j^{eq}) + \dots \quad (2.19)$$

By ignoring in the Taylor serie terms with order larger than 2, anharmonic effects may be neglected. We can thus define the dynamical matrix as:

$$M_{ij}^{\alpha\beta} = \frac{1}{\sqrt{m_i m_j}} \frac{\partial^2 E_{pot}}{\partial x_i^\alpha \partial x_j^\beta} \quad (2.20)$$

$M_{ij}^{\alpha\beta}$ thus couples the displacement of the i and j particles in the directions α and β , via the associated variation of the potential energy [80]. Using Eq. 2.20, Eq. 2.18 becomes:

$$\sqrt{m_i} \frac{\partial^2 u_i^\alpha}{\partial t^2} \simeq - \sum_{j,\beta} M_{ij}^{\alpha\beta} u_j^\beta \sqrt{m_j} \quad (2.21)$$

A plane-wave such as $u_i^\alpha = r_i^\alpha \exp i\omega t$ is then a solution of Eq. 2.21 leading to:

$$\sqrt{m_i}\omega^2 r_i^\alpha \simeq \sum_{j,\beta} M_{ij}^{\alpha\beta} r_j^\beta \sqrt{m_j} \quad (2.22)$$

Where $\sqrt{m_i}r_i^\alpha$ denote the eigenvectors of the dynamical matrix. The dynamical problem is then reduced to the problem of finding the $3N$ eigenmodes of the dynamical matrix, whose eigenvalues ω^2 allows determining the vibration frequencies $\omega/2\pi$ of the global system.

2.2.4 Dynamical Structure Factor

From the knowledge of the dynamical matrix eigenmodes, the phonon dispersion curves can be described. It is as well interesting to simulate the dynamical structure factor $S(q, \omega)$, which can be directly compared to experimental data, and from which the phonons lifetime and mean free paths can be extracted, similarly to what we do in an experiment. In order to simulate $S(q, \omega)$, we have used the method developed by Y.Beltukov et al [81]. It consists first in imposing random velocities to all particles and follow their position at each time step of the simulations. It is important to remind that the forces are always governed by the dynamical matrix and the total energy is conserved. Hence, no dissipation or plastic deformation are expected to occur. This results in an output file containing all the positions at each time step of the simulation. Starting from this, we can finally carry out a temporal and spatial Fourier transform on the displacements of all particles which gives the dynamical structure factor:

$$S(\vec{q}, \omega) = \frac{2}{NT} \left| \sum_{i=1}^N \int_0^T \vec{u}(\vec{r}_i, t) \vec{m}_q \exp(-i\vec{q} \cdot \vec{r}_i) \exp(i\omega t) dt \right|^2 \quad (2.23)$$

Here T denotes the total length of the MD run and \vec{m}_q is the polarization vector. By selecting \vec{m}_q parallel or perpendicular to \vec{q} , we calculate respectively the longitudinal and transverse dynamical structure factor. In order to analyze these data, we have followed the procedure already described in Ref. [82]: the simulated $S(q, \omega)$ for several values of \vec{q} has been convoluted with a typical IXS experimental resolution, and then the data have been treated in the very same way as experimental data. A DHO fit has been performed in order to extract the phonon dispersion and energy width. More details will be given in the results section.

2.2.5 Propagation of a Wave-Packet

In this part, we focus on measuring the mean free path (MFP) of phonons, looking directly at the real space propagation of a wave-packet. As a first step, we impose a displacement to atoms belonging to the first 4 Å layer during a MD run such as:

$$\vec{u}(t) = A \exp\left(-\frac{(t - 3t_0)^2}{2t_0^2}\right) \sin(\omega t) \vec{e} \quad (2.24)$$

Where $A = \frac{4.9 \cdot 10^{-3}}{\alpha \omega}$, $t_0 = \frac{3\pi}{\omega}$ and $\alpha = \frac{0.1}{\omega}$.

Depending on the orientation of \vec{e} , longitudinal ($\vec{e} = \vec{e}_x$) or transverse ($\vec{e} \cdot \vec{e}_x = 0$) wave-packets can be calculated separately. The propagation of the displacement energy along the sample allows to compute the total kinetic energy evolution as a function of simulation time and with respect to the distance from

the wave excitation layer ($x = 0$):

$$E(x, t) = \sum_i^N E_i^K(t) \delta(|x_i - x|) \quad (2.25)$$

Where E_i^K is the kinetic energy of the i^{th} atom. As already described in Ref. [82], we analyze the data by plotting $E(x, t)$ for all the timesteps in the course of the simulation. The obtained plot gives the repartition of the kinetic energy with time along the sample at a given frequency ω . At low frequencies, in the propagative regime, the envelope of the energy evolution can be fitted with a decreasing exponential function such as the Beer-Lambert law given by $A \exp(-\frac{x}{l})$, where l corresponds to the MFP of the wave-packet. More details will be given in Chapter 5.

2.2.6 Thermal conductivity calculations: Green-Kubo Method

MD allows to compute the phonon contribution to the thermal conductivity of a model system using equilibrium simulations [83, 84]. The principle relies on Green Kubo formula which is based on the fluctuation-dissipation theorem [85]. It is mathematically expressed as the time integral of the heat flux autocorrelation function.

$$\lambda(t) = \frac{1}{3Vk_B T^2} \int_0^t \langle \vec{J}(t') \cdot \vec{J}(0) \rangle dt' \quad (2.26)$$

Where V is the volume of the system, and J denotes the component of the heat flux vector in a given direction. The expression of the energy flux vector is given as:

$$\vec{J} = \frac{d}{dt} \frac{1}{V} \sum_i \vec{r}_i E_i \quad (2.27)$$

where \vec{r}_i is the position vector of atom i and E_i the energy associated to the atom i (potential plus kinetic), and the sum is over all the atoms in the sample. Thus, the main idea of this method is to compute the heat flux autocorrelation function, which requires following the dynamics of a system over time scales a few times larger than the longest relaxation time describing the dynamics of the system. In our simulations, the relaxation time was 1000 picoseconds. In practice, one needs to record the instantaneous values of the energy flux vector during a time which is roughly ten times the typical decay time of the autocorrelation function. Once the autocorrelation function is constructed, the running integral $\lambda(t)$ may be calculated and the Green Kubo conductivity is identified with the plateau of the running integral (Eq. 2.26). An example of the running integral is reported in Fig. 2.15. To improve the statistics on the determination of the conductivity, one needs to run several independent simulations to obtain different running integrals (typically 10) and averaging the corresponding integrals to obtain a converged value for the conductivity.

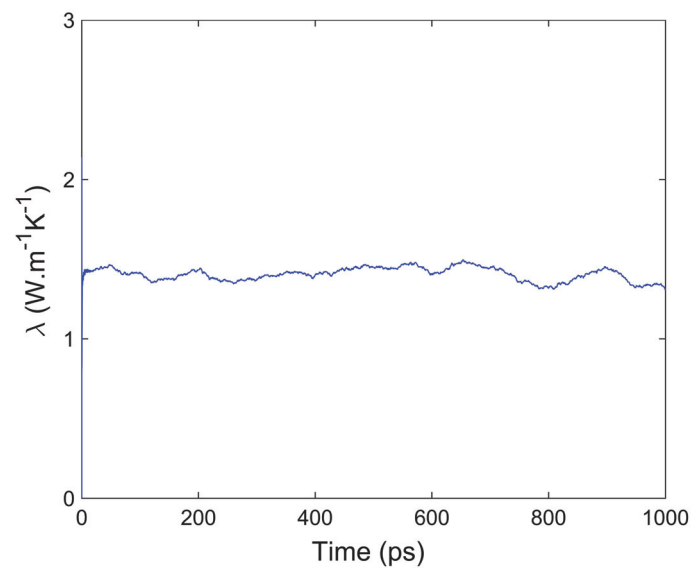


Figure 2.15: The running integral λ as a function of time for a bulk amorphous silicon at 300 K modeled by the Stillinger-Weber potential.

Chapter 3

Transport properties in metallic amorphous/crystalline composites

In this chapter, we present a detailed investigation of the transport properties in a Zr-based bulk metallic glass and how they are modified in the presence of nanocrystalline inclusions. The first section of this chapter is devoted to a brief review of the main physical and transport properties of bulk metallic glasses and their crystalline counterparts. In section 3.2, we describe the experimental tools that allowed to characterize the structure of our samples. In Sections 3.3 3.4 and 3.5 we present our transport properties results, including thermal conductivity, electrical resistivity and phonon measurements. In the last section 3.6 we report an analytical calculation of the thermal conductivity starting from the experimental measurements.

3.1 Bulk Metallic Glasses (BMG)

In the last decades, Metallic Glasses (MG) have aroused as revolutionary materials in a number of structural applications, thanks to their excellent mechanical properties, intimately related to their disordered atomic structure and lack of grain borders and defects [86, 87, 88].

The first MG has been produced in 1960, by fast quench of the binary liquid alloy $\text{Au}_{80}\text{Si}_{20}$ [89]. The very high quenching rate required (10^6 K/s) to overcome crystallization has limited for longtime the development of these materials. Indeed, such quenching rate can be obtained only by melt-spinning the liquid alloy, thus obtaining the metallic glass as a ribbon less than $100 \mu\text{m}$ thick.

More recently, ternary alloys able to vitrify with quenching rates as low as 10^2 - 10^3 K/s have been discovered. Such a low cooling rate can be achieved by the simple injection of the liquid in a macroscopic water-cooled copper mold, thus allowing to produce millimeter or even centimeter-sized MG, called then Bulk Metallic Glasses (BMG).

By the end of the 80's, several bulk metallic glasses were discovered: Mg based [90] and then Zr based [91, 92], Pd based [93] and Fe based [94]. In such systems, the cooling rate went down to 0.1 K/s allowing to synthesize metallic glasses several centimeter long.

Since then, many multicomponent alloys (from 3 to more than 10 elements) have been found that can be vitrified as BMG, opening the way to new perspectives.

Empirically, it has been found that a multi-component metallic alloy can be vitrified as a BMG if four fundamental thumb rules are followed:

- Minimum 3 components are required (5 in most of the cases).
- The components have different atomic sizes (at least 12% of difference).
- The binary/ternary phase diagram present deep eutectics, helping to avoid atomic rearrangements.
- The enthalpy of mixture between the main components is negative.

These 4 characteristics define the glass forming ability (GFA) which define the easiness of vitrifying the liquid alloy and then the thermal stability of the glass. As such, the GFA describes how deep the liquid can be undercooled before vitrification takes place, being then related to $\Delta T = T_x - T_g$ where T_x is the crystallization temperature and T_g is the glass transition temperature.

As presented in chapter 2, the system that we have chosen for the study of a metallic nanocomposite is $\text{Zr}_{52.5}\text{Cu}_{27}\text{Al}_{10}\text{Ni}_8\text{Ti}_{2.5}$. This MG is a bulk metallic glass with a very good GFA, largely investigated for his excellent mechanical properties. Concerning electronic transport properties, this MG belongs to the group 4 of the Mizutani classification, thus presenting an electrical resistivity decreasing with

temperature, as described by the Baym-Meisel-Cote model, and with a residual value at 0 K around $180 \mu\text{Ohm cm}$ [31, 32].

The thermal conductivity of this specific alloy is not reported in literature, however, Zr-based BMG generally present a thermal conductivity in the $5\text{-}15 \text{ W K}^{-1}\text{m}^{-1}$, which weakly increases with temperature, showing two slope changes at the glass transition and at the crystallization temperatures [95].

As previously mentioned, thermal conductivity is the sum of two contributions, one coming from the electrons k_{el} and the other from the atomic vibrations k_{ph} . Despite their disordered structure, MG generally display a thermal conductivity dominated by the electrons as typical for classical metals. Indeed, very small values of $k_{ph} \approx 0.8 \text{ W K}^{-1}\text{m}^{-1}$ have been reported in some studies [96, 97].

3.2 Sample Characterization

The investigation of both electrical and thermal properties in metallic composites requires first a deep understanding of the microstructure of the samples, namely the grain size and distribution of the nanocrystalline inclusions. As previously reported, these properties were studied using X-Ray diffraction (XRD) and Transmission electron microscopy (TEM).

A selection of X ray patterns collected on composites with a crystalline fraction going from 0 to 100% is reported in Fig. 3.1 (a). The growing of broad peaks with crystallization suggests the nanometric nature of the crystalline grains.

It is possible to estimate the amorphous fraction (and thus the crystalline one) in the composite, by directly comparing the XRD pattern collected on the amorphous phase prior to crystallization and the one after the thermal protocol.

The procedure is simplified by the fact that the two patterns were collected on the very same sample and in the same experimental conditions, which means that incident intensity and background signal were the same. As the number and chemical identity of atoms contributing to the signal remains the same, the ratio of the amorphous component in the composite pattern to the total amorphous signal reflects the volumetric amorphous fraction. More specifically, after background subtraction, we superpose the amorphous and composite patterns, and we identify the scaling parameter for which the amorphous signal matches the composite one in the q regions between crystalline peaks, where the intensity comes mostly from the amorphous component (Fig. 3.1 (b)). Considering the noise of the measurement and the precision of such scaling, we estimate that this method gives the volumetric amorphous fraction in the composite within $\approx 5\%$.

Once the amorphous content is known, its signal can be subtracted from the composite pattern in order to get the purely crystalline signal and analyze the crystalline peaks. Contributions from three different crystalline phases can be identified, Zr_2Ni , Zr_2Cu and $\text{Zr}_7\text{Cu}_{10}$, the latter being the major one. From the width of the diffraction peaks, the crystallites size has been estimated by means of the Scherrer method [98] given by the following equation:

$$B = \frac{K\lambda}{L \cos \theta} \quad (3.1)$$

Where L is the peak full width at half maximum in radians (FWHM), λ is the X ray wavelength, K is a dimensionless Shape constant equal to 1 for spherical crystallites, θ is the Bragg angle, and B is the mean diameter of the crystallite.

An example of this analysis is shown in Fig. 3.2 on a fully crystallized sample. The majority of crystalline peaks correspond to a grain size distribution centered at 5 nm with a standard deviation of only

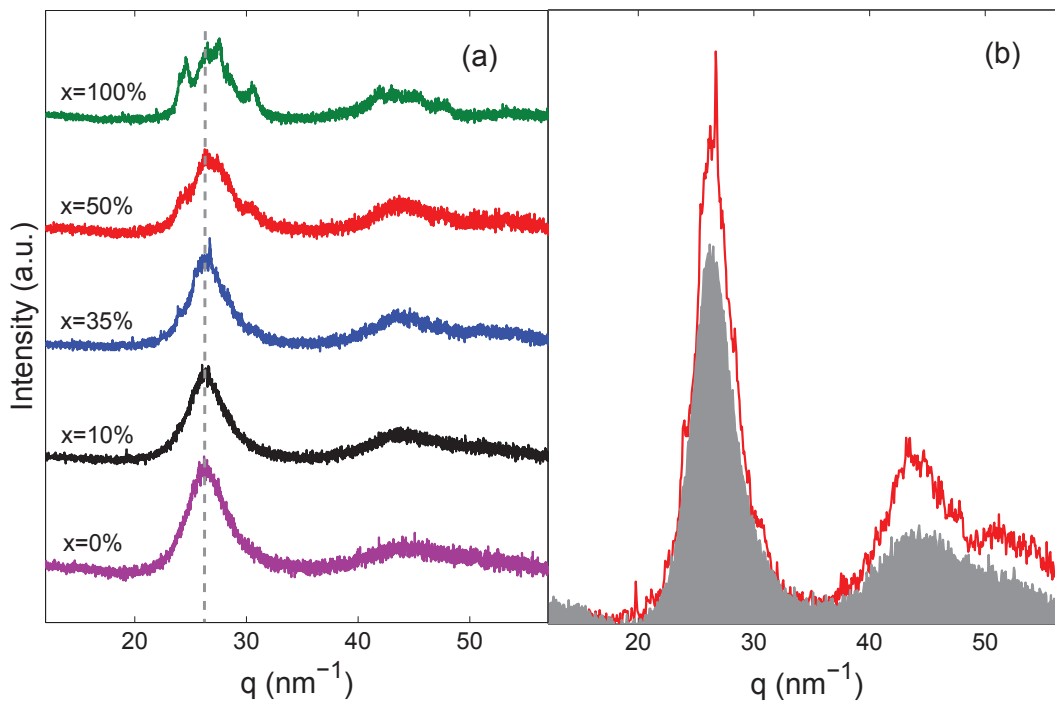


Figure 3.1: (a) X-ray diffraction (XRD) patterns measured at room temperature on samples with different crystalline fraction x (%). The intensity is reported as a function of the scattering wavevector q after background subtraction. The vertical dashed line marks the position of the First Sharp Diffraction Peak q_0 . (b) Estimation of the crystalline fraction from XRD patterns: the amorphous pattern (shaded grey) measured prior to crystallization is scaled until it matches the remaining amorphous contribution in the composite pattern (red). In the reported case, it results $x=35 \pm 5$ %.

1 nm. However, a few narrow peaks indicate the presence of some larger crystallites with 25 nm diameter. Doing the same analysis in our composites, we have found crystallites size in the [5-20] nm range depending on the sample.

In order to confirm the results of our XRD analysis, the same samples, after having performed all the transport measurements, have been investigated by TEM. For each sample, several images were taken along the hole border drilled by the PIPS procedure which has been described in chapter 1, and analyzed in order to extract the total crystalline over amorphous areas, and the size distribution for the observed crystallites. An example of a TEM image is reported in Fig. 3.3, where we find a crystalline volume fraction of 50% and an average grain size of $d \approx 4 \pm 2$ nm, whose distribution is reported in the inset. The results of the TEM investigations were found to be in good agreement with the XRD estimates, as well as with the predicted DSC crystalline fractions.

3.3 Thermal transport in metallic composites

As first thing, the room temperature thermal conductivity of the metallic glass, a fully crystalline sample and a composite with 30% crystalline fraction has been measured by scanning thermal microscopy (SThm) [73, 74]. No difference could be assessed within the experimental uncertainty, as large as 25%, due to the intrinsic uncertainty of the method and to the surface roughness. Indeed, we found a thermal conductivity of $k_T = 5 \text{ WK}^{-1}\text{m}^{-1}$ in the glass and 4.6 and 4.7 in the composite and polycrystal respectively. Such a low value in the fully crystalline sample is surprising, and can be understood in terms of

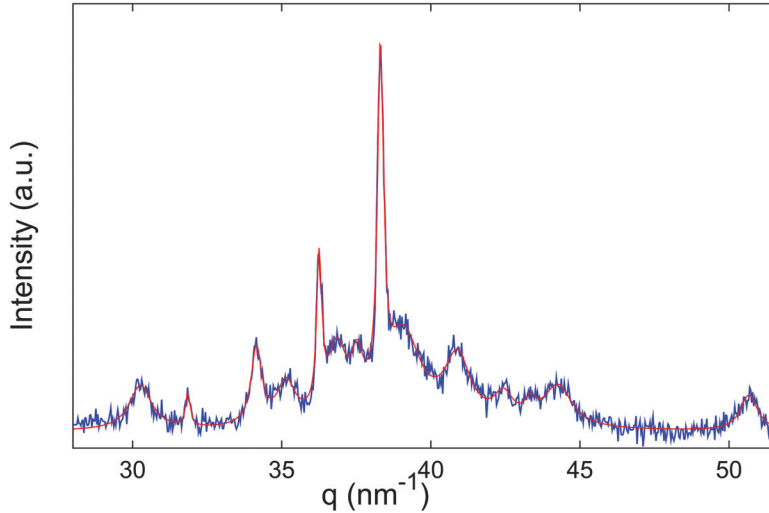


Figure 3.2: Analysis of XRD spectrum of a fully crystallized sample. The major grain size distribution obtained here were 5 ± 1 nm with a presence of bigger crystallites with ≈ 25 nm of diameter.

a heat transport dominated by grain boundaries scattering in the nanometric polycrystal, decreasing its thermal conductivity towards the amorphous value. The crystalline fraction-independence, on the other hand, suggests a negligible effect of a partial nanocrystallization on the thermal transport, at least for a crystalline fraction of 30%.

As previously mentioned, the total thermal conductivity is the sum of two contributions, one coming from the electrons, k_{el} , and the other from the atomic vibrations, k_{at} . One could thus wonder whether a lucky compensation of opposite trends in the two contributions could lead to a crystallinity-independent thermal conductivity. In order to disentangle the interface and partial nanocrystallization effect on the two contributions, we have performed a separate detailed investigation of both.

3.4 Electrical contribution

The electronic contribution is intimately linked to the electric conductivity, the Wiedemann-Franz law assessing their proportionality for simple systems: $k_{el} = \frac{LT}{\rho}$, with $L = 2.45 \times 10^{-8} \text{ W } \Omega \text{ K}^{-2}$ the Lorenz number, T and ρ temperature and electrical resistivity respectively. While this law is not universally valid, the Lorenz number possibly being different and temperature dependent, its validity in metallic glasses has been confirmed in several cases [57, 95, 96, 99] with the given value for L .

We have thus investigated the electrical resistivity of the amorphous, the fully crystalline and the composite samples between 50 and 300 K for getting insight into the electronic contribution. First of all, we focus on the temperature dependence of the resistivity in the fully amorphous sample and its absolute value at room temperature. As reported in Fig. 3.4, the amorphous exhibits a decreasing electrical resistivity pointing to $\rho = 179.4 \pm 0.5 \mu\text{Ohm cm}$ at room temperature.

As already said, our system belongs to the fourth group of the Mizutani classification and the temperature dependence of the electrical resistivity is described by the Baym-Meisel-Cote theory [100], giving

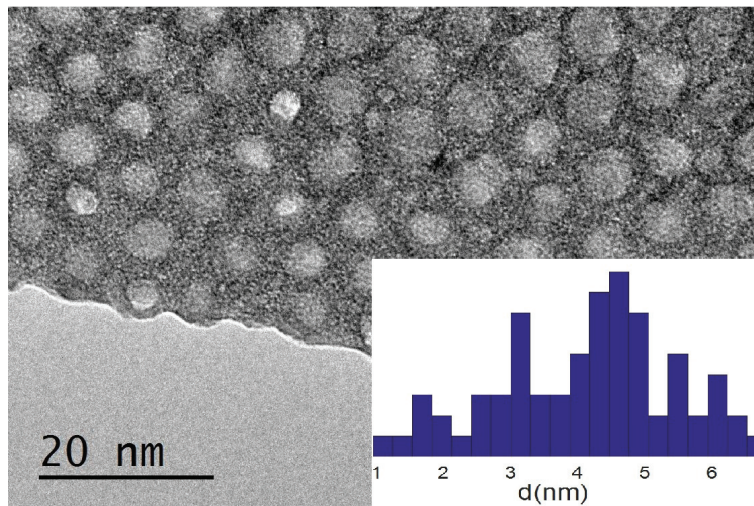


Figure 3.3: Dark field TEM image collected in a composite with crystalline fraction $x=50\%$; from the analysis of the image the crystalline diameters distribution is obtained and shown in the inset, with a crystallite mean diameter $d \approx 4 \pm 2$ nm.

$\rho(T) = (\rho_0 + \alpha T)e^{-W}$, with ρ_0 the residual resistivity at $T=0$ K and W the Debye-Waller factor. A negative temperature dependence can here be expected for temperatures above ≈ 20 K, due to the main role played by the Debye-Waller factor [31, 32]. This is actually the case, as it is shown in Fig. 3.4 where the electrical resistivity is linearly fitted by the Baym-Meisel cote model. We can quantify the strength of its temperature dependence through the Temperature Coefficient of the Resistivity, defined in chapter 1, which here is $\text{TCR} = -2.19 \cdot 10^{-4}$. We focus now on the fully crystalline and the composite samples. The observed temperature and crystalline fraction dependencies are reported in Fig. 3.5 (a) and (b).

Looking at the temperature dependence, it can be seen that all samples but the fully crystalline one display a negative dependence, the resistivity decreases with temperature, as it can be quantified via the TCR reported in Fig. 3.5 (c).

Inversely, the resistivity of the fully crystalline sample exhibits the normal metal-like temperature increase, with a linear dependence typical for polycrystalline materials with nanometric grains, due to the dominant interface effect [101]. From the negative Temperature Coefficient of Resistivity in all composites, we can thus conclude that electronic transport is dominated by the matrix even for crystalline fractions as large as 50%.

Moreover, the room temperature resistivity decreases with the crystalline fraction, but with a total decrease of only 20% from amorphous to fully crystalline sample.

Such a small difference is surprising. Indeed, in several literature works it is reported that the resistivity decreases by more than 2 orders of magnitude at the crystallization when the crystalline system is made of micrometric grains. We can understand such discrepancy on the basis of the nanocrystallinity in the fully crystallized sample, giving raise to a grain boundary dominated transport.

The behaviors of $\rho(x)$ and the Temperature Coefficient of Resistivity are rather smooth, revealing no enhanced interface effect such as the one reported in Ref. [65], where interface scattering caused a maximum in the electrical resistivity at small crystalline fractions. The behaviors here look in fact quite linear, suggesting that a simple Effective Medium Theory (EMT) could capture the mechanisms at play. Indeed, we could reproduce both dependencies using the EMT model introduced in chapter 1. Applying such theory to the case of an amorphous matrix with embedded crystalline particles, the following

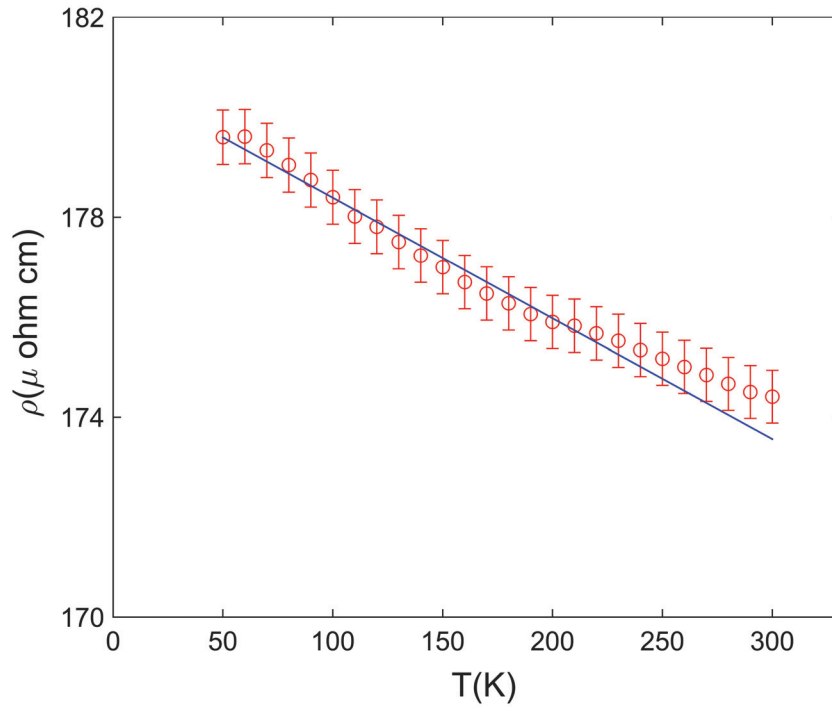


Figure 3.4: Temperature dependence of electrical resistivity in the fully amorphous sample. The fit with the Baym-Meisel-Cote model is also reported as a blue line

equality is obtained:

$$x \frac{\sigma_c(T) - \sigma_e(T)}{\sigma_c(T) + 2\sigma_e(T)} + (1 - x) \frac{\sigma_a(T) - \sigma_e(T)}{\sigma_a(T) + 2\sigma_e(T)} = 0; \quad (3.2)$$

where x is the crystalline fraction, σ the electrical conductivity and subscripts c , a and e stand for crystalline, amorphous and effective medium.

For the two phases, we use the measured values of the temperature dependence of the electrical conductivity $\sigma(T) = 1/\rho(T)$ for the glass and the fully crystalline sample. This choice corresponds to the idea that the crystalline component being made of nanometric grains, its electrical conductivity is given by the one measured on a polycrystal with nanometric grains. In this sense σ_c implicitly includes the effect of the finite size on the electric transport of isolated nanometric grains.

With this assumption, Eq. 3.2 gives a calculated electrical resistivity and TCR in a very good agreement with our measurements, as can be seen in Fig. 3.5 where they are reported as dashed lines. Moreover, the model allows us to estimate $x_c = 60\%$ as the critical value of crystallinity for which the crystalline part starts to dominate over the matrix, causing the change of sign in the TCR.

3.5 Phonons contribution

The understanding of the partial nanocrystallization effect onto the vibrational contribution to thermal conductivity requires a microscopic investigation. Indeed, the vibrational thermal conductivity cannot be experimentally directly accessed, unless the system is insulator so that the total thermal conductivity coincides with the vibrational one. However it is possible to measure the phonon individual properties in a given energy range by means of inelastic scattering techniques, and estimate the right side of

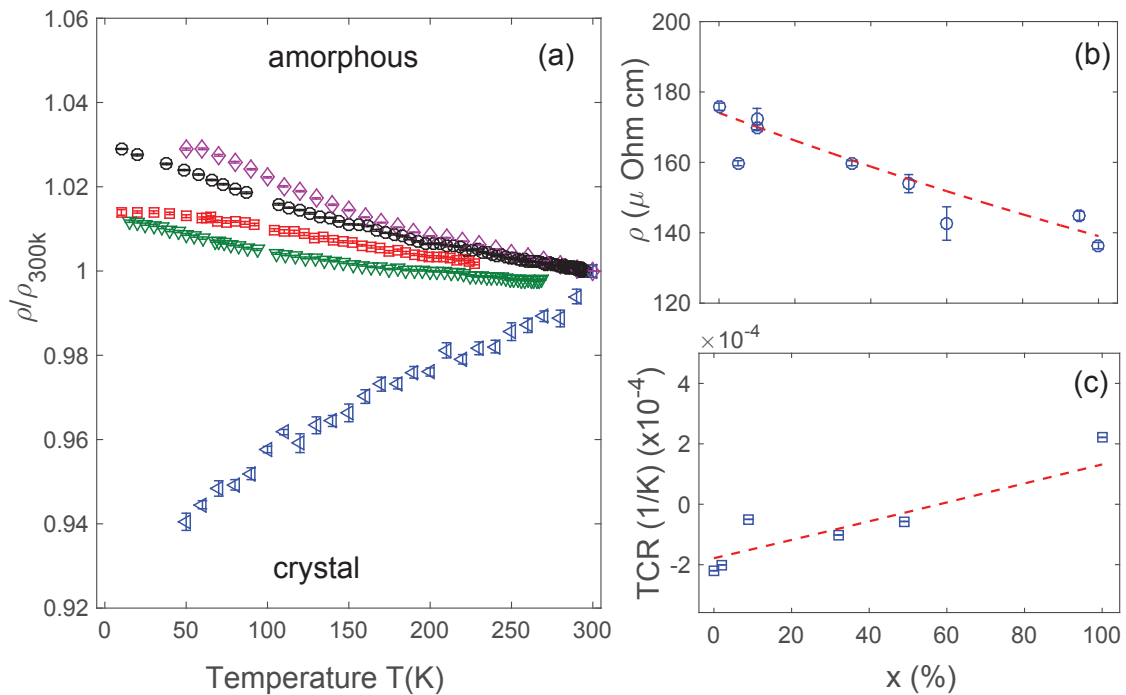


Figure 3.5: **Electrical Resistivity** (a) Temperature dependence of electrical resistivity renormalized at the room temperature value, for the amorphous (violet), crystalline (blue) and some representative composite samples with $x=35\%$ (black), $x=10\%$ (red), $x=60\%$ (green). (b) Room temperature electrical resistivity as a function of crystalline fraction. The prediction of the effective medium theory is reported as a dashed line. (c) Evolution of the Temperature Coefficient of Resistivity (see text) as a function of crystalline fraction. The prediction of the effective medium theory is reported as a dashed line.

the phonon contribution to the thermal conductivity which, as already described in chapter 1, can be expressed as an integral over all phonon frequencies:

$$k_{at} = 1/3 \int_0^{\omega_{max}} C_v(\omega)v(\omega)^2\tau(\omega)g(\omega)d\omega; \quad (3.3)$$

with $C_v(\omega)$ and $g(\omega)$ the phonon specific heat and density of states. We have thus performed an inelastic X ray experiment collecting data on three samples: an amorphous, a fully crystalline and a partially crystallized one with $x=30\%$. A total of 27 q-points was measured per sample up to the maximum of the static structure factor, $q_0 = 26 \text{ nm}^{-1}$.

It is now largely accepted that in a disordered system a pseudo-Brillouin zone can be identified with $q_0/2$ marking its border. Concerning the polycrystalline sample, the first strong diffraction peak allows similarly to identify an orientationally averaged pseudo-Brillouin zone, which is pertinent for the comparison with the amorphous dynamics data [102]. A selection of spectra of the three samples is reported in Fig. 3.6, for positive energy transfer, and after subtraction of the elastic line. As it can be seen, the inelastic excitation remains well defined, although broad, up to very high momentum transfer.

Data have been analyzed using the Damped Harmonic Oscillator (DHO) model, presented in chapter 1, for the inelastic excitation and a delta function for the elastic line, convoluted with the experimental resolution [21].

In all samples, two inelastic excitations were needed to fit data for $q \geq 7 \text{ nm}^{-1}$, while in the partially and fully crystalline samples up to three modes were needed in the second pseudo-Brillouin Zone

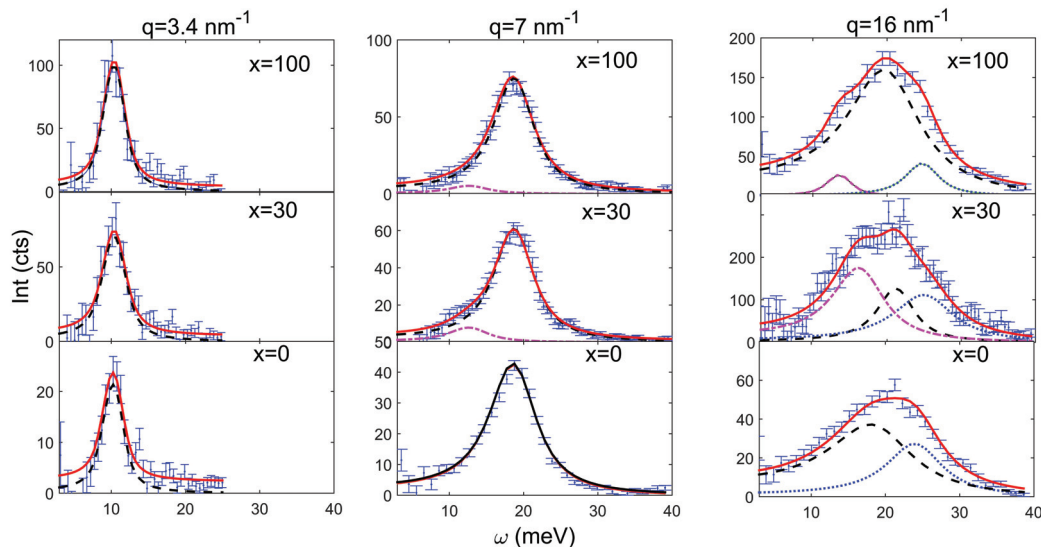


Figure 3.6: IXS spectra collected at three different momentum transfer q in the fully amorphous ($x=0$, bottom line), partially crystalline ($x=30$, middle line) and fully crystalline ($x=100$, top line) samples, after elastic line subtraction. The first 2 columns correspond to q values in the first pseudo-Brillouin zone, the right column to a q lying in the second pseudo-Brillouin zone. The red line corresponds to the fit with a multi-modes model, whose components are also reported in black, magenta and blue. Details are in the text.

($q \geq q_0/2$). The highest energy mode was ascribed to a longitudinal excitation, while the lower ones to transverse-like excitations.

The fact that we can easily identify only one longitudinal and one transverse mode in the first pseudo-Brillouin zone in the polycrystal is not trivial. It is known that in a polycrystal the measurement should yield the orientational average of phonons belonging to all existing branches with the same polarization, and the broadening corresponds to the width of the branches distribution [103, 102]. One single mode per polarization should thus be observed in the first pseudo-Brillouin zone for a single-phase polycrystal with randomly oriented grains. In presence of several phases, as it is the case here, more branches could be observed, one per crystalline phase and per polarization. The observation of only one longitudinal and one transverse mode in the first pseudo-Brillouin zone is thus an indication that phonon dynamics is dominated by the major crystalline phase.

3.5.1 The high frequency dynamics of the metallic glass

We first compare the high frequency longitudinal sound velocity of the amorphous sample with the low frequency value, as measure by ultrasound technique by our collaborators at SIMaP in Grenoble. As it can be seen in the left panel of Fig. 3.7, the amorphous sample exhibits a positive dispersion, in the sense that the low- q limit of its sound velocity (as measured at high frequency here) is higher than the macroscopic limit as measured by ultrasound techniques at low frequency.

As mentioned in chapter 1, discrepancies between high frequency and low frequency sound velocity have already been reported in several glasses [21, 29, 104] and ascribed to the existence of nanometric elastic heterogeneities or relaxation processes [105].

Looking now to the transverse modes which are reported in the right panel of Fig. 3.7, we observe also

for the transverse mode a positive dispersion of the glass speed of sound, much stronger than in the longitudinal case, in agreement with recent calculations [105].

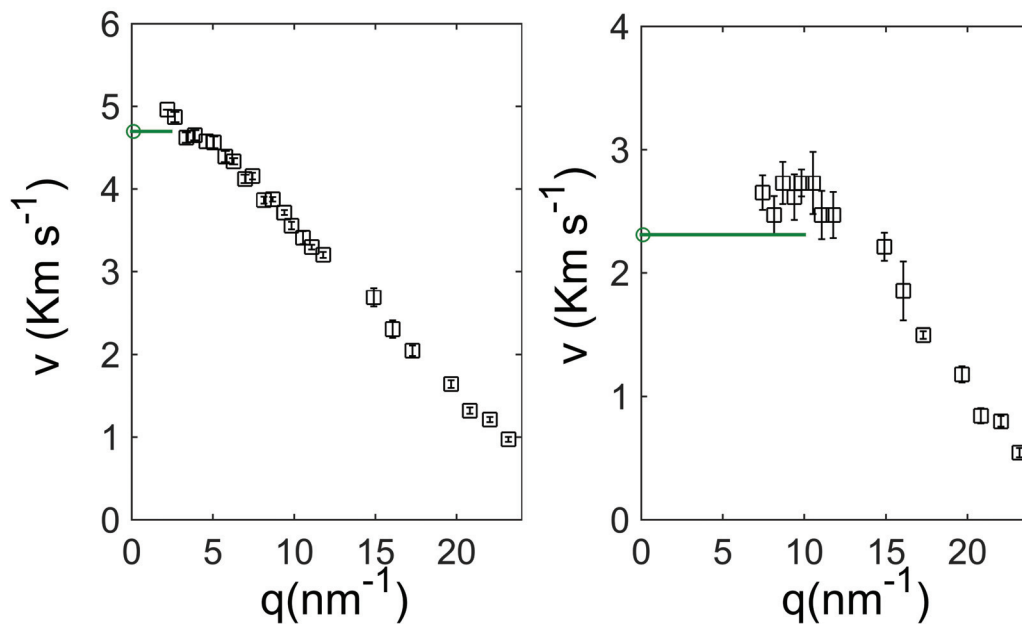


Figure 3.7: Acoustic sound velocity in the fully amorphous sample (black squares) measurement by IXS. Left panel: longitudinal modes. Right panel: transverse modes. The green circle corresponds to the ultrasound value, while the horizontal green line is just a guide to the eye, to better evidence the positive dispersion.

3.5.2 Phonon dynamics in amorphous/nanocrystalline composites

In the following session we focus on the effects of a partial nanocrystallization on the dynamics of the glass.

3.5.2.1 Longitudinal Modes

The respective phonon velocities and broadening are reported in Fig. 3.8 and 3.9 for the three samples: the amorphous, the crystalline and the partially crystallized one.

No difference among the three samples is observed over the whole explored q -range, indicating that the longitudinal moduli of the three samples are very similar in the investigated lengthscale, which leads to the conclusion that they have similar local orders and similar inter-atomic forces.

Concerning the longitudinal phonon broadening, it increases in the first half of the pseudo-Brillouin Zone, before the appearance of the transverse acoustic excitation, then it starts to flatten out. While in the glass this is inversely proportional to phonon lifetime as far as phonons are not overdamped and we don't enter the microscopic regime, this is not true in the polycrystal, where broadening is related to the branches separation. It is thus surprising that the broadening in the polycrystal is only slightly smaller than in the glass, the difference being more marked in the second pseudo-Brillouin zone. This suggests that in our polycrystal an additional broadening contribution is present, due to an enhanced phonons scattering from grain boundaries, as well as from the existence of contributions from the minor solid phases. The phonon broadening in the composite is indistinguishable from the amorphous case within

error bars in the whole explored q -range.

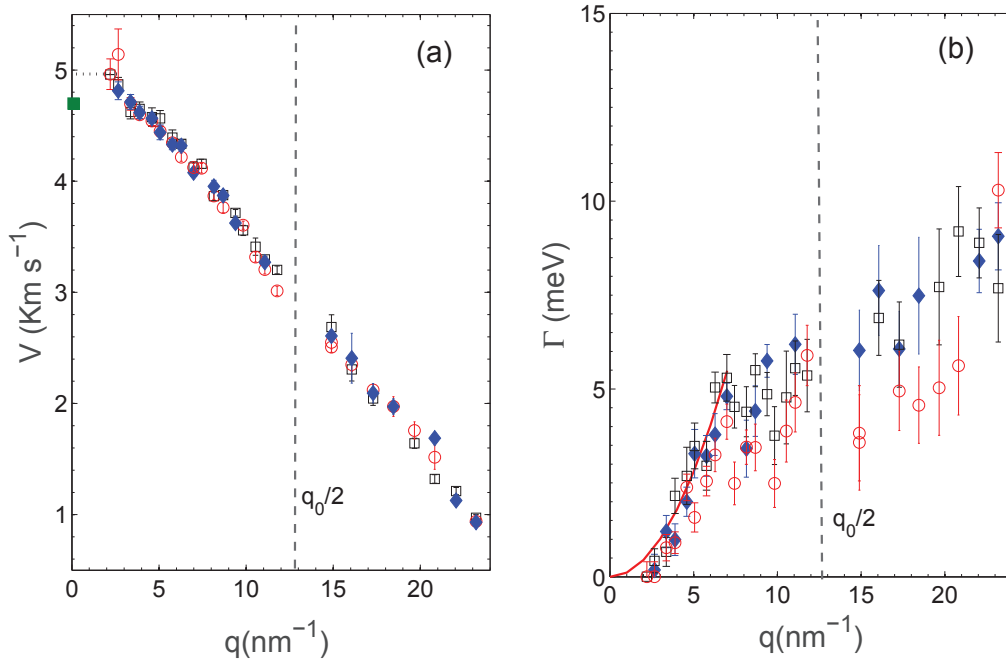


Figure 3.8: Longitudinal sound velocity (a) and phonon broadening (b) as a function of wave vector q : for the amorphous sample (black squares), the fully crystalline sample (red circles) and a composite with $x=30\%$ (blue full diamonds). A vertical dashed gray line marks the pseudo-Brillouin zone border. (a): The macroscopic longitudinal sound velocity for the amorphous sample measured by ultrasound technique is also reported as a green square. The low q limit of the amorphous longitudinal speed of sound, as extrapolated from high frequency data, is marked with a horizontal dotted line. (b): the red solid line corresponds to the fit of amorphous data to a q^2 behavior.

3.5.2.2 Transverse modes

We focus first on the first Brillouin zone. Differently from the longitudinal case, composite and polycrystal display for $q \leq 10 \text{ nm}^{-1}$ a higher transverse speed of sound with respect to the glass, resulting in a macroscopic shear modulus about 12% higher. Many literature studies report on the increase of macroscopic elastic moduli in metallic glasses upon crystallization, showing that the main effect is on the shear modulus. However, the strength of such increase strongly depends on the thermal protocol and final grain size in the crystallized alloy [106, 107, 108]. Therefore, our results allow to access a direct information on the shear modulus hardening at different lengthscales, going from macroscopic ($q \rightarrow 0$) to the atomic scale ($q \approx q_0$). Surprisingly, such hardening is observed only on a macroscopic scale, while at microscopic distances ($q \geq 10 \text{ nm}^{-1}$, corresponding to $r \leq 6$) the three systems elastic moduli are indistinguishable from each other. This result is in agreement with the findings of recent structural investigations in metallic glasses and composites under uniaxial compression, exploiting novel analysis methods to access the strain spatial distribution, and thus the local elastic moduli [109, 110].

Concerning the phonons broadening, no difference is detectable within the experimental uncertainty, which is rather large due to the difficulty of fitting the low energy modes because of a high elastic signal.

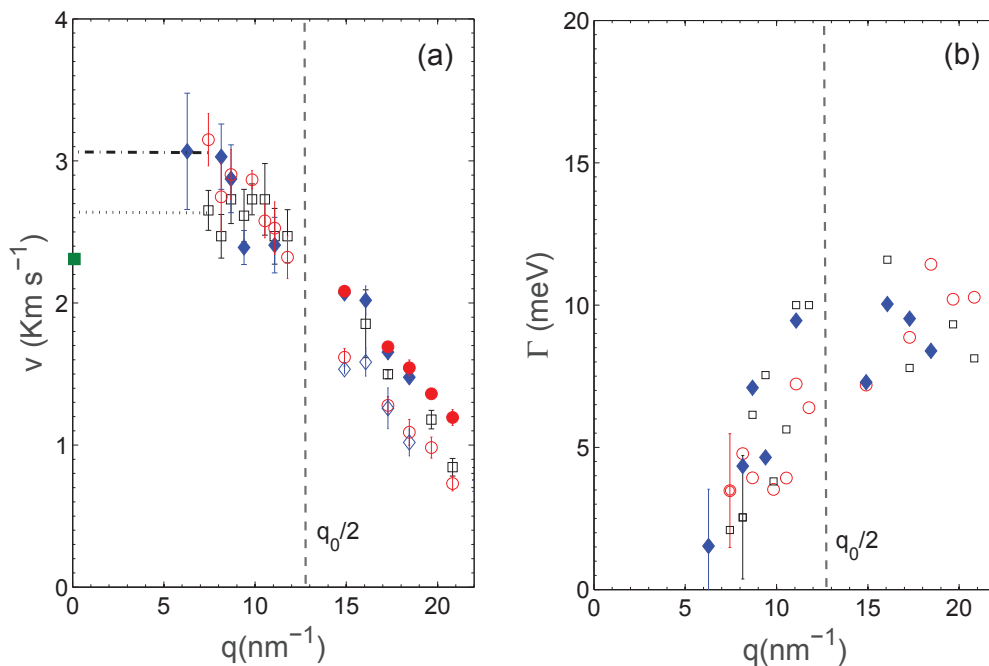


Figure 3.9: Transverse sound velocity (a) and phonon broadening (b) as a function of wavevector q for the amorphous (black squares), the fully crystalline sample (red circles) and a composite with $x=30\%$ (blue full diamonds). A vertical gray dashed line marks the pseudo-Brillouin zone border. (a): In the second zone, full and empty red circles and blue diamonds correspond to the two transverse modes of the fully and partially crystalline samples respectively. The macroscopic transverse sound velocity of the amorphous sample measured by ultrasound technique is also reported as a green square. Horizontal lines mark the low q limit for the transverse speed of sound in the glass (dotted line) and the polycrystal and composite (dot-dashed line) as extrapolated from high frequency data (b): A representative error bar on the broadening is reported only for one data point per dataset for better visual clarity. Data for the partially and fully crystalline samples in the second zone correspond to the sum of the two transverse modes width in this zone, to be compared with the width of the single transverse mode in the glass.

We focus now on the second pseudo-Brillouin zone. We report in Fig. 3.10 the transverse acoustic dispersion, for a better visualization of the transverse dynamics. The appearance of two transverse-like excitations for the crystalline and the composite samples is quite surprising.

This could be understood in terms of a strong elastic anisotropy of the major crystalline phase, mostly affecting the transverse dynamics, where the orientational average gives then raise to two major contributions, as illustrated in the case of the α -cristobalite polymorph of SiO_2 in Ref. [103]. In order to confirm this interpretation DFT ab-initio calculations of the lattice dynamics of the crystalline phase would be needed, however this remains beyond the scope of the present work.

From Fig. 3.10 it can be noticed that the glass transverse mode lies between the two transverse modes of the polycrystal, indicating that the elastic anisotropy is washed out by the overall disorder. Still, some residual elastic anisotropy remains, as we can deduce from the phonons width looking to the panel b of Fig. 3.9. Here, for the polycrystal and the composite, we report the single mode width only in the first zone, while in the second zone, where two modes are present, we have chosen to report the sum of their widths. It can be seen that such sum corresponds roughly to the width of the transverse phonon in the glass. This means that the amorphous phonon, via its width, spans the whole branches distribution of

the inelastically anisotropic polycrystal, thus keeping such anisotropy, meaning that the same anisotropic local order is present in the amorphous.

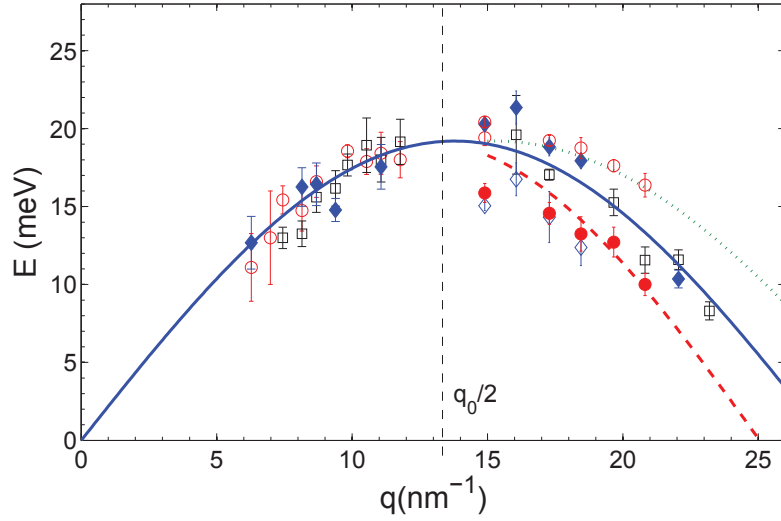


Figure 3.10: Transverse acoustic dispersion for the glass (black square), the polycrystal (full and empty red circles) and the composite (full and empty blue diamonds). The solid line is a sinusoidal fit of the glass data, dotted and dashed line describe the two transverse branches of the polycrystalline and composite samples in the second zone.

3.6 Total Thermal conductivity

Electric and phonons measurements allow us to calculate the electronic and phonon contributions to the thermal conductivity. We first focus on the metallic glass, where, using the Wiedemann-Franz law, we can calculate an electronic contribution of $k_{el} = 4.20 \pm 0.02 \text{ W K}^{-1} \text{ m}^{-1}$, e.g. $\approx 84\%$ of the total thermal conductivity, confirming that this is the dominant heat transport channel, as observed in other metallic glasses [95, 96, 97].

For estimating the phonon contribution, we need first of all to assess the propagative character of the measured modes. For the longitudinal modes, we find that in the whole explored energy range it is $\Gamma < \omega/2\pi$, thus the Ioffe-Regel limit is not reached and longitudinal phonons keep a propagative character over the whole first pseudo-Brillouin zone. As for transverse modes, the opposite is true, the Ioffe-Regel limit being at $q = 7 \text{ nm}^{-1}$. Nevertheless, we decide to use Eq. 3.3 to get a first rough estimation of the phonons thermal conductivity, considering that the transverse phonons width remains close to such limit, bypassing it only by 30% at the highest energy point.

We calculate the integral of Eq. 3.3, using all experimental data measured in the first pseudo-Brillouin zone. In order to do so, we first fit the experimental acoustic dispersions to analytical laws, which allow us to get an analytical expression for the energy dependence of the phonon sound velocities and then estimate the longitudinal and transverse densities of states and the specific heat [111]. Specifically, we fit the longitudinal dispersion to a sinusoidal behavior, $\omega_L(q) = 24.3(2) \sin(\pi q/q_0)$, and the transverse one to a linear behavior for $q \leq 10 \text{ nm}^{-1}$, $\omega_T(q) = 17.2q$, and sinusoidal above, $\omega_T(q) = 19.2(4) \sin(\pi q/q_0)$. The normalization condition for acoustic branch allows us to determine the upper limit to be used in Eq. 3.3 for longitudinal and transverse modes, $\omega_{max}^L = 24.3 \text{ meV}$ and $\omega_{max}^T = 17.5 \text{ meV}$.

We then fit the phonon damping to a quadratic energy dependence for the transverse mode, $\Gamma_T(\omega) = 0.023\omega^2$, while a multi-regime dependence can be observed for the longitudinal broadening. Indeed, data lying below 12 meV escape from a quadratic fit and point more to an ω^4 dependence, consistent to what observed in many glasses at energies close to the Boson Peak [21, 22, 112, 113], which in similar metallic glasses lies in the 5-10 meV range, and in the parent vitreloy MG, Vit4, is at 5 meV [114]. In our energy range, we thus model the longitudinal broadening as $\Gamma_L(\omega) = 0.00009\omega^4$ up to 12 meV, $\Gamma_L(\omega) = 0.013\omega^2$ for $12 \leq \omega \leq 20$ meV and $\Gamma_L(\omega) = 5.2$ meV for $\omega > 20$ meV.

If we limit the integral of Eq. 3.3 to the experimentally investigated energy range [5–25] meV, a phonon thermal conductivity contribution of only $0.44 \text{ W K}^{-1}\text{m}^{-1}$ is found. In order to estimate the total contribution, we need to extend the integral down to zero energy, thus making a strong hypothesis on the phonon broadening below our experimental energy range. The ω^4 dependence is known to be limited to a narrow energy range around the Boson Peak, we thus assume that our lowest energy point marks also the lower limit of such behavior, and we recover the ω^2 law for lower energies. With this approximation, a total phonons contribution of $0.8 \text{ W K}^{-1}\text{m}^{-1}$ is calculated, corresponding to $\approx 16\%$ of the total (electronic plus phononic) thermal conductivity.

The contributions to the thermal conductivity coming from the different energy ranges here described can be appreciated from Figure 3.11 (a), where we report the room temperature cumulative thermal conductivity $k(\omega, T)$, defined as $k_{at}(\omega) = 1/3 \int_0^\omega C_v(\omega)v(\omega)^2\tau(\omega)g(\omega)d\omega$ normalized to the total integrated thermal conductivity k_T , together with the separate longitudinal and transverse contributions. It can be here appreciated that about 50% of the total thermal conductivity comes from phonons in our experimental energy range. Increasing approximately linearly with the energy, the slope changes to a slower increase at about 9 meV, reflecting the entering in the ω^2 regime for the longitudinal attenuation, followed by a second slowing down, due to the end of the transverse branch. Looking to the corresponding integrands, as reported in Fig. 3.11 (b), it is clear that the contribution from longitudinal phonons is drastically reduced from the ω^4 dependence of the phonon attenuation, in the Boson Peak energy range, while the transverse contribution is basically constant over the whole energy range, due to the assumed simple ω^2 dependence.

At this point, it is important to remind the strong approximations behind our calculation: 1) we haven't modeled the positive dispersion in the speed of sound, thus slightly overestimating the macroscopic speed of sound, but also neglecting its effects on the calculated density of states [21]; 2) we have overlooked the very complex energy dependence of phonons lifetime in a glass, with our simplistic modeling of the longitudinal and transverse broadening, especially for this latter, having used a single quadratic dependence over all energies. As it can be seen from Fig. 3.11 (b), the introduction of an ω^4 dependence would dramatically reduce the transverse contribution; 3) we have assumed transverse phonons as propagative over the whole energy range, while our experimental data lie above the Ioffe-Regel limit. Despite such approximations, the calculated value is well consistent with our calculated electronic contribution and the measured total thermal conductivity, confirming once again that the electronic contribution dominates thermal transport in this glass.

Looking now to the effects of partial and full nanocrystallization on the total thermal conductivity, from the relative weight of electronic and phonon contributions, it is clear that any change related to this latter will be almost negligible. We can quantify it, knowing that the relevant effect of crystallization is only an increase of the transverse speed of sound of $\approx 6\%$ in the first pseudo-Brillouin zone, while phonons lifetime is basically unaffected. Such change enters Eq. 3.3 through the phonon velocity and density of states, leading to a phonon-related change in the total thermal conductivity of less than 2%.

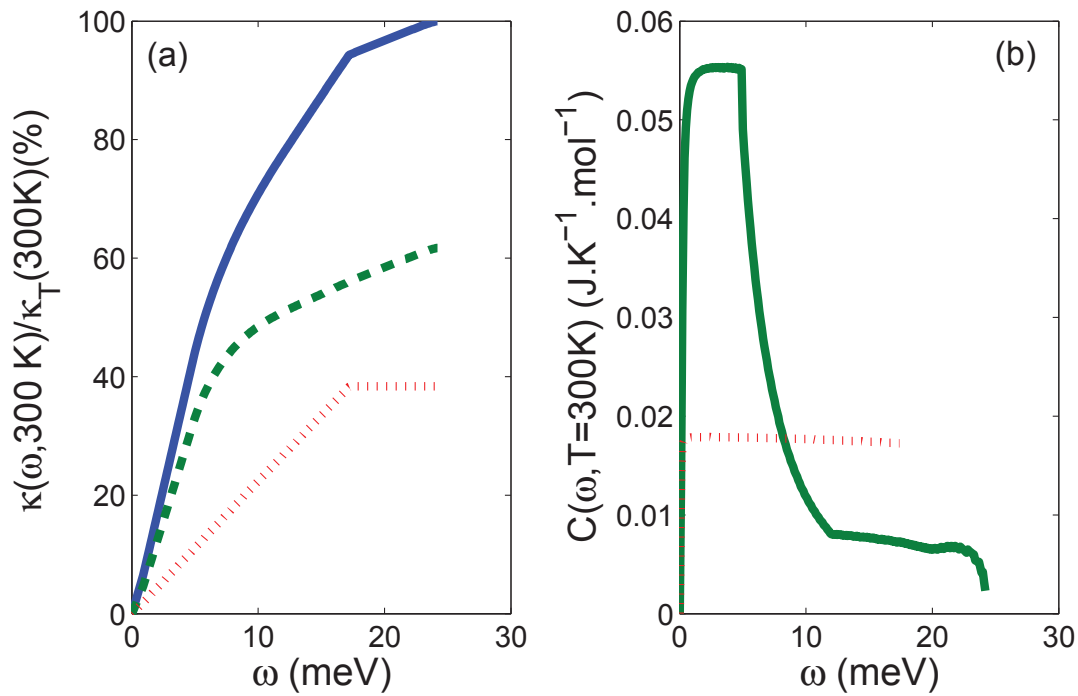


Figure 3.11: (a): The cumulative thermal conductivity at 300 K is reported as a function of ω , normalized to the total thermal conductivity k_T (300 K) as a solid line. The separate contributions from longitudinal and transverse modes are reported as dashed line and dotted line respectively. The slope changes reflect the changes in the longitudinal slope and the end of the transverse branch. (b) Longitudinal (solid line) and transverse (dotted line) contributions to the integrand of Eq. 3.3 as a function of the phonon energy ω . The dramatic reduction of the longitudinal integrand due to the ω^4 dependence of the phonons attenuation is clearly visible between 5 and 9 meV.

The effect is much more important on the electronic contribution, where the linear decrease of the resistivity results in a linear increase of the electron-related total thermal conductivity of about 15%. Such change, though substantial, is smaller than the experimental uncertainty on our measured values of thermal conductivity, which explains why we could not detect it. Electric measurements are therefore a reliable tool for investigating the effect of nanocrystalline inclusions in metallic glasses on their thermal transport properties, thanks to the higher precision available on electronic measurements with respect to thermal measurements.

3.7 Discussions and conclusion

In this chapter we have presented an experimental study of the thermal conductivity in amorphous/nanocrystalline metallic composites by investigating its two contributions: electronic and vibrational one. The electronic contribution is assessed by measuring the electrical resistivity which decreases linearly with the crystalline volume fraction and is weakly affected by presence of nanocrystalline inclusions pointing to 20% of total change from the amorphous to the fully crystallized sample. This result suggests that no enhanced electrons scattering from the interfaces is observed in the range of crystalline fractions and grain sizes here investigated.

Concerning the vibrational contribution, we find that a partial nanocrystallization of about 30% leads to an increase of the transverse acoustic speed of sound in the first Brillouin zone, which reflects into

an increase of the total thermal conductivity, but of only 2%, remaining a negligible contribution in this metallic system.

The fully crystalline sample on the other hand exhibits a high electric resistivity and important phonon broadening, which result in electric and thermal transport properties very close to the parent MG, likely due to the dominant effect of grain boundaries scattering in nanometric grains as well as scattering from a kind of disorder on the mesoscopic scale, given by the mixture of three solid phases.

Chapter 4

Transport properties in chalcogenide amorphous/crystalline composites

While the previous chapter has been devoted to study the transport properties in metallic composites where the presence of inclusions do not seem to have a considerable effect, this chapter deals with composites based on chalcogenide glasses, characterized by a huge contrast of properties between the inclusion and the matrix.

The first section of this chapter is devoted to a review of structural and physical properties in chalcogenide glasses and their crystalline counterparts in addition to their transport properties. In the second section, we show the structural properties of the samples employed in this chapter. In the third section, we present the transport measurements performed on crystalline GeTe and discuss the effect of carbon (C) doping on them. Finally, we will present and discuss the effect of a partial nanocrystallization on electric and vibrational properties of C-doped GeTe.

4.1 Chalcogenide Glasses

The materials investigated in this chapter are based on chalcogenide glasses (CG) e.g. a class of inorganic amorphous materials containing one or more chalcogen elements: S, Se or Te, which belong to the family of phase change materials (PCM), characterized by an amorphous phase stable at room temperature on a years-long time scale [115].

PCM show a great potential in applications such as rewritable optical data storage devices, electronic non volatile memories and neuromorphic hardwares [116], exploiting a combination of two unique properties:

- a very high speed of crystallization (order of nanoseconds): the atomic rearrangement required on recrystallization proceeds on a very fast timescale of ten to one hundred nanoseconds [115, 117, 118]. Generally this fast crystallization is ascribed to the strongly temperature dependent viscosity of the liquid phase approaching the glass transition temperature [119, 120] and to the simple crystalline structure [121].
- A usually high contrast between amorphous and crystalline phase in their optical and electrical properties compared to metals, ionic compounds or ordinary sp_3 -bonded semiconductors.

Most materials fulfilling the above criteria have been found to be located in the stoichiometric triangle of Germanium (Ge), Antimony (Sb) and Tellurium (Te) shown in Fig. 4.1 and as such, they are referred to as GST materials.

For our study we have chosen to work with a simple binary glass, the GeTe, owing to its well understood atomic structure and large thermal stability, thanks to a high crystallization temperature.

4.1.1 GeTe compound

The amorphous phase of GeTe is characterized by an alternation of Ge and Te atoms in both tetrahedral and distorted octahedral environments [123]. Ge-Te bond length was determined to be around 2.6 Å [124] and the presence of homopolar Ge-Ge bonds was confirmed by means of Monte Carlo simulations and X-ray diffraction experiments [125]. Amorphous GeTe crystallizes at $T_c=485$ K into a rhombohedral phase (space group R3m) stable at room temperature [126, 127], which can be viewed as a distorted rocksalt structure along the [111] direction [128]. In this phase, Ge and Te are sixfold coordinated by each other with subsets of three shorter (2.83 Å) and three longer (3.15 Å) bonds [129, 130]

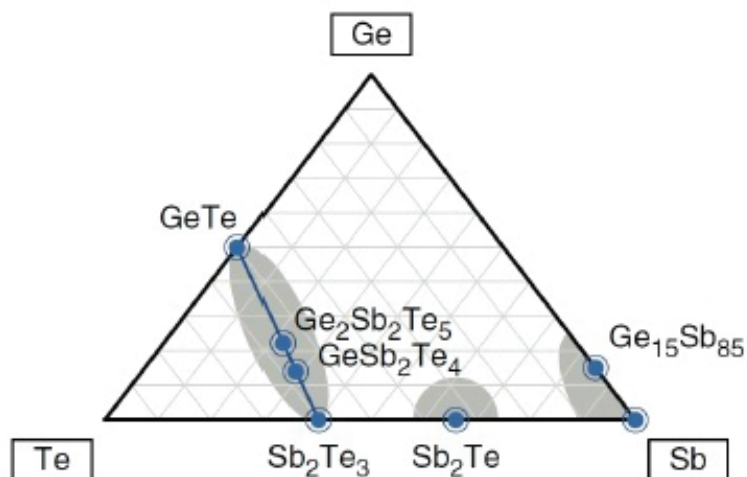


Figure 4.1: Phase Change materials reported on the ternary Ge:Sb:Te phase diagram.
Taken from [122]

often described as a Peierl distortion where the bonding is insured by p-orbitals. It has been found that the fast crystallization process induces structural defects, such as the presence of homopolar Ge-Ge bonds, and the germanium segregation, yielding to a large number of vacancies [131].

Rhombohedral GeTe is ferroelectric and undergoes a ferroelectric-to-paraelectric transition at a Curie temperature of $T_c=705$ K. The nature of this transition is still a matter of controversy, being described either as a displacive transition to a rocksalt phase without distortion [132, 133, 127] or as an order-disorder transition with randomly distributed local distortions [134]. We don't enter into the detail of such debate as it is out of the scope of our work.

4.1.2 Carbon-doped GeTe (GeTeC)

It has been found that doping GeTe by carbon [131, 135] or by nitrogen [136, 137] results in an increase of the crystallization temperature. In the case of carbon doping, this was ascribed to the deep modification of the amorphous structure in presence of carbon. Indeed, while, similarly to GeTe, strong chemical order between Ge and Te and short Ge-Te bonds are present, Ghezzi and coworkers have shown that strong changes at the second neighbors level take place [135]. Here C centered tetrahedral and triangular units appear with the formation of long carbon chains. Breaking the C-C bonds in such chains is an extremely endothermic process which could act as a barrier to crystallization [135]. Concerning crystalline GeTeC, some XRD studies [138, 139] investigated the structural changes induced by carbon doping, reporting that GeTeC with carbon content lower than 10%at. crystallizes in a rhombohedral structure, like pure GeTe. But for C concentration higher than 10 %at. the structure becomes more and more cubic and the distortions vanish. Moreover, the grain size was found to drastically decrease with C doping from more than 100 nm in pure GeTe down to 20 nm [140]. A structural refinement aiming to identify the position of carbon atoms in the crystalline phase has not been done however. Recent studies, based on optic spectroscopies such as Fourier-Transform Infrared (FTIR) and Raman, indicate that C-Ge or C-Te bonds, present in the glass phase, disappear upon crystallization. This suggests that C migrates out of the GeTe crystalline grains, cumulating at the grain boundaries, likely limiting their

growth, similarly to what reported in carbon doped $\text{Ge}_2\text{Sb}_2\text{Te}_5$ [141].

4.1.3 Electronic properties

Electronic transport in amorphous GeTe takes place through a variable range hopping mechanism at low temperatures, changing to a Poole-Frenkel mechanism ($\log \sigma \simeq 1/T$) above 200 K with an activation energy for conduction being equal to half the band gap. This is indicative of a Fermi level pinned in the midgap, a characteristic of chalcogenide glasses. The Seebeck coefficient is positive, typical of a p-type conduction. The existing values in literature are reported on thin films and range between $S=600 \mu\text{V/K}$ [142] and $S=880 \mu\text{V/K}$ [143] at room temperature.

Amorphous GeTe displays two striking electronic properties, as it is also the case in other PCM which are highly relevant for their applications. The first one is the so-called "threshold switching". This term denotes a phenomenon taking place at a distinct electrical "threshold" field $E_t \approx 10^6 \text{ V/m}$ at which the initially high resistivity is dramatically reduced by orders of magnitude and a conductive state is created. This state can be maintained unless the field falls below the holding field $E_h < E_t$ [115]. Presently, there are no commonly accepted explanations for this phenomenon. Instead, some models suggest that the decrease of the resistivity is associated to trap kinetics [144], other models propose an increasing carrier mobility [145, 146] or field induced crystalline nucleation [147, 148] to be the physical origin of this effect.

The second one is the so-called "resistivity drift", e.g. the fact that the electrical resistivity in the amorphous phase increases with time t after the amorphization [149]. This drift is usually associated to the on-going structural relaxation and it is empirically described by a power law $\rho \propto (t/t_0)^\gamma$ with $\gamma \sim 0.1$ at room temperature [150].

Crystalline GeTe is a p-type degenerate semiconductor, which means that the Fermi energy resides in the valence band, close to the valence band maximum [151, 152], giving raise to a metallic-like conduction. This p-type behavior was ascribed to the presence of a high concentration of Ge vacancies (8-10%) as the most easily formed intrinsic defects at equilibrium which represent a native p-type doping with hole concentration typically higher than $5 \times 10^{19} \text{ cm}^{-3}$. It was explained by Edwards et al [151] by density functional calculations which revealed that intrinsic defects like Ge vacancies form empty states at the top of the valence band forcing the Fermi-level to shift into the valence band and leading thus to the degeneracy. It was shown that the dominant contribution to the electrical resistivity at low temperatures comes from temperature independent carrier-defect scattering while at high temperature carrier-phonon scattering will become important.

The Seebeck coefficient is still positive in crystalline GeTe with a relatively low value in bulk GeTe at room temperature $S \sim 30 \mu\text{V/K}$ [153] compared to thin films where it becomes $\approx S=80 \mu\text{V/K}$ [143]. The effect of C-doping on the electronic properties of GeTe is the subject of our study and will be presented later in details.

4.1.4 Thermal properties

Few studies reported measurements of the total thermal conductivity at 300 K for thin films of GeTe in the amorphous and crystalline phases. The amorphous phase has a very low thermal conductivity $k_T \sim 0.2 \text{ W K}^{-1}\text{m}^{-1}$, similar to other chalcogenide glasses [154, 136]. As expected, this value is larger in the crystalline phase where the reported data are scattered between 1.6 and $6 \text{ W K}^{-1}\text{m}^{-1}$ [154, 136, 155]. Such a large spread of values in the crystalline phase has been ascribed to a different content of defects, namely the Ge vacancies, which depends on the growth process and is difficult to estimate and control.

Crystalline GeTe exhibits a decreasing thermal conductivity with increasing temperature (higher than 300 K) and the total value is dominated by the electronic contribution [155].

The phonons contribution to the thermal conductivity in crystalline GeTe at room temperature has been calculated and reported to spread from 0.1 to 4.1 W K⁻¹m⁻¹, following the spread of total thermal conductivity values. C-doping has been recently found to dramatically affect thermal transport in the crystalline phase. Indeed Kusiak and coworkers reported the first experimental measurements of the thermal conductivity of C-doped GeTe thin films, measured by means of a modulated photo thermal radiometry technique. While the thermal conductivity of the amorphous is basically unaffected, in the crystalline films it is found to decrease by a factor as large as 10 with respect to pure crystalline GeTe, independently on the C-content [140].

This is in contrast with the case of N-doped GeTe where it was found that N-doping could reduce the thermal conductivity only by a factor of 2 [136].

4.1.5 Vibrational properties

The vibrational properties of amorphous GeTe have been largely investigated by optical spectroscopy techniques, giving insights on the local structure [156]. As for acoustic vibrational properties, more interesting for the understanding of thermal transport, and measurable with inelastic neutrons or x-rays techniques, to our knowledge nothing has been reported yet.

The situation is different for the crystalline phase, for which an extended database of optic and acoustic vibrational properties, measured by Raman spectroscopy [156] and nuclear inelastic scattering [157], exists, in addition to several computer simulations [158].

Pure GeTe displays a narrow phonon energy range remaining below 25 meV and an acoustic energy limit of about 12 meV. From density of states calculations, Pereira et al [157] reported a Debye sound velocity of 1900 m s⁻¹.

As for C-doped GeTe, calculations have shown that C-doping induces a strong decrease of the vibrational density of states in the low frequency range (below 12 meV). It also induces a reduction of the Boson Peak, likely related to an increased network rigidity [137].

4.1.6 PCM as potential thermoelectric materials

Crystalline PCM have recently attracted a novel interest for another kind of application than the memory storage. Indeed their relatively low and tunable electrical resistivity together with a quite low thermal conductivity makes them interesting materials for thermoelectric applications.

Thermoelectric applications exploit the capacity of a material, subject to a temperature gradient, to convert this latter into an electric tension (in the case of generator) or inversely (in the case of refrigerator). These transformations benefit from the Seebeck and Peltier effect respectively.

The efficiency of thermoelectric materials is typically described by the temperature dependent and dimensionless quantity ZT , defined as:

$$ZT = \frac{S^2}{\rho k_T} \cdot T \quad (4.1)$$

where S is the Seebeck coefficient, defined as the ratio between the electric potential generated by a temperature gradient and this latter, $S = \frac{\Delta V}{\Delta T}$, ρ is the electrical resistivity, k_T is the thermal conductivity

and T is the temperature in Kelvin. The ZT equation can be written differently as:

$$ZT = \frac{P}{kT} \cdot T \quad (4.2)$$

Where P denotes the power factor. Hence, the challenging task to obtain high ZT materials resides in achieving simultaneously high electronic conductivity (low electrical resistivity), high Seebeck coefficient and a low thermal conductivity in the same material. So far, the state of the art of ZT points to a value close to 1. This is illustrated in Fig. 4.2. which is taken from a review on thermoelectric materials by Sootman et al [159].

Interestingly, many thermoelectric materials contain the same elements as typical PCM, which attracted more attention to them. All Telluride-based materials show good values of ZT in the high temperature range, from 300 K to 900 K.

In most cases, doping and alloy engineering approaches are used to optimize the structural stability and thermoelectric properties of GeTe, such as $\text{Bi}_2\text{Te}_3/\text{GeTe}$ [153], PbTe/GeTe [160] and SnTe/GeTe [161]. Given the recent results by Kusiak et al [140] on the surprisingly low thermal conductivity of GeTeC, the crystalline phase of the system here investigated promises to represent a huge improvement on the thermoelectric potential of GeTe without any complex engineering. In this work, we aim thus to clarify the thermoelectric potential of fully and partially nanocrystallized GeTeC.

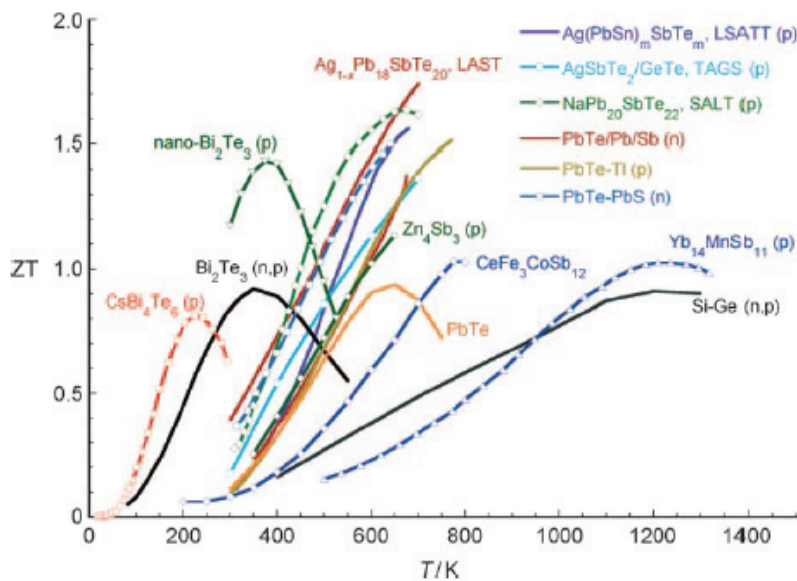


Figure 4.2: Temperature dependence of the thermoelectric figure of merit ZT in a selection of state of the art thermoelectric materials. Taken from [159]

4.2 Sample preparation and characterization

We first present here the investigation of fully crystalline GeTeC samples, with respect to fully crystalline GeTe. The aim of this work was first of all to understand the role of carbon on structure and properties of crystalline GeTeC.

4.2.1 Sample preparation

The as-prepared films were amorphous, and as such, electrically insulators. Crystallization was then induced by annealing the samples in air, monitoring the resistivity as a function of temperature by means of a four points probe. As it can be seen in Fig.4.3 the resistivity changes during the thermal protocol by many orders of magnitude at the crystallization. C-doping induces a shift of the crystallization temperature, increasing the temperature range of stability of the glass, as previously reported in Refs. [131, 135].

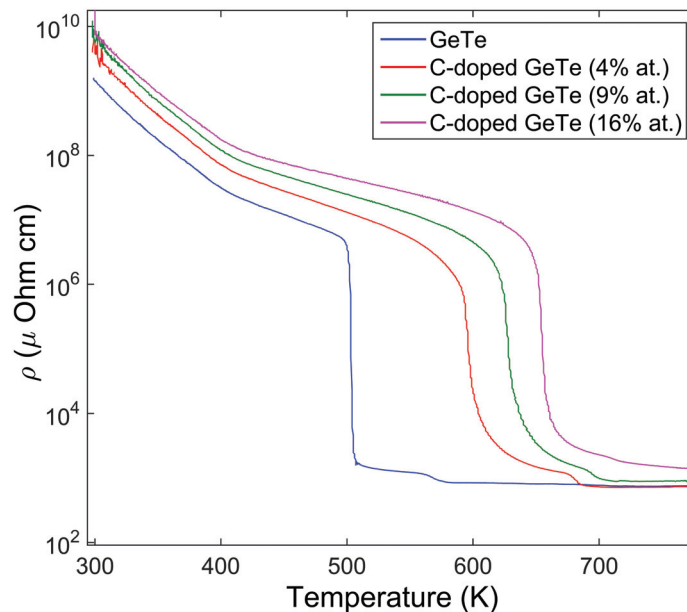


Figure 4.3: Evolution of electrical resistivity as a function of temperature during crystallization of GeTe and C-doped GeTe thin films.

4.2.2 Structural characterization

The structural characterization by means of XRD on samples from the same batch as ours was already previously reported in Ref. [140]. Such data, as mentioned in section 4.1, show the disappearance of the rhombohedral distortion with increasing C-content.

In order to get a better insight into the differences in crystalline structure due to C-doping, we have investigated the structure of an amorphous and a crystalline sample with 9% at. C-content by means of high resolution synchrotron based XRD. Such measurements were carried out at the diffraction station of Beamline ID28 (ESRF) using an X ray beam with 10^{12} ph/s intensity in a $50 \mu\text{m}$ spot on the sample at an energy of 23.7 keV.

The XRD spectra reported in Fig. 4.4 show no signature of texturing. They were further analyzed using the Scherrer formula [98] in order to obtain the grain sizes. An average grain size of $\approx 18\text{nm}$ was found, confirming previous reports in Ref. [140].

In the inset, a zoom of the two lowest peaks is reported. The lowest angle one, at $\sim 13.8 \text{ nm}^{-1}$, is the peak which in a rhombohedral structure should be splitted in two peaks. Here it is a single peak, suggesting thus that at this carbon content there is no rhombohedral distortion, in agreement with literature. Still, due to the broad peak, it is difficult to definitely rule out such distortion, which could be hidden by the nanometric grain induced peak broadening.

As for the peak at about 14.5 nm^{-1} , it corresponds to the [111] peak of pure Germanium. Similarly to

pure GeTe, in GeTeC as well crystallization causes a partial Ge segregation, in contradiction with what was generally thought. The difference is that here Ge is nanocrystalline, as the broad peak demonstrates, while in pure GeTe, it can precipitate in micrometric crystals.

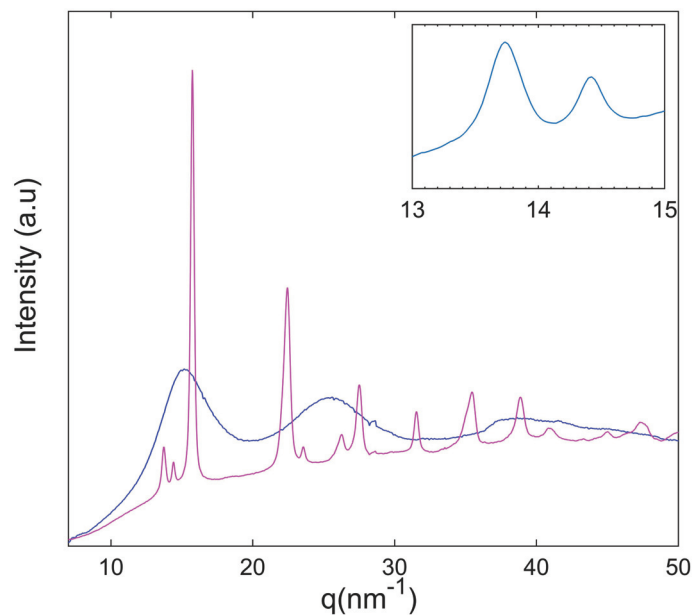


Figure 4.4: XRD pattern of a fully crystallized GeTeC sample (magenta) and amorphous sample (blue) with 9%at. carbon content. The inset shows a zoom on the doublet peak around q 14 nm^{-1} , which indicates the presence of rhombohedral distortions

Additional structural informations can be obtained with optical Raman spectroscopy. We have thus investigated a crystalline pure GeTe and GeTeC 9%at. samples by low-frequency Raman spectroscopy at room temperature. The excitation laser had a wavelength of 532 nm, and the spectrometer used was a LabRAM HR Evolution Raman Spectrometer, from Horiba Scientific, at the Centre Commun de Microspectrometrie Optique (CECOMO) in Lyon. The laser power was reduced to 1% of the normal power by the introduction of filters, in order to reduce the sample heating, when investigating the low frequency region. As for the high frequency region, explored for highlighting the presence of C-C vibrational signatures, a weaker filter (5%) was used in order to have a more intense signal.

The low frequency data are reported in Fig. 4.5 (left panel). We find a striking similarity between the two samples, suggesting no relevant difference between their vibrational properties. Moreover, a narrow peak at $\approx 300 \text{ cm}^{-1}$ confirms the presence of isolated Ge in both samples.

The right panel of Fig. 4.5 reports the frequency region around 1500 cm^{-1} for GeTeC. This is the region where phonon modes relative to C-C bonds appear. Not only we do observe them, but also they have the typical spectral appearance as in amorphous carbon [162], suggesting then the presence of amorphous carbon in our crystalline sample.

Such results would be compatible with the suggestion by Kusiak et al [140] of an amorphous carbon segregation to GeTe grain boundaries.

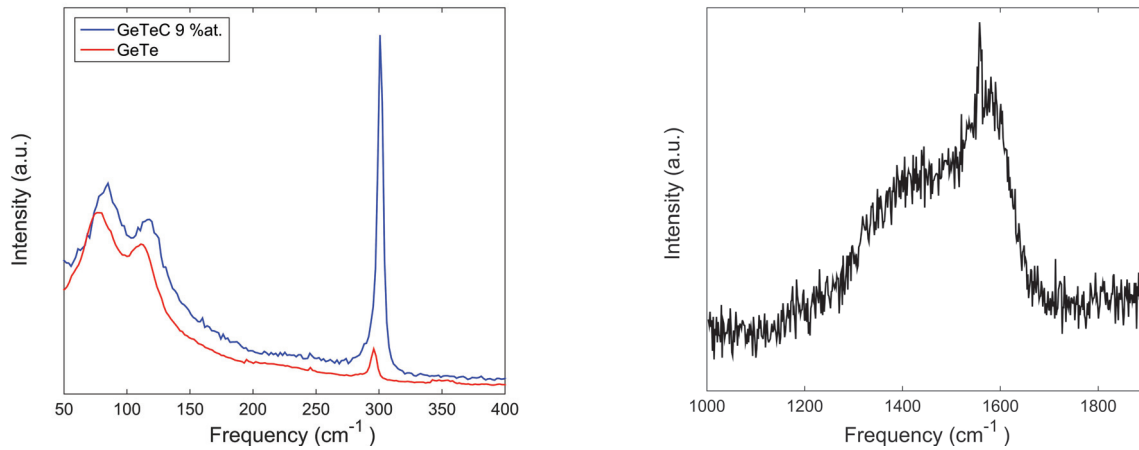


Figure 4.5: Low frequency raman spectra of GeTe and GeTeC(left panel). Raman spectrum of GeTeC at high frequency(right panel) indicating a typical amorphous carbon appearance.

With the aim of shedding light onto this question, we have performed a TEM investigation of crystalline GeTeC 9%at. The crystalline sample was polished using Focused Ion Beam (FIB) procedure. The TEM measurements were conducted by our collaborators at the CEA LETI using FEI TITAN Ultimate apparatus. An example of TEM images is reported in Fig. 4.6, where a grain size in the 10-20 nm range can be appreciated, confirming XRD results. Within the sensitivity of the technique, we did not observe any signature of carbon in crystalline grains but only on the grain boundaries, as it can be seen in Fig. 4.7 where a color map of carbon signal is reported.

For the first time, we thus demonstrate that amorphous carbon do segregate during crystallization, precipitating to the grain borders. This means that GeTeC samples are indeed composites made of core shells particles, where the core is the crystalline GeTe grain and the shell is amorphous carbon. We also note a Germanium condensation around the crystalline grains in agreement with XRD and Raman results on the presence of isolated Ge.

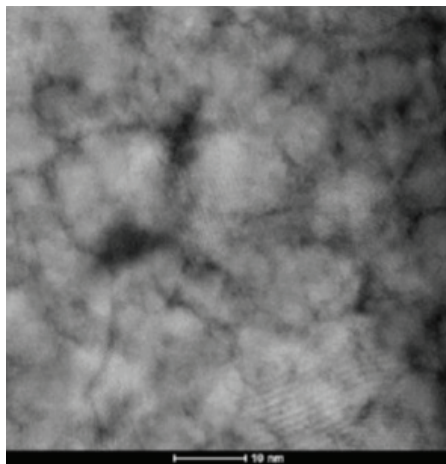


Figure 4.6: TEM images of a fully crystallized GeTe sample doped with 9%at. of carbon annealed at 773 K. The carbon doping induces a reduction of grain size. Here the mean diameter obtained is ≈ 20 nm

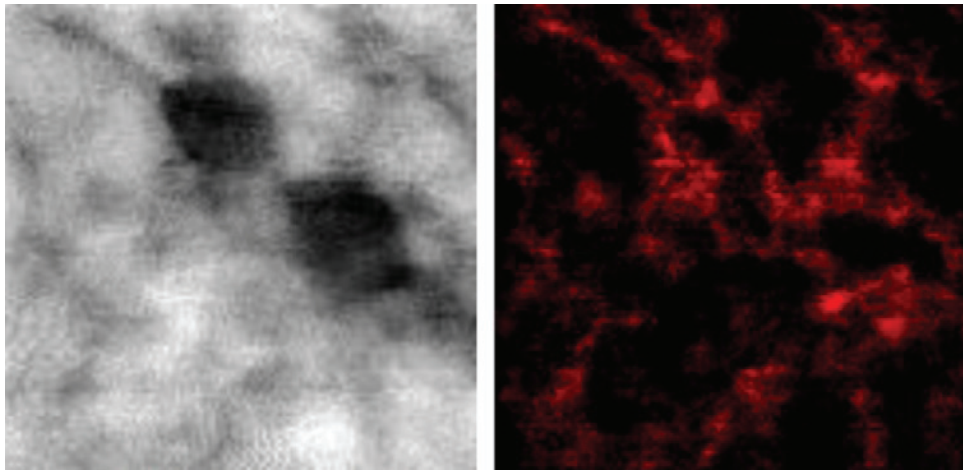


Figure 4.7: Left: TEM image of a selected region in the 9%at. C-doped GeTe. Two crystalline grains are clearly visible. Right: Image obtained by means of electron energy loss spectroscopy of the same region as in the left panel. Red color corresponds to presence of carbon. It can be seen that it concentrates on grain boundaries.

4.3 GeTe Versus carbon-doped GeTe

Our structural characterization has shown that fully crystalline GeTeC is in fact an amorphous/crystalline nanocomposite made of two different materials: crystalline GeTe and amorphous carbon. As such this is an ideal system for investigating transport properties in nanocomposites. By tuning the C-doping, we will tune the amorphous content.

In section 4.3.1 we report and discuss the effect of C-doping on the electrical resistivity and Seebeck coefficient. Section 4.3.2 will be devoted to the calculation of the power factor P in order to gain additional informations about the potential of these materials in thermoelectric applications.

4.3.1 Electrical properties

4.3.1.1 Results

In Fig. 4.8 we report electrical resistivity measurements in pure GeTe and carbon doped samples in the temperature range between 10 and 570 K. For the highest C-doping, we have reported data on two samples, prepared at two different annealing temperatures. The low temperature data were obtained using the Van Der Pauw method, while the higher temperature ones were measured using a four points probe in air. As it can be seen from the figure, the low and high temperature data are in good agreement within the uncertainty due to different experimental conditions.

Looking to the temperature dependence reported for $T < 300$ K in Fig. 4.9, crystalline GeTe exhibits a linear and positive TCR in the whole temperature range. This behavior is in agreement with the expected metallic-like conduction present in a degenerate p-type semiconductor, as mentioned in section 4.1.3.

As for GeTeC samples, the TCR vanishes for the lowest amount of carbon doping (4% at.) before it becomes negative for samples with C-content higher than 9% at., which indicates a change in the nature of conduction from metallic to insulator. Moreover, the 16% at. doped sample displays a strongly negative TCR, together with very high electrical resistivity, which however are both reduced with an annealing to higher temperature. Hence, two phenomena are here present. The first one is the appearance of some kind of transition from metal to insulator-like behavior with C-doping and the second one is an effect of annealing on both absolute value of the electrical resistivity and its TCR.

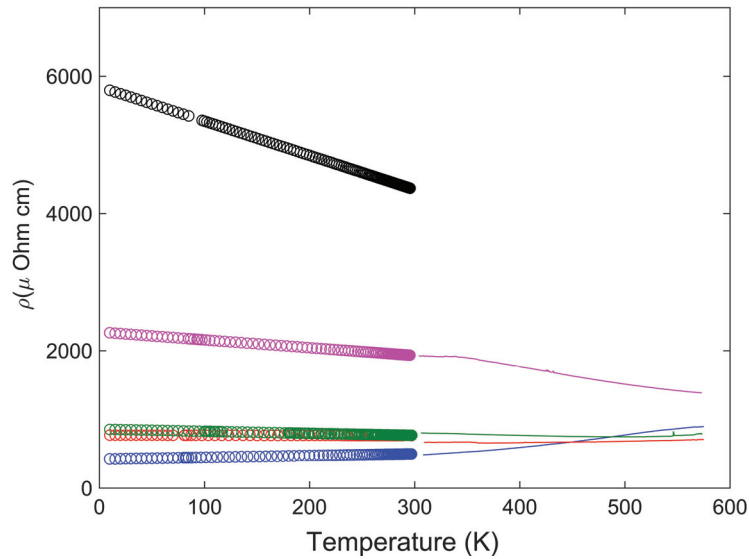


Figure 4.8: Temperature dependence of electrical resistivity as a function of temperature. Low temperature data are reported with circles, high temperature ones with lines. Pure GeTe is reported in blue, GeTeC in red (4%at.), green (9%at.), magenta (16%at. annealed at 723 K) and black (16%at. annealed at 773 K). High temperature data for 16 %at. doping annealed to 723 K are missing.

Fig. 4.10 shows the Seebeck coefficient as a function of temperature between 80 and 300 K for the GeTe sample together with the C-doped samples. All samples exhibit a linear increasing temperature dependence. Our measurements on pure GeTe are in a good agreement with the data provided by Chopra et al in Ref. [143] on 200 nm thick GeTe samples (See Fig 4.10) where the rapid rise of thermopower with increasing temperature has been ascribed to the enhanced scattering of carriers.

The absolute values at room temperature are 77.7 , 61.5 , 72.8 and $72 \pm 7 \mu\text{V/K}$ for pure GeTe and C doped samples with ascending order of C-content, respectively. Hence, we observe only a very small change with carbon doping, which remains below the error bars. This result suggests that C-doping does not significantly affect the Seebeck coefficient leading thus to the same trend observed in GeTe thin films.

In addition to the absolute values and the temperature dependencies, the positive sign of the Seebeck coefficient supports again the classification of all our samples as p-type semiconductors,

4.3.1.2 Discussion

First of all, it should be recalled that the carbon doped samples measured in this section are in fact composites made of core shells structures, as already discussed in section 4.2.2, where the cores are the GeTe grains and the shells are filled by the amorphous carbon. One can wonder thus, whether an effective medium theory (EMT) can describe the variation of the room temperature resistivity upon C-doping.

As a first step, we need to calculate the carbon volume fractions in each sample, starting from the mass densities of the two phases and the known carbon atomic contents X . The GeTe density has been measured by our collaborators at the CEA: $\rho_{\text{GeTe}} = 5.38 \text{ g/cm}^3$. For amorphous carbon, we take an average density from literature $\rho_C = 2.2 \text{ g/cm}^3$ [163]. We can thus calculate the atomic volumes for both components. If we define $R = \frac{\text{atomic volume (C)}}{\text{atomic volume (GeTe)}}$, the carbon volume fractions can be calculated

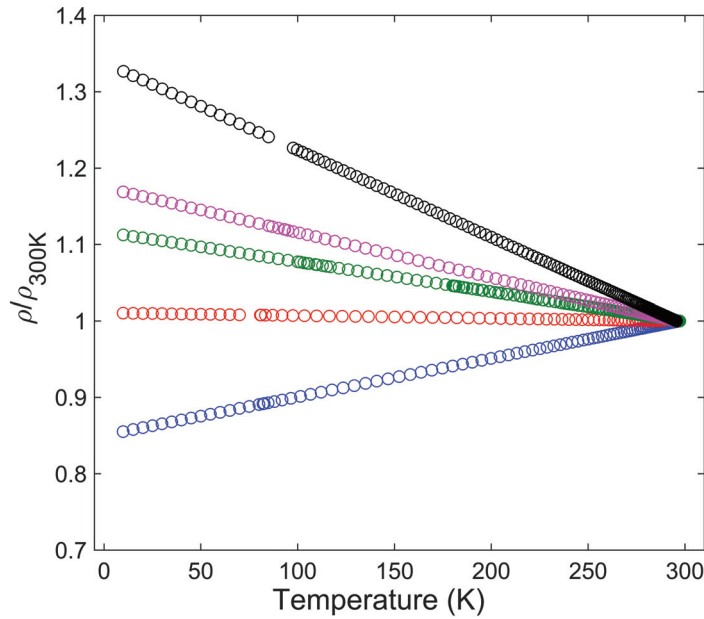


Figure 4.9: Temperature dependence of the low temperature electrical resistivity normalized by the room temperature value, for the crystalline GeTe sample (blue) and GeTe doped samples; with 4 %at. (red), 9 %at. (green), 16 %at. annealed to 773 K (magenta) and with 16 %at. annealed to 723 K (black)

with Eq. 4.3.

$$f = \frac{R.X}{R.X + 1 - X} \quad (4.3)$$

We then obtain $f=1.2, 2.8$ and 5.3% for $X=4, 9$ and 16 %at. The volume fractions are thus very low and below the percolation threshold. We have tried first to fit our data using a model describing a conductive system presenting insulating inclusions given by the following formula:

$$\sigma = \left(1 - \frac{D.f}{d-1}\right) \frac{d}{D} \quad (4.4)$$

Where d is the dimensionality of the system, $d=3$, and D is the fractal dimension (<3). However, this model could not reproduce the peculiar behavior of the resistivity at room temperature and its important increase for $f = 5.3\%$, with physically meaningful parameters. We try thus to fit our data with the generalized EMT presented in Ref. [164] given by:

$$\varphi_1 \frac{\sigma_1^{1/t} - \sigma_e^{1/t}}{\sigma_1^{1/t} - A.\sigma_e^{1/t}} + \varphi_2 \frac{\sigma_2^{1/t} - \sigma_e^{1/t}}{\sigma_2^{1/t} - A.\sigma_e^{1/t}} = 0 \quad (4.5)$$

Where φ_1 and φ_2 are the volume fractions of the phases 1 and 2 respectively, A is a constant that depends on the percolation threshold φ_c (of the phase 2 in the phase 1) through the equation $A = (1 - \varphi_c)/\varphi_c$ and t is a constant representing the asymmetry of the microstructure in terms of connection between the grains. The best fit with the generalized EMT is reported in Fig. 4.11. It can be seen that such model fails in describing our data, suggesting that not only interface scattering plays here a role, differently from the case of metallic glasses, but its role is also dominant. The EMT succeeds actually in predicting the sign change in the temperature derivative of resistivity (TDR) with C-content, still it cannot predict

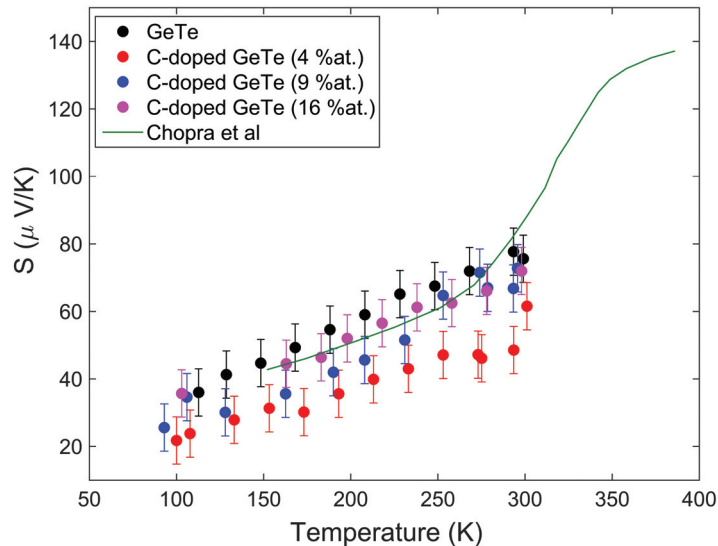


Figure 4.10: Seebeck measurement of crystalline GeTe and GeTeC samples, as a function of temperature, compared with literature data from Chopra [143] on a 200 nm thick pure GeTe film (green solid line).

the high electrical resistivity for our sample with the highest C-content. It is important to underline that the sample reported for this tentative fit is the one annealed at the highest temperature, and thus with the lowest room temperature resistivity and slope. As for the fitting parameters we find for amorphous carbon an electrical resistivity going as $\rho = 5300 - 3.5T$; the shape parameter t results $t=2$ and an unphysical percolation threshold of $\varphi_c=99\%$ is found.

We focus first on the change of the temperature dependence upon C-doping and the fact that it becomes negative.

C-doping causes a crystalline grain size reduction from ~ 160 to ~ 20 nm. One may thus wonder if an enhanced grain border scattering could play a major role in GeTeC. In fact, Siegrist et al [165] reported that the electron mean free path in GeTe is around 29 \AA which is much smaller than the size of the crystallites, thus ruling out any grain boundary scattering effect. Hence, we have to look elsewhere for the explanation of our observations and more likely to possible electronic states localization effects due to disorder. Here, a similar phenomenology (metallic to insulator transition) has been observed in single crystalline GeTe nanowires with pre-induced structural defects. Indeed, under short voltage pulses [166] or ion irradiation [167], dislocations and antiphase boundaries can be created, ultimately leading to carrier localization and to a transition in GeTe from metal to dirty metal first and insulator then. This latter state is achieved when a high degree of disorder is introduced, but still the system retains its single-crystalline long-range order.

In our case, we can speculate that the difficult crystallization process, due to the need of breaking C-Ge bonds and diffusing C atoms to the grain boundaries, causes a bad crystallization, so that crystalline GeTe grains present more defects than when pure GeTe is crystallized. This can explain why even the lowest C-content has already a remarkable effect on electronic properties. Still, such intrinsic defects are likely not enough for inducing the transition from metal-like to insulator-like behavior. This can be likely the result of a localization of charge carriers in the grain boundaries which are now filled by amorphous carbon.

Grain boundaries can be described as potential barriers that the carriers need to overcome. It has been recently shown that, if a random distribution of such barriers is assumed in granular semiconductors,

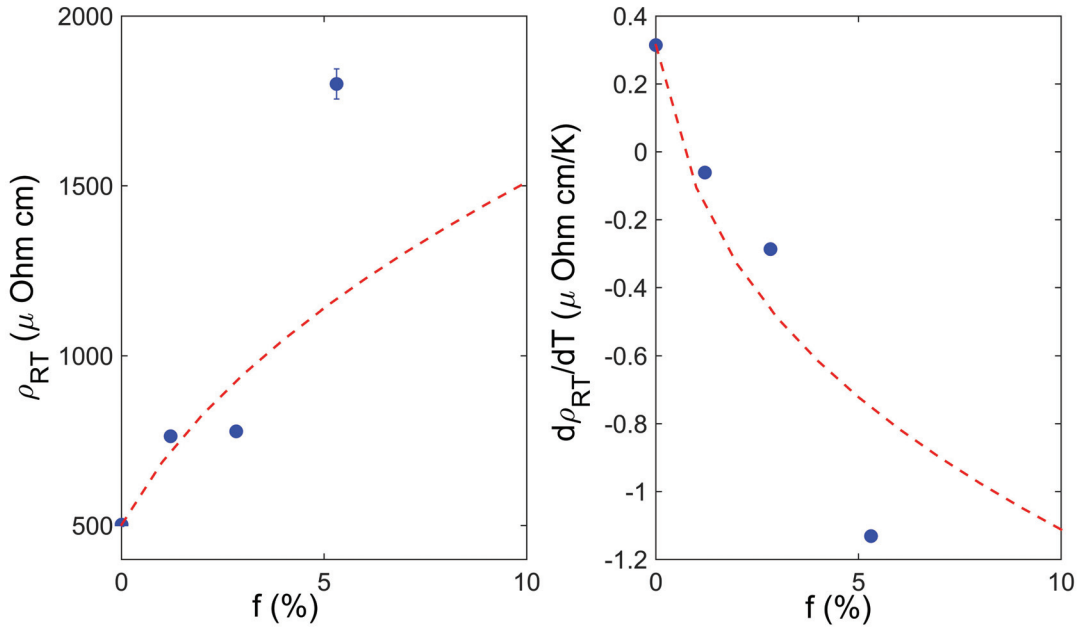


Figure 4.11: Left: room temperature electrical resistivity and TDR (right) as a function of carbon fraction (f).

energy filtering and carrier localization can take place [168].

On the other hand, the Seebeck coefficient does not exhibit much change with the carbon doping, which means that the localization of electronic states does not have any effect on the Seebeck.

In the framework of the Boltzmann transport equation, the Seebeck coefficient can be written as [168]:

$$S = \frac{1}{qT} \cdot \frac{\int_0^\infty E\tau(E)(E - E_f)g(E)\partial_E f_0 dE}{\int_0^\infty E\tau(E)(E)g(E)\partial_E f_0 dE} \quad (4.6)$$

Where $g(E)$ is the density of electronic states, $f_0(E)$ is the Fermi-Dirac distribution function, q is the carrier charge, $\tau(E)$ is the energy dependent carrier relaxation time, E_f is the Fermi energy and T is the absolute temperature.

The localization would affect the relaxation time τ , which however appears both at numerator and denominator in Eq. 4.6. If despite the localization, $\tau(E)$ keeps a fairly weak energy dependence, the modified $\tau(E)$ can be extracted from the integral in both numerator and denominator and will cancel out, thus leading to a lack of strong effect on the Seebeck coefficient. This picture is compatible as well with the findings of Ref. [168], where it is reported that the effect on the Seebeck coefficient strongly depends on the nature of grain boundaries and potential barriers distribution.

In the cited work, it was reported that the Seebeck coefficient should depend on the ratio between electrical conductivity and localized carriers fraction χ : $S = E_f - B\left(\frac{\sigma}{\chi}\right)^{2/5}$ where E_f is the Fermi energy, σ is the electrical conductivity and B is a parameter depending on material electronic properties. The independence of the Seebeck coefficient on the carrier localization implies that the electrical conductivity is proportional to the amount of localized carriers χ .

Assuming this proportionality, and reminding that the EMT does not work here, we deduce that such amount is not simply proportional to the carbon volume fraction. A more complex connection must exist, related to the exact nature and geometry of the grain boundaries. Indeed, the localized carrier concentration depends on the threshold mobility, which in turn depends on the potential barrier width

on one hand, e.g. the thickness of grain boundaries, and its height on the other, e.g. the atomic bonds at play. In order to get more insight on the relation between localized carriers and carbon content, further investigations, such as Hall mobility measurements, would be needed, which however remain beyond the scope of this work.

In the framework of a localization-dominated electron transport in GeTeC, the change in the slope and absolute value of the resistivity with annealing can be explained as due to a partial removal of localization and disorder with temperature. Indeed, it is largely known that TDR increases with decreasing defect density [169, 170]. We can thus understand the observed phenomenology as due to a temperature induced structural defects annihilation within the crystalline grains.

4.3.2 Thermoelectric potential of GeTeC nanocomposites

All sets of experimental data provided in this section have been combined to calculate the power factor $P = \frac{S^2}{\rho}$ which is represented in Fig. 4.12. All alloys display a rising trend in P over the entire temperature range comprised between 80 and 300 K used in Seebeck measurements. Crystalline GeTe exhibits the highest power factor pointing to $P=0.35\pm 0.06$ W/mK at 300 K. As for the C-doped samples, it is clear that high C-content such as 16 %at. ultimately leads to very low power factors, due to the increased electrical resistivity.

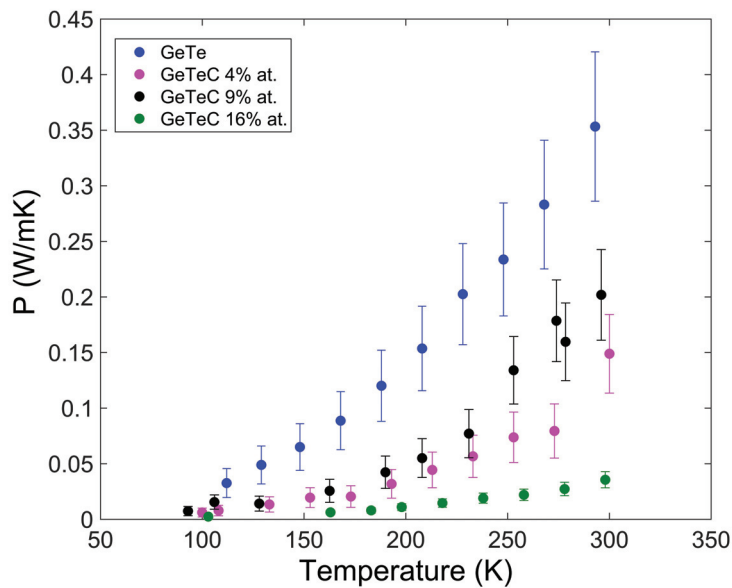


Figure 4.12: Power factor $P = \frac{S^2}{\rho}$ measured for crystalline GeTe and GeTeC samples. Here we have reported only the sample at 16% at. content annealed at 723 K.

We calculate now the ZT using the thermal conductivity values provided in Ref. [140]. As shown in Fig. 4.13, only small values of ZT were obtained for crystalline GeTe with a maximum value of 0.25 ± 0.14 at 300 K. For the C-doped samples, higher thermoelectric efficiencies are observed with a maximum value of ≈ 0.9 at 300 K in the samples doped with 4 and 9% at. As expected, the sample doped with 16% at. displays the lowest ZT. However, this value can be enhanced to 0.95 by further annealing the sample to 773 K, assuming that the annealing will not affect the Seebeck coefficient. Moreover, as

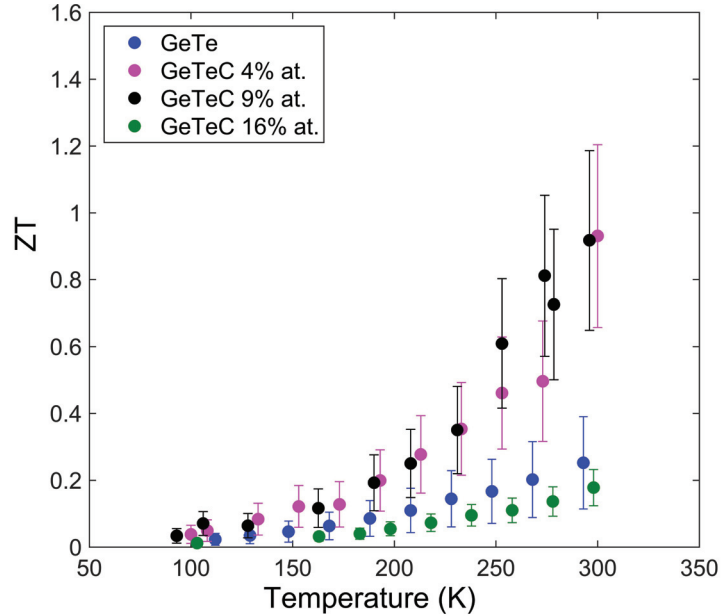


Figure 4.13: Thermoelectric figure of merit $ZT = \frac{P}{k_T}$ calculated from the experimental data for the crystalline GeTe and GeTeC samples. Here we have reported only the sample at 16% at. content annealed at 723 K.

all alloys display a rising trend in ZT over the entire measured temperature range, we may expect to reach even better thermoelectric efficiencies at temperatures above 300 K.

GeTeC composites appear then as very promising for thermoelectric applications. Still such promise relies on the exceptionally low thermal conductivity of the C-doped crystalline phases.

We can use our electric measurements in order to obtain an indirect confirmation of Kusiak's thermal conductivity data, by calculating the electronic contribution. This can be done using the Wiedeman-Franz law $k_{el} = \frac{LT}{\rho}$, and calculating L with the model proposed by Kim et al [171] based on the measured Seebeck coefficient S : $L = 1.5 + \exp(-\frac{|S|}{116})$. We then find for crystalline GeTe $k_{el}=1.2$ W $K^{-1}m^{-1}$ and for crystalline GeTeC $k_{el}=0.81, 0.95$ and 0.14 W $K^{-1}m^{-1}$ for 4, 9 and 16%at. (annealed at 723 K) respectively. With the exception of the highest C-content, the electronic contribution in GeTeC is surprisingly much larger than the total thermal conductivity reported by Kusiak et al [140] ($k_T = 0.2 \pm 0.02$ W $K^{-1}m^{-1}$), shedding a doubt on the reliability of their measurements. An experimental verification of the values reported by Kusiak is thus mandatory for definitely assessing the potential of these composites for thermoelectricity.

4.4 Effect of a partial crystallization

In the spirit of increasing the amorphous fraction in the GeTeC composites, rather than further increasing the C-content, we have investigated partially crystallized samples. This section deals thus with composites made of core-shells nanoparticles (crystalline GeTe grains surrounded by amorphous carbon) embedded in a GeTeC amorphous matrix. In the first paragraph, we investigate the electrical properties of partially crystalline GeTeC with 16 %at. C-content, chosen for its higher insulator behavior. In the second paragraph, we address the thermal properties of our composites by a microscopic point of view. As previously said, the thermoelectric potential of these materials resides in their reported low thermal

conductivity. Since there are not any other macroscopic data to confirm it, we use x-ray inelastic scattering for investigating the phonons velocity and lifetime properties and getting a microscopic insight into the thermal transport properties. For this study GeTeC with 9 %at. C-content has been selected as the alloy with the best thermoelectric potential.

4.4.1 Electrical properties

We present here the investigation of the effect of a partial crystallization on the low temperature electrical resistivity of GeTeC with 16 %at. C-content. Two samples, with 40 % and 60 % crystalline content, have been measured between 10 and 300 K. Lower crystalline fractions resulted in highly insulator samples, beyond the technical capability of our equipment. The temperature and crystalline fraction dependencies are presented in Fig. 4.14. The room temperature resistivity decreases with the crystalline fraction (Fig. 4.15), as expected.

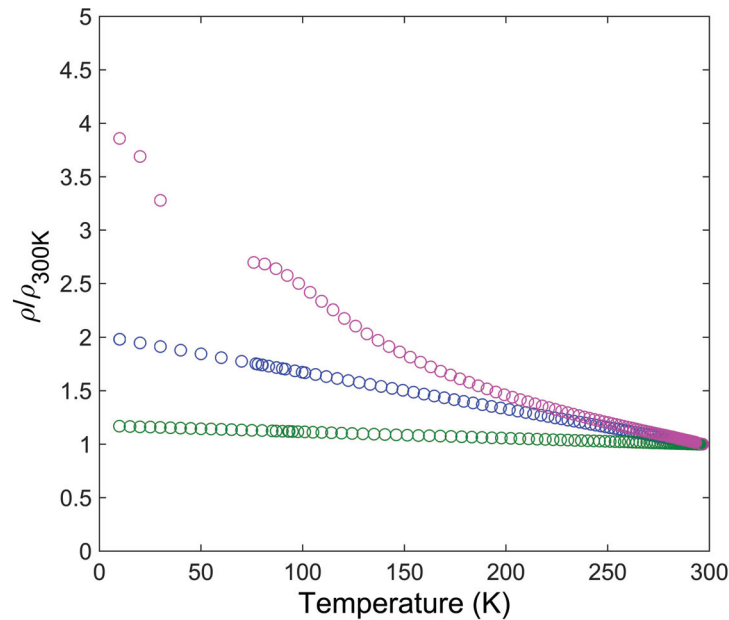


Figure 4.14: Temperature dependence of electrical resistivity normalized by the room temperature value for of GeTeC samples (16% at. of C-content) with crystalline fractions $x=40\%$ (magenta), $x=60\%$ (blue) and $x=100\%$ annealed at 773 K (green).

The temperature dependence is illustrated in Fig. 4.15 where we report the Temperature Coefficient of Resistivity $TCR = \frac{1}{\rho_0} \left(\frac{\partial \rho}{\partial T} \right)$ as a function of crystalline fraction, where ρ_0 is the residual resistivity and the quantity $\frac{\partial \rho}{\partial T}$ is obtained by fitting the data for $150 < T < 300$ K. Both measured composite samples display a negative TCR, together with the fully crystallized sample, arising from the same insulator-like behavior observed in the fully crystallized sample. Despite the negative sign, we can still observe an increase of the TCR with increasing the crystalline fraction. This seems quite obvious, since the disorder decreases with the crystallization.

In addition to electrical resistivity measurements, we have also looked into the effect of the partial crystallization on Seebeck coefficient. Fig. 4.16 shows the temperature dependence of a composite sample with a total crystalline fraction $x = 60\%$ compared to the fully crystallized one. Surprisingly, no

effect has been observed: absolute value as well as temperature dependence are completely unaffected by the partial amorphization of the sample. At this stage, we don't have any explanation for this result. More data on samples with different crystalline fractions are needed.

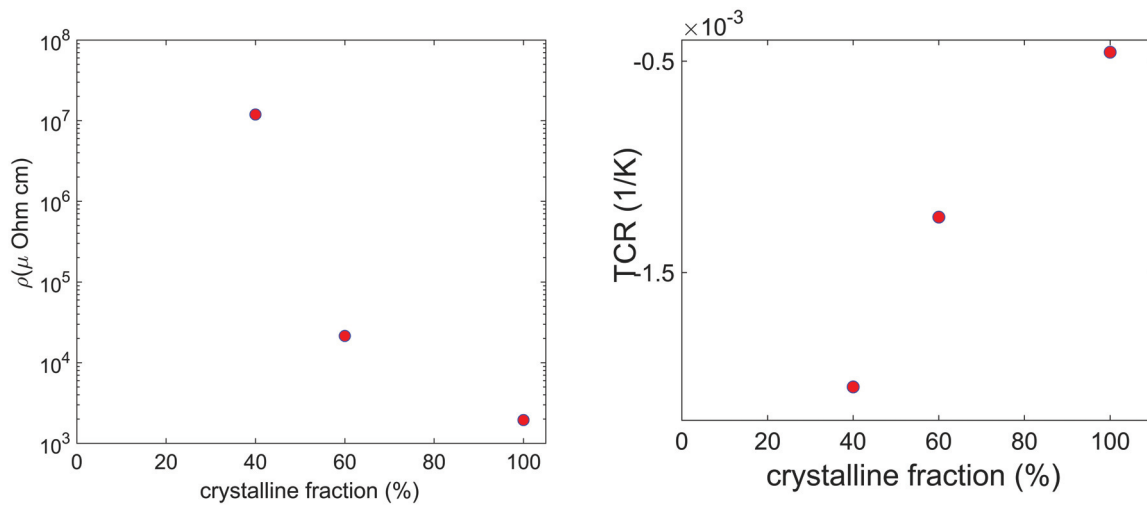


Figure 4.15: Left: Room temperature electrical resistivity of partially crystallized GeTeC as a function of the crystalline fraction. Right: Temperature coefficient of resistivity (TCR) in GeTeC with 16% of C content, as a function of the crystalline fraction. Here the fully crystallized sample is annealed at 773 K.

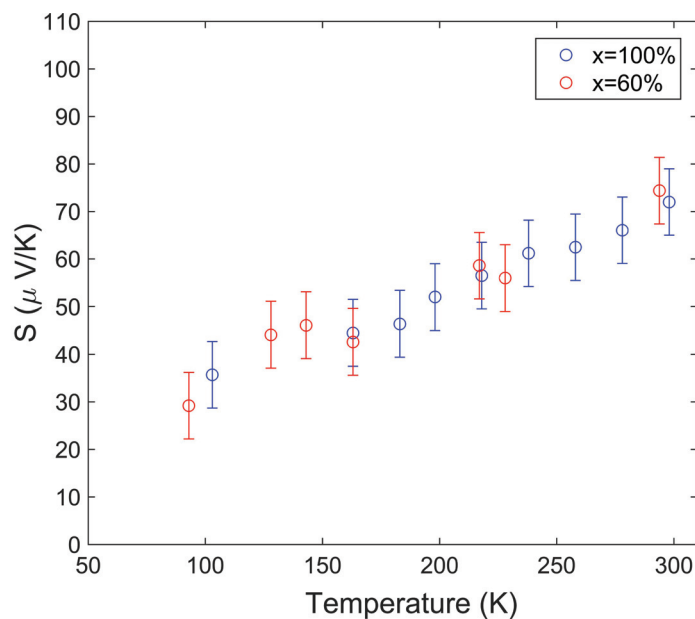


Figure 4.16: Temperature dependence of Seebeck coefficient in a 60% crystallized GeTeC sample with 16%at. C-content compared to a fully crystallized sample annealed at 723 K

4.4.2 Phonons transport

In order to have a better understanding of the underlying lattice dynamics responsible for the low thermal conductivity in crystalline GeTeC, it is necessary to learn more about the phonon dynamics in such material.

We focus now on the phonon contribution in GeTeC with 9%at. of C-content. To this aim we performed IXS measurements at ID28 at ESRF to measure phonons in two samples: a fully crystallized sample and a partially crystallized one with $x = 30\%$. The fully amorphous sample could not be measured due to an extremely intense elastic line hiding all inelastic features. Data were collected in grazing incidence geometry mounting the sample vertically and slightly tilted. The X ray energy was 17.8 keV, giving an energy resolution of 3 meV. Three q points below 4 nm^{-1} could be measured as well using an X ray incident energy of 23.7 keV with an energy resolution of 1.4 meV. The incident grazing angle was chosen in order to reduce the silicon substrate contribution to the IXS signal. Then, data have been analyzed using a DHO model for the inelastic excitation and a delta function for the elastic line, convoluted with the experimental resolution.

We focus first on the fully crystallized sample. A selection of the obtained spectra is reported in Fig. 4.17, for positive energy transfer and after subtraction of the elastic line. Despite the noisy signals, we can still observe well defined modes. Two inelastic excitations were needed for $q \geq 7 \text{ nm}^{-1}$ where the highest energy modes are ascribed to optic modes.

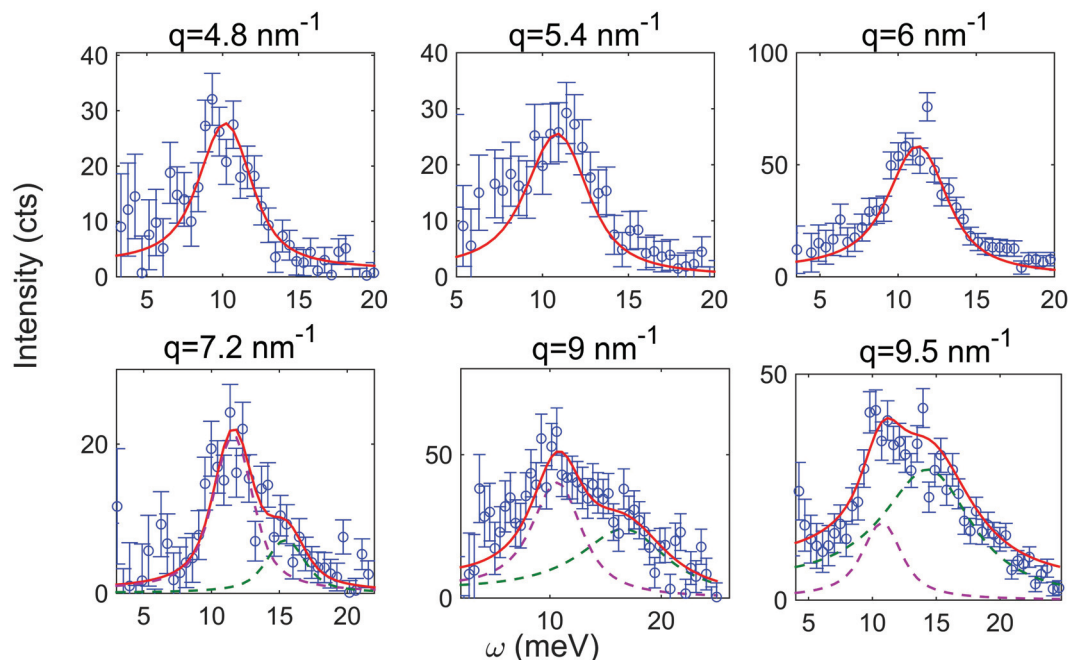


Figure 4.17: Inelastic X ray spectra in a fully crystallized GeTeC sample with 9%at. C-content. The result of the fit with a DHO model is reported as well as a red line. In the bottom line two excitations have been used for modeling the data, and are reported as dashed lines.

Fig. 4.18 shows the experimental phonon dispersions of the fully crystallized GeTeC sample, compared with unpublished DFT calculations performed by J.-Y. Raty on a pure GeTe crystalline sample [172]. Only longitudinal acoustic modes are reported from theory.

We have marked in blue the experimental modes that we interpret as longitudinal, and in green and red the optic modes. The lowest q-points, reported as squares, correspond to measurements performed at 23.7 KeV with a 1.4 meV resolution.

It can be seen that our longitudinal dispersion lies well in between the calculated longitudinal branches, as it would be expected for a polycrystal dispersion. Indeed, in a polycrystal the observed longitudinal dispersion is the orientational average of all directions in the single crystal. Starting from $q=8.4 \text{ \AA}^{-1}$, we start to see other modes, dubbed optic. More specifically, the longitudinal dispersion is stopped by

the low-lying optic mode at ~ 12 meV, here reported in green.

The agreement between our experimental data and the DFT calculations indicates that C-doping does not affect the sound velocity, and in general the vibrational properties, of pure GeTe. This result is in agreement with our findings on low-frequency optic modes as measured by Raman spectroscopy, and ultimately is consistent with the picture of a composite made of crystalline GeTe nanograins with unmodified elastic constants, with an amorphous carbon shell,

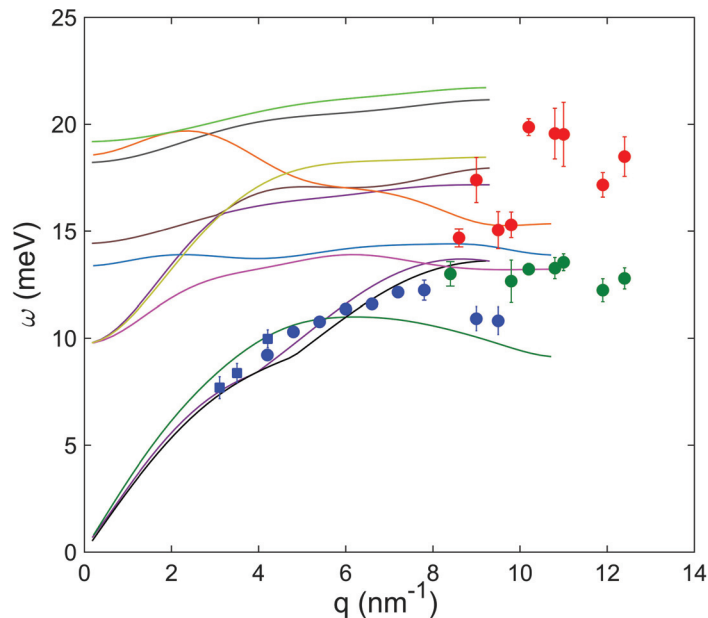


Figure 4.18: Longitudinal acoustic and optic phonon dispersion of a fully crystallized GeTeC sample with 9%at. C-content. Data are reported as symbols, with the following color code: blue for longitudinal acoustic modes, green for the low-lying optic mode, red for higher energy optic modes. Blue squares correspond to high resolution data collected with an incident energy of 23.7 keV, bullets to data collected with an incident energy of 17.8 keV. Phonon branches calculated by DFT on a single crystalline pure GeTe sample are reported for comparison (lines, J.Y. Raty [172]).

As said, in polycrystalline materials, we measure a phonon dispersion which is the result of an orientational average of the phonon branches over all directions. In absence of external sources of a dramatic phonon damping, the experimental phonon broadening corresponds then to the width of the branches distribution.

In Fig. 4.19 we report the acoustic longitudinal phonons below $q=8.4$ nm^{-1} , compared again with calculations. In this case, however, we report as errorbars the experimental phonon broadening. It can be seen that, starting from $q=4$ nm^{-1} and up to $q\sim 8$ nm^{-1} the phonon width is well compatible with the longitudinal branches separation calculated by DFT. For $q>8$ nm^{-1} a large phonon broadening sets in, due to the coming in of many optic modes, that we cannot experimentally resolve. Such observation would indicate that we are not measuring an intrinsic longitudinal phonon lifetime for $q>4$ nm^{-1} .

To get more insight on the longitudinal phonon lifetime, the longitudinal phonon broadening given by the energy width at each wave vector q , is plotted in Fig. 4.20. As we have previously mentioned, the IXS signal is given by the dynamic structure factor, convoluted with the experimental resolution of the spectrometer. Analytically, during a fit, we convolute a theoretical model with the experimental energy resolution. In such convolution/deconvolution procedure we can reliably extract from our data

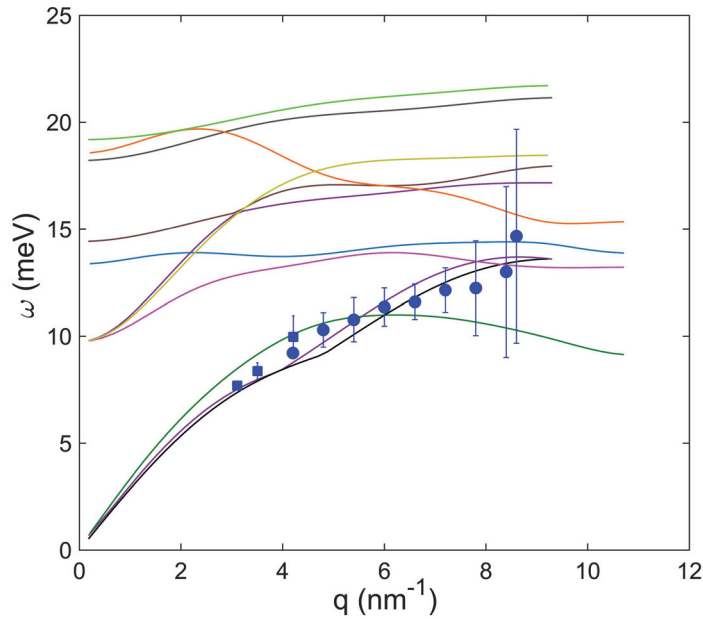


Figure 4.19: Longitudinal acoustic and optic phonon dispersion of a fully crystallized GeTeC sample with 9%at. C-content. Data are reported as symbols, with the following color code: blue for longitudinal acoustic modes, green for the low-lying optic mode, red for higher energy optic modes. Blue squares correspond to high resolution data collected with an incident energy of 23.7 keV, bullets to data collected with an incident energy of 17.8 keV. The errorbars are here reported as equal to the experimental phonon broadening. Phonon branches calculated by DFT on a single crystalline pure GeTe sample are reported for comparison (lines, J.Y. Raty [172]).

only intrinsic phonon lifetimes larger than $\sim \Gamma_{min} = \frac{E_{res}}{5}$. This defines then a lower experimentally accessible broadening Γ_{min} . On the other hand, the q resolution plays a role as well. Due to the finite size of the horizontal slit in front of the analyzers, we do not measure a single point q in the phase space, but a small q -range. In our experimental setup we measure $\Delta q \sim 0.34 \text{ nm}^{-1}$. Such q -spread converts into an energy-spread, due to the local slope of the acoustic dispersion, as each q within this range will correspond to a phonon with different energy. It results then that an additional experimental q -related energy resolution arises given by $\Delta E_q = \frac{\partial E}{\partial q} \cdot \Delta q$. We report in Fig. 4.20 Γ_{min} calculated for an incident energy of 23.7 KeV (green) and 17.8 KeV (purple), and the calculated ΔE_q as a dashed line. It can be seen that the lowest q -value measured at 17.8 KeV (red data) is below the minimum accessible broadening, and thus its numerical value is not meaningful. The same is true for the lowest q value measured at 23.7 KeV (blue data). The $q=3.4 \text{ nm}^{-1}$ value measured at 23.7 KeV corresponds in fact to the q -related energy resolution. Thus only broadenings measured for $q > 4 \text{ nm}^{-1}$ are beyond the experimental resolution. Still, as observed from Fig. 4.18, at such values the measured width corresponds to the branches separation. We can therefore conclude that in this sample we are unable to access intrinsic phonon lifetimes, for any explored q .

Concerning the partially crystallized sample, we could obtain only 3 scans due to the bad quality of signal and the high elastic line. We report them in Fig. 4.21, after subtraction of the elastic line. We have chosen to fit the data with only one excitation: indeed, when the optic mode is visible (for example at $q=6.6 \text{ nm}^{-1}$), it is weak and well distinct from the acoustic mode, so that neglecting it does not change significantly the fitting results on the acoustic energy and width.

It can be seen from Fig. 4.22 and 4.23 that the partially crystalline sample exhibits a lower speed of

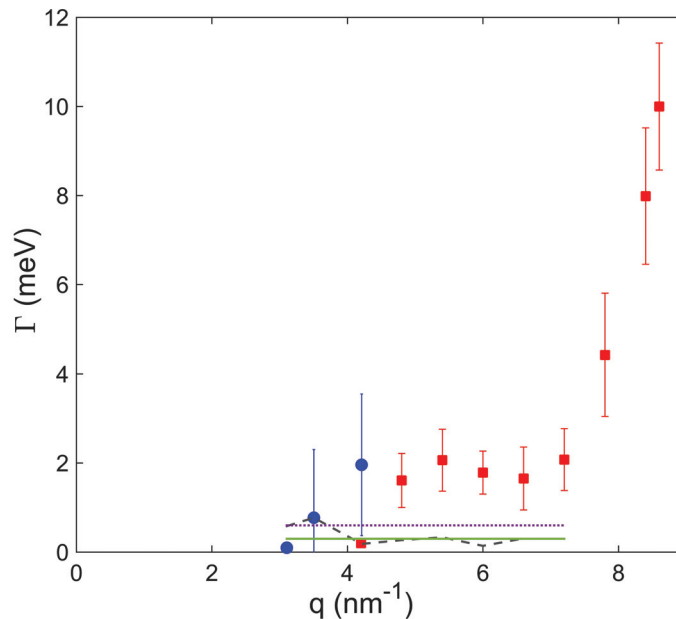


Figure 4.20: Longitudinal phonon broadening of a fully crystallized GeTeC sample with 9%at. C-content. of a fully crystallized GeTeC sample with 9%at. C-content. Blue bullets correspond to high resolution data collected with an incident energy of 23.7 keV, red squares to data collected with an incident energy of 17.8 keV. The green and purple lines correspond to Γ_{min} , calculated for an incident energy of 23.7 meV and 17.8 meV, respectively, and the black line corresponds to the calculated experimental resolution ΔE_q .

sound, and a much stronger acoustic phonon damping. From our data, we see that in the partially crystalline sample we do measure an intrinsic phonon broadening, going well beyond the phonon branches separation of the fully crystalline sample, likely due to the important amorphous component.

Such contrast between composite and polycrystal, very different from what we have observed in the metallic glass case, likely reflects an even stronger contrast of properties between amorphous and polycrystal. Indeed, as we don't have data on the amorphous sample, we can only infer from these results that in the glass the speed of sound would likely be even lower and phonon broadening even larger.

Moreover, our results shed another strong doubt on the thermal conductivity data by Kusiak on the fully crystalline sample, concerning the vibrational contribution. We have seen that already the electronic contribution as calculated using the Wiedemann-Franz law and our measured electric resistivities exceed the thermal conductivity reported by Kusiak. One could argue that the validity of the Wiedemann-Franz law is at this day still a matter of debate. However, when one looks at our vibrational results, it can be seen that even disregarding the electronic contribution, our results are in contradiction with Kusiak's data.

The first thing to notice is that in the amorphous sample the total thermal conductivity is fully vibrational, the glass being insulator, and equal to $0.2 \text{ W K}^{-1}\text{m}^{-1}$. As Kusiak has reported the same total thermal conductivity in the crystal, where normally the electronic contribution should not be absent, the vibrational contribution in the crystal should be even smaller than in the glass. This could eventually happen for a smaller phonon lifetime or a reduced acoustic phonon phase space in the crystal than in the glass.

We have already seen that GeTeC has the same acoustic dispersion as GeTe, which means that there is no reduction of the phonon phase space useful for heat transport with carbon doping. The speed of sound of the fully crystalline sample is moreover about 20% higher than in the composite, and thus in

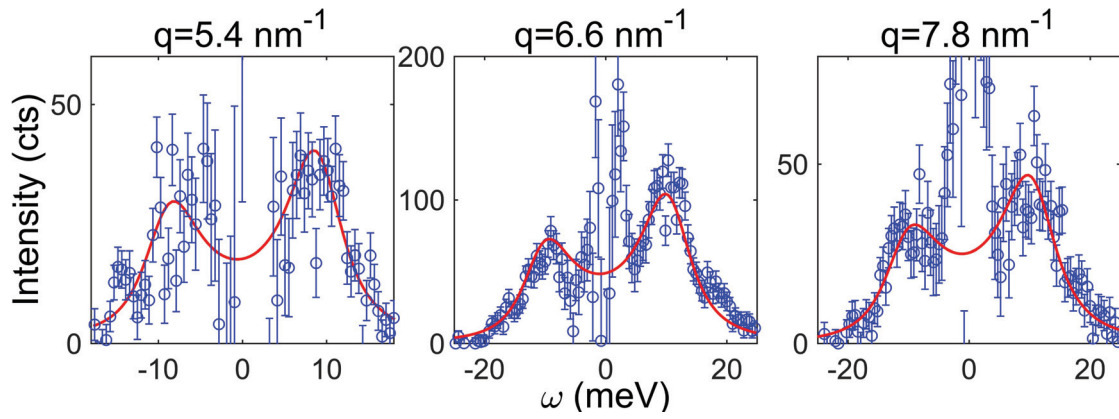


Figure 4.21: Inelastic X ray spectra, for 3 different q -points, are reported after subtraction of the elastic line for the 30% crystallized sample. The result of the fit with a DHO model is reported as well as a red line.

the glass. It does remain thus only a short phonon lifetime as explanation for a low thermal conductivity in crystalline GeTeC. More specifically, as the speed of sound is higher in crystalline than amorphous GeTeC, phonon lifetime should be quite smaller in the former than in the latter in order to explain a similar vibrational thermal conductivity.

In the fully crystalline sample we are not able to measure the intrinsic lifetime, as we in fact measure only the experimental resolution at low q and the inter-branches separation at high q . We can only set the experimental resolution broadening as an upper limit to the intrinsic phonon broadening in the polycrystal, $\Gamma_{min}=0.3$ meV for $q<4\text{nm}^{-1}$ and $\Gamma_{min}=2$ meV for larger q , as limited by the phonon branches separation.

On the other side, the phonon broadening in the composite can be taken as a lower limit for the one in a fully amorphous sample, e.g. $\Gamma^{am} \geq 8$ meV for $q>5$ nm^{-1} . Taking the phonon at 5.4 nm^{-1} as representative, the fully crystalline sample thus presents an acoustic phonon lifetime which is more than 4 times the one in the amorphous phase, resulting then in a thermal conductivity which, in a simple kinetic formulation, should be about 6 times the one of the glass, taking into account the velocity increase with crystallization. Our results thus strongly contradict Kusiak's data, and challenge the interest of such materials for thermoelectricity.

Finally, we can comment on the effect of the partial crystallization on phonon dynamics. A partial amorphisation induces an elastic moduli softening, as seen from the sound velocity decrease, and lifetime reduction. Such behavior is different from the case of the metallic glass composite, where the same crystalline fraction was leading to the same elastic moduli as in the polycrystal, and similar phonon broadening.

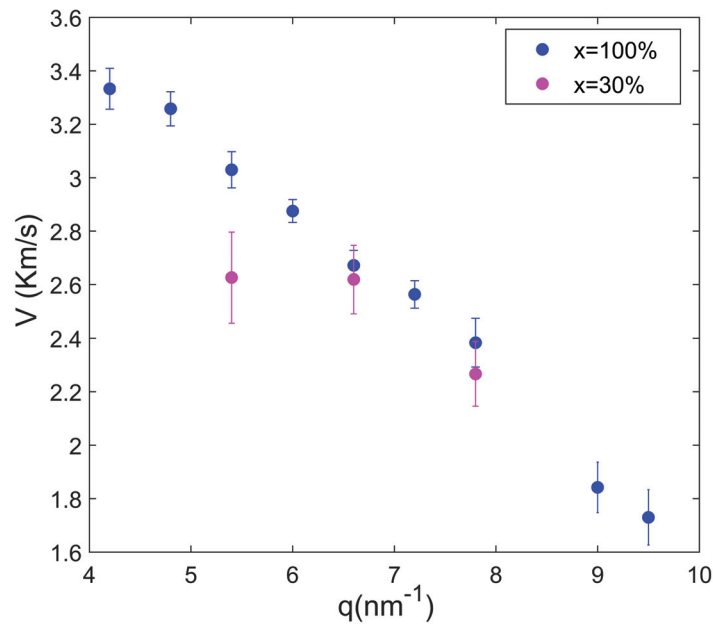


Figure 4.22: Longitudinal velocity of sound as a function of the wavevector q for the fully crystalline sample and the partially crystallized one

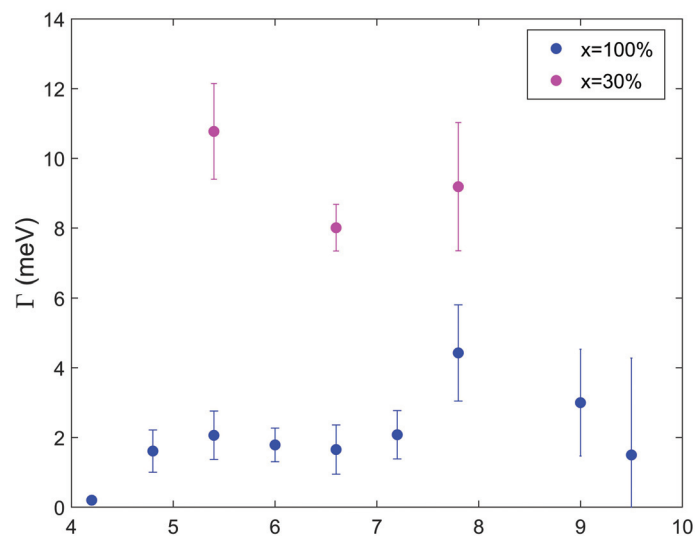


Figure 4.23: Longitudinal phonon broadening as a function of wavevector q for the fully crystalline sample and the partially crystallized one

4.5 Conclusion

In this chapter, we have presented an experimental study of the transport properties of carbon-doped GeTe. Two types of amorphous/crystalline composites have been considered. The first one is formed by direct crystallization of glassy GeTeC. The so-obtained composite is in fact a polycrystal of core-shell particles, composed of crystalline GeTe nanograins with amorphous carbon shells. The second composite is obtained by partial crystallization of glassy GeTeC, thus resulting in core-shell nanograins embedded in an amorphous GeTeC matrix.

In the former composite, C-doping has been shown to induce metallic-like to insulator-like transition in the electronic transport properties, which has been explained as due to a charge localization at amorphous grain boundaries. No strong effect is observed on the Seebeck coefficient, consistent with a picture where the effect on Seebeck coefficient strongly depends on the geometry and energy details of the energy barriers at the grain boundaries. Interestingly, once the electronic contribution to the total thermal conductivity is calculated, a strong disagreement with the ultra-low thermal conductivity reported by Kusiak for crystalline GeTeC samples is observed, shedding a doubt on the reliability of literature reports.

We have reported as well an electronic and vibrational characterization of partially crystallized GeTeC. Once again the Seebeck coefficient is not affected while the electric resistivity displays a more and more insulating behavior as the amorphous component increases.

Concerning vibrational properties, we find that the behavior is remarkably different from the one of the metallic glass composite. In the case of GeTeC, the vibrational dynamics of the 30% composite is dominated by the amorphous component, displaying a decrease of the sound velocity and strong phonon attenuation.

Unable to measure the intrinsic phonon lifetime in crystalline GeTeC, we have used the experimental data for setting a lower limit for it. Such value has been compared with the phonon lifetime as measured in the composite, which represents an upper limit for the amorphous phase. The comparison clearly points to a vibrational contribution to the thermal conductivity which is in the crystal at least 4 times larger than in the glass, thus challenging once more the findings of Kusiak.

To summarize, we have here investigated a system which does present a strong contrast of electronic and acoustic properties. Such contrast translates into the arising of charge localization effects at grain boundaries, and in a different vibrational behavior with a partial crystallization with respect to the metallic glass composite. Indeed the vibrational dynamics is now dominated by the amorphous component for the same crystalline fraction at which in the metallic glass it was crystal-dominated.

Chapter 5

Thermal transport in amorphous/crystalline composites: numerical simulations

In the previous two chapters, we have presented an experimental investigation of the transport properties in amorphous/crystalline composites where we emphasized the importance of contrast of properties between the crystalline inclusion and the amorphous matrix. In the present chapter we provide simulations of the vibrational properties performed by means of molecular dynamics. We focus particularly on investigating the effect of rigidity contrast between the inclusion and the amorphous matrix. In the Stillinger-Weber potential introduced in Chapter 2, the parameter λ allows to tune the three-body term, finally changing the system's rigidity. In Ref. [173] it can be seen that all elastic moduli depend linearly on λ . In this work the amorphous matrix is always described by a potential with $\lambda = 21$, while for the inclusion we have used once $\lambda = 21$ and once $\lambda = 100$. A linear extrapolation of the elastic moduli as a function of λ from Ref. [173] allows to estimate the expected change in the Young (E), the bulk (B) and the shear (G) moduli. Specifically, it results $E(\lambda = 100) = 4.6E(\lambda = 21)$, from which we can define the rigidity contrast between inclusion and matrix as $\chi = \frac{E(\text{inclusion})}{E(\text{matrix})}$. Therefore, in the first composite we have $\chi = 1$ and in the second $\chi = 4.6$.

In the first part of this chapter, we report calculations of the vibrational density of states in an amorphous sample and in the two composites with different χ . The section 5.2 reports a detailed analysis of the dynamical structure factor providing insights on the sound velocity and the phonon lifetime. The effect of rigidity contrast on the phonon mean free path is presented in section 5.3 by following the propagation of a wave-packet at a given frequency. Finally in section 5.4, calculations of the total thermal conductivity are provided.

5.1 Density of Vibrational States

The diagonalization of the dynamical matrix allows one to access the eigenmodes and the eigenfrequencies of the system. The vibrational density of states (VDOS) can thus be obtained.

We have then calculated the vibrational density of states for three samples, one fully amorphous and two composites with a different rigidity contrast, by summing the number of eigenmodes existing for each frequency interval $\delta\omega = 0.1 \text{ THz}$. This kind of calculations being heavily time-demanding, we have kept the sample size reasonably small. In all cases we used a sample box with side of 30 \AA . The inclusion is spherical with radius 10 \AA , which gives a crystalline volume fraction of 15%.

Examples of such eigenmodes can be seen in Fig. 5.1 for five distinct frequencies for the three samples. The direction of each arrow represents the displacement direction of the corresponding particle and the size of the arrow represents the amplitude of this displacement. At low frequencies ($<1.8 \text{ THz}$), we can observe propagating waves in the amorphous sample. For the two composite samples, the propagating character is still visible and the particles belonging to both the crystalline and the amorphous part are now moving together and become faster for the sample with $\chi = 4.6$, due to the higher velocity of sound inside the crystalline inclusion. At higher frequency ($<6.2 \text{ THz}$), we don't see any remarkable difference among the three samples. Modes become more and more localized, for the highest frequency ($\sim 17.84 \text{ THz}$). Interestingly, while the spacial modes localization in the amorphous phase is random, in the composite, modes appear to be localized around the inclusion, as it can be easily seen in the composite with $\chi = 4.6$.

The corresponding VDOS have been calculated around equilibrium at $T=0 \text{ K}$ and are reported in Fig. 5.2. First of all, we notice that the VDOS starts at $\omega = 1 \text{ THz}$, being zero for lower frequencies. This is in fact an artifact due to the limited size of our sample box. Indeed, the box side L imposes a lower limit for the wave-vector and thus frequency that can be explored, $q_{min} = \pi/L$. Here it is $q_{min} = 0.1 \text{ \AA}^{-1}$ which corresponds to $\omega_{min} \simeq 1 \text{ THz}$. Looking now to the three samples, it can be seen that the DOS

of the composite where there is no rigidity contrast between inclusion and matrix is basically indistinguishable from the DOS of the fully amorphous sample. Weak differences can be seen at high frequency ($\omega > 10$ THz), which seem to correspond to a shift of modes from the 16 THz peak.

The composite with a rigidity contrast $\chi = 4.6$ shows stronger differences. Already in the acoustic part of the DOS where both transverse and longitudinal modes are present ($\omega < 5$ THz) we can see that the slope of the DOS is smaller, which comes from a higher speed of sound. Moreover, the redistribution of modes which were first localized in the 16 THz peak in the amorphous is now clearer: a density increase can be in fact seen not only in the 10-14 THz region but also at high frequency, up to 25 THz.

The presence of the inclusion implies then a weak increase of the optic modes in the 10-14 THz for both composites and for the composite with $\chi = 4.6$ the appearance of modes above 20 THz. Such high frequency modes can be understood when one considers that the normal modes of the inclusion will shift to higher frequency with the stiffening of the elastic constants. One could expect that phonons with a wave-length comparable to the inclusion size would be more affected by its presence. In our case this corresponds to a $q = 0.3 \text{ \AA}^{-1}$, which, as we will see in the next section, corresponds to energies between 1 THz (transverse) and 3 THz (longitudinal). We don't see any special modification of the DOS in this energy range. However, such energies remain at the limits of our calculations because of the limited box size. We cannot therefore rule out an effect of the inclusion on these phonons. The lack of differences in the acoustic part of the DOS for $\chi = 1$ suggests that the thermal conductivity would not show a clear change unless the phonon mean free path is strongly affected by the presence of the inclusion.

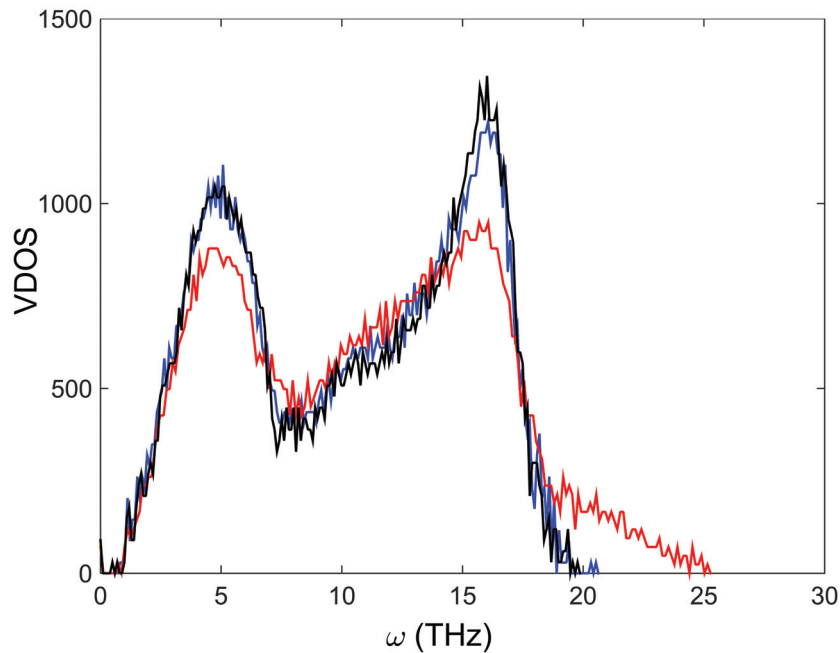


Figure 5.2: Vibrational density of states (VDOS) calculated for three samples, one fully amorphous (black) and two composites (volume crystalline fraction of 15 %) with a different rigidity contrast between the amorphous matrix and the crystalline inclusion corresponding to $\chi = 1$ (blue) and $\chi = 4.6$ (red). More details can be found in the text.

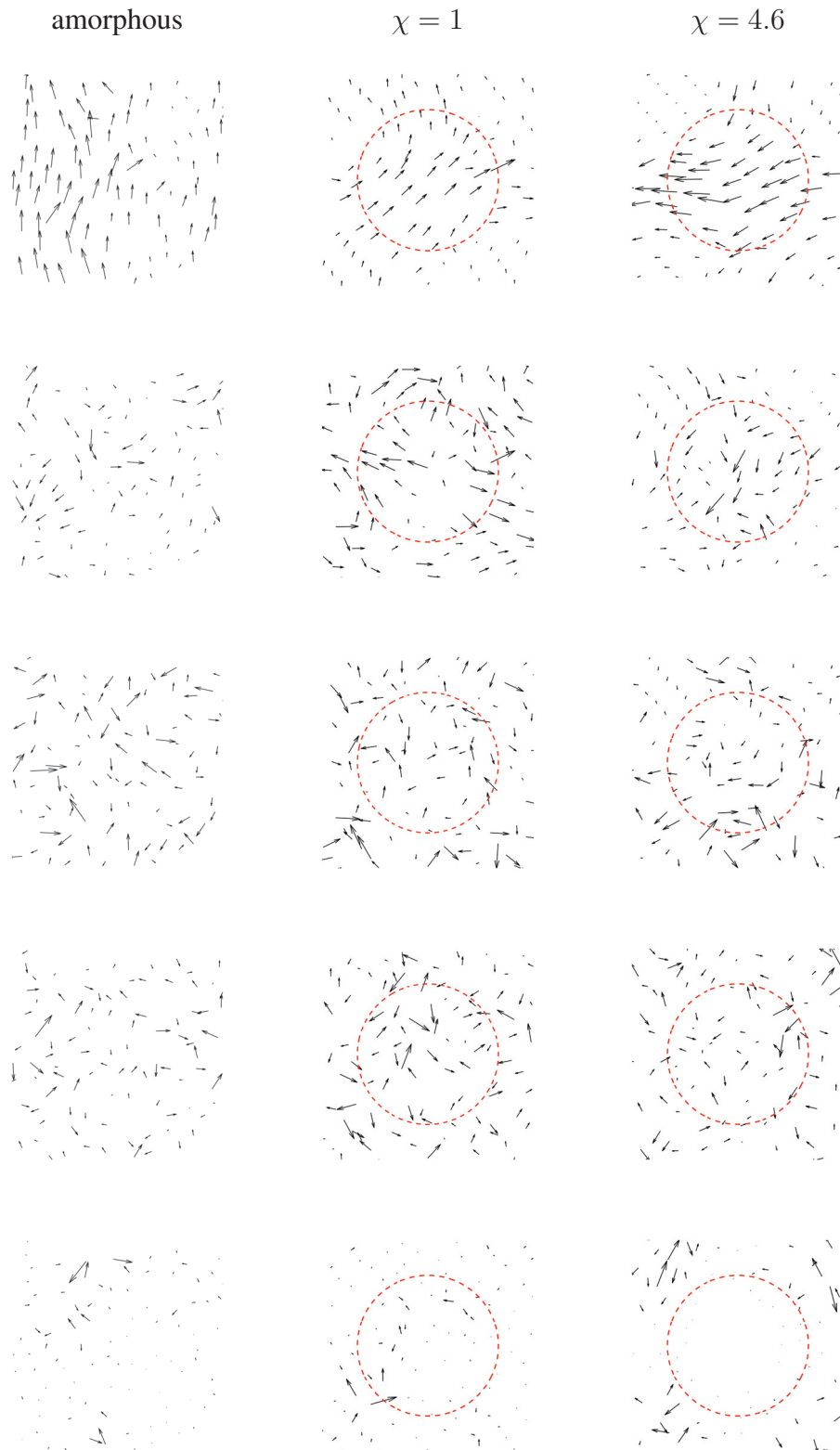


Figure 5.1: Example of modes of vibration for the amorphous and the two composite samples with $\chi = 1$ and $\chi = 4.6$. Each row corresponds to a given frequency in THz. 1st row: 1.15, 2nd row: 1.79, 3rd row: 6.21, 4th row: 10.27, 5th row: 17.84. The red dashed circles indicate the perimeter of the crystalline inclusion.

5.2 Dynamical Structure Factor

We present here the investigation of the dynamical structure factor in the same two composites with $\chi = 1$ and $\chi = 4.6$. In order to get rid of any size effect and to be able to access lower wave-vectors and thus energies, we have prepared relatively large samples. The amorphous box side was 60 Å, and the inclusion radius 25 Å, giving thus a crystalline volume fraction of 30 %.

Using the protocol described in Chapter 2, we have calculated the longitudinal and transverse dynamical structure factors at an effective temperature $T = 100$ K.

The intensity maps of the longitudinal and transverse dynamical structure factor is reported in Fig. 5.3 and Fig. 5.4 respectively for the two composites. It can already be seen in these intensity maps, that a clear longitudinal and transverse acoustic branch is visible for $\chi = 1$, while secondary, weaker branches appear for $\chi = 4.6$.

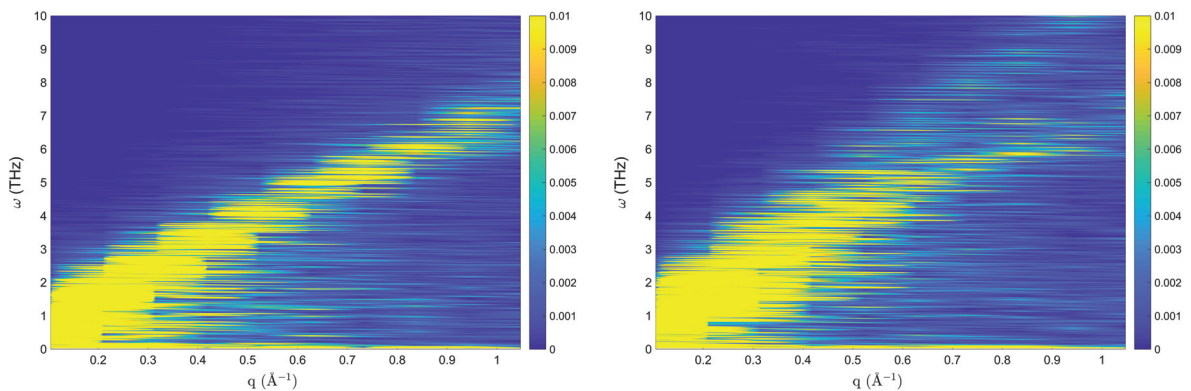


Figure 5.3: Intensity map of the longitudinal $S(q, \omega)$ in two composite samples with $\chi = 1$ (on the left) and $\chi = 4.6$ (on the right)

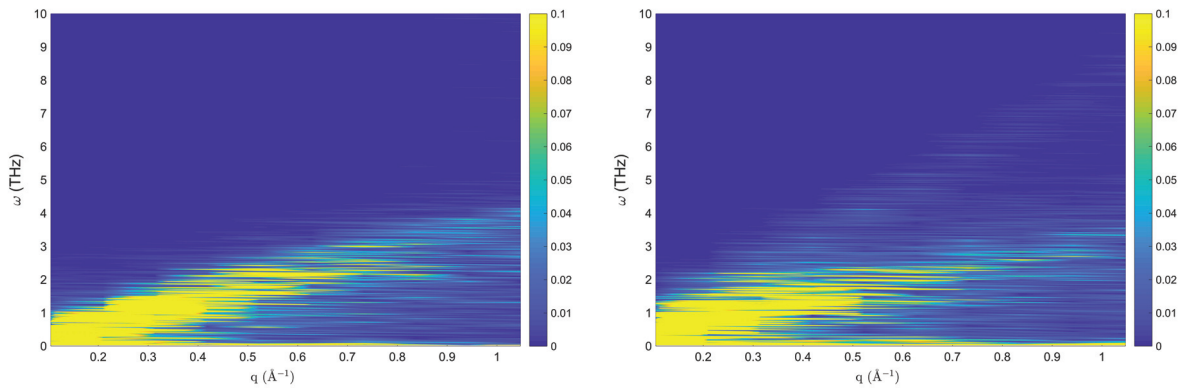


Figure 5.4: Intensity map of the transverse $S(q, \omega)$ in two composite samples with $\chi = 1$ (on the left) and $\chi = 4.6$ (on the right)

In order to treat these simulated data in a similar way to the one routinely used in IXS experiments, we have followed what was done in Damart et al [82]. We have first convoluted the data with an experimental resolution from the ID28 beamline of ESRF, corresponding to an incident energy of 23.7 keV. This has allowed us to get rid of the noise of the data and obtain well resolved peaks.

We have then fitted such peaks using the same fitting function as the one used for our experiments on metallic and chalcogenide glasses, made of a damped harmonic oscillator (DHO) model convoluted with

the instrument resolution. We have thus obtained longitudinal and transverse dispersions and attenuations.

5.2.1 Longitudinal Modes

The acoustic longitudinal modes for both rigidity contrasts $\chi = 1$ and $\chi = 4.6$ are shown in Fig. 5.5. In this figure, the modes intensity has been multiplied by the squared phonon energy for better visibility of higher frequency and much less intense phonons. The composite with $\chi = 1$ exhibits a well defined single phonon in the whole investigated q range, e.g. up to $q = 0.7 \text{ \AA}^{-1}$. In the sample with $\chi = 4.6$ instead, already for $q = 0.2 \text{ \AA}^{-1}$ the phonon is splitted into several modes, giving rise to an envelop which broadens as q increases, due to the different speed of sound of the single modes. Such spread of the phonon can be thought of as a loss of propagative character. Usually, it is agreed upon, that beyond the Ioffe-Regel limit the plane-wave phonon does not exist anymore, q is not a good quantum number anymore and the observed mode is in fact the superposition of many modes. In this sense, the spread of the phonon in many different phonons mimics what happens at the Ioffe-Regel limit in a glass, and marks the end of the propagative regime [174].

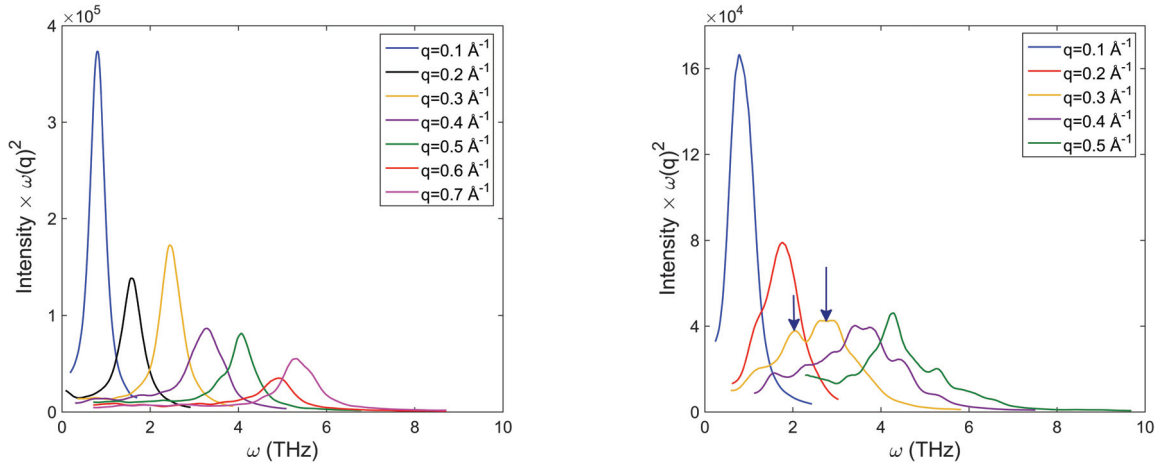


Figure 5.5: Longitudinal acoustic phonons in two composite samples with $\chi = 1$ (left panel) and $\chi = 4.6$ (right panel). As mentioned in the text, the intensity has been multiplied by the squared phonon energy for better visibility. The two arrows in the right panel indicate the most intense modes at $q=0.3 \text{ \AA}^{-1}$.

Fig. 5.6 reports the corresponding longitudinal acoustic dispersions, together with data from Damart et al [82] on a fully amorphous sample. It is important to mention here that the sample in Damart et al. was prepared in the same way as ours (from the box size and the atomic potential used to the calculations and data treatment of the $S(q,\omega)$).

From the figure we notice that the sample with $\chi = 1$ is in perfect agreement with the amorphous sample. This suggests that in the absence of rigidity contrast acoustic phonon energies are not perturbed by the inclusion, in agreement with our results on the DOS.

In the case of the sample with $\chi = 4.6$, we had to fit the data with several modes, sometimes up to 5 different modes. We have chosen to report here only the dispersion of the most intense two modes (as indicated by two arrows in Fig. 5.5), together with the position of the center of mass of the phonons envelop.

Surprisingly, the phonon here breaks up in slower and faster modes, but its center of mass has almost

the same dispersion than in the sample with $\chi = 1$, e.g. the one of the amorphous matrix.

From Ref. [173], we can estimate the change in longitudinal ($M = B + \frac{4}{3}G$) and transverse modulus (G) with χ . We find $\frac{M(\chi=4.6)}{M(\chi=1)} = 2.8$ and $\frac{G(\chi=4.6)}{G(\chi=1)} = 5$. Remembering that longitudinal and transverse sound velocities are defined as $v_L = \sqrt{M/\rho_M}$ and $v_T = \sqrt{G/\rho_M}$, with ρ_M the mass density, it will be $v_L(\chi = 4.6) = 1.7 v_L(\chi = 1)$ and $v_T(\chi = 4.6) = 2.2 v_T(\chi = 1)$.

Using the Reuss approximation for the homogenized calculation of the moduli [175, 176], for a crystalline fraction of 30%, we would expect $M_{eff} = (\frac{x}{M_c} + \frac{1-x}{M_a})^{-1}$, with M the longitudinal modulus, with subscript a or c for amorphous and crystalline phase, and x is the crystalline fraction. The same is true for the shear modulus. Using then the longitudinal and shear moduli for $\chi = 4.6$, and calling $v_{L/T}^a$ the longitudinal/transverse velocity of the amorphous matrix, we find for $x=30\%$ $v_L = 1.11v_L^a$ and $v_T = 1.14v_T^a$.

Such increase is obviously not reproduced by the center of mass of the envelop, which closely follows the phonon velocity in the amorphous sample, nor by all modes of the envelop, which present higher and lower velocities. The effective medium approach cannot thus reproduce anything of the observed phenomenology.

Fig. 5.7 reports the phonon broadening for the two samples, together with data on the amorphous sample from Damart et al [82]. Here the perfect agreement between our sample $\chi = 1$ and the amorphous one confirms once again that in absence of rigidity contrast the dynamics is fully determined by the matrix. This is quite interesting, as it means that the scattering from the interface, which would be expected to further decrease the phonon lifetime, has in fact no effect when there is no rigidity contrast. The story is different for the sample with $\chi = 4.6$. Here both the two most intense phonons present a much larger broadening, corresponding to a strong reduction of their lifetime. For $q > 0.1 \text{ \AA}^{-1}$, their lifetime is reduced by a factor of 2.

In order to quantify the information that the phonon is "single" for $\chi = 1$ but breaks up into an envelop of several modes for $\chi = 4.6$, we report in Fig. 5.8 the full width at half maximum of the phonon envelop for the two samples, without deconvolution from the instrument resolution. The dramatic increase of the envelop width in the $\chi = 4.6$ sample, corresponds to such breaking into phonons much slower and much faster than the ones of the amorphous matrix. All these observations suggest that heat transport is dramatically affected when a rigidity contrast is present.

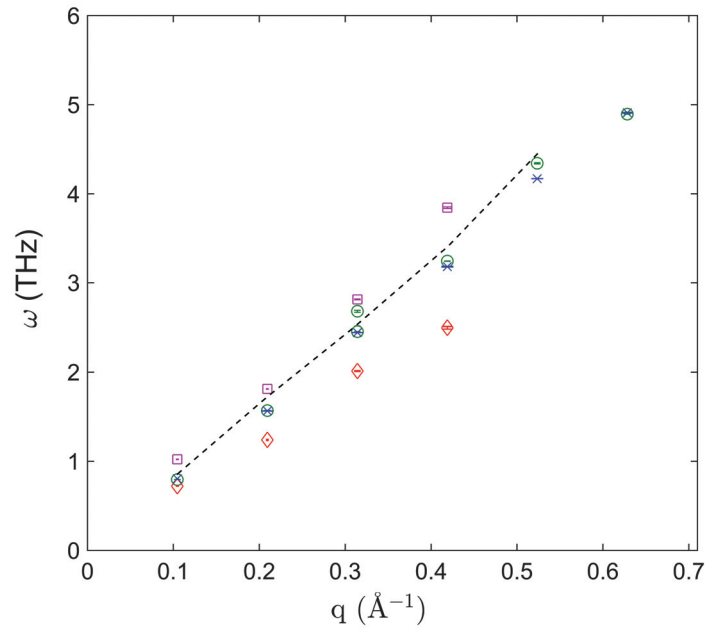


Figure 5.6: Longitudinal acoustic dispersion for our samples compared with literature data: composite with $\chi = 1$ (green circles), the two most intense modes for the composite with $\chi = 4.6$ (violet square and red diamond), data from T. Damart et al. [82] (blue stars). The dashed line represents the center of mass of the envelop of phonons for $\chi = 4.6$.

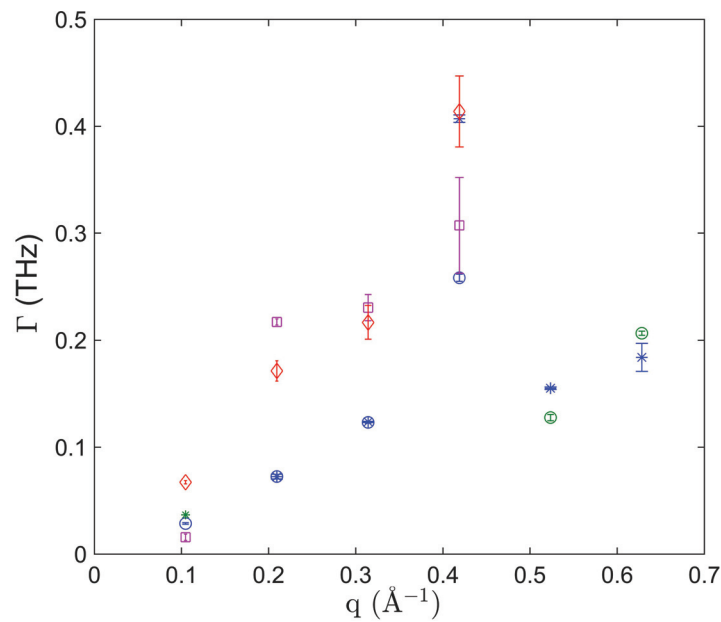


Figure 5.7: Longitudinal acoustic attenuation for our samples compared with literature data: composite with $\chi = 1$ (green circles), the two most intense modes for the composite with $\chi = 4.6$ (violet square and red diamond), data from T. Damart et al. [82] (blue stars).

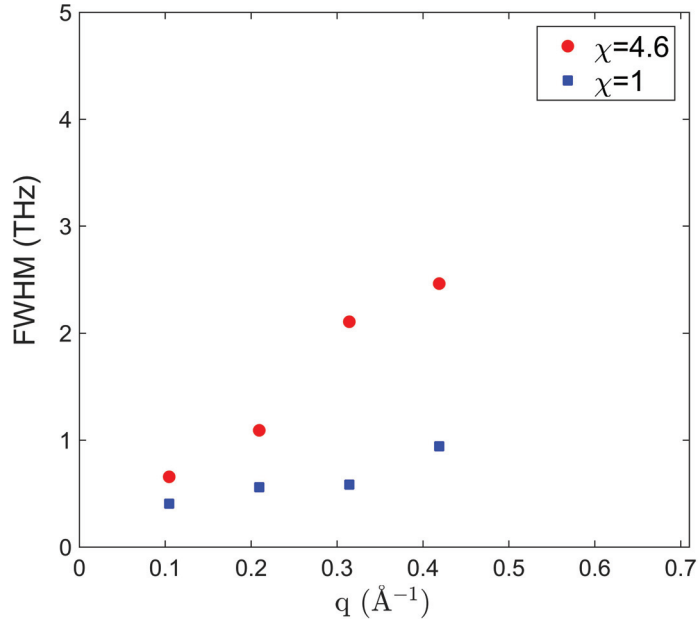


Figure 5.8: Full width at half maximum (FWHM) of the longitudinal phonon envelop as measured on the spectra convoluted with the instrumental resolution, in the two composite samples. As such, the FWHM is larger than the real envelop width, as there is still the broadening contribution from the experimental resolution.

5.2.2 Transverse Modes

Fig. 5.9 reports the acoustic transverse modes for both rigidity contrasts with $\chi = 1$ and $\chi = 4.6$. In both cases, we can observe well defined single phonons only up to $q = 0.4 \text{ \AA}^{-1}$. Beyond $q = 0.4 \text{ \AA}^{-1}$, the single mode breaks down in several modes in both samples.

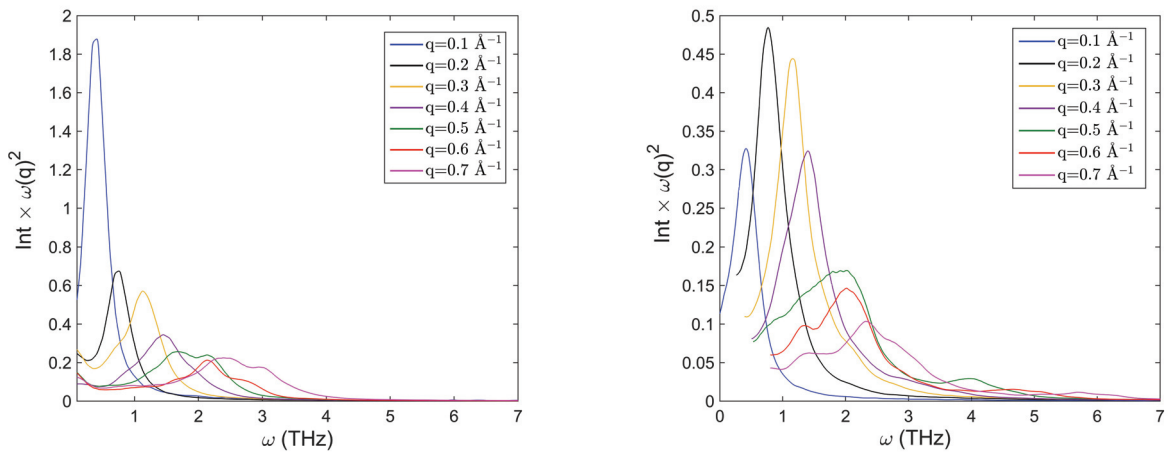


Figure 5.9: Transverse acoustic phonons in two composite samples with $\chi = 1$ (left panel) and $\chi = 4.6$ (right panel). As for longitudinal modes, the intensity has been multiplied by the squared phonon energy for better visibility.

The transverse acoustic dispersions are shown in Fig. 5.10. We report here for both samples only the dispersion of the most intense mode, together with the position of the center of mass of the phonons

envelop for $\chi = 4.6$. We report as well, as dashed and dotted lines, the most intense higher and lower energy modes in the phonon envelop for $q > 0.4 \text{ \AA}^{-1}$. Surprisingly, the dominant mode is the same in the two composites and follows the phonon in the amorphous phase. The two "side-modes" are very close to each other between the two composites, and have higher and lower speed of sound with respect to the dominant mode. Other, less intense, modes are present at higher and lower frequency. The rigidity contrast plays a role only at high energies: weak peaks with high energies up to 6 THz at $q = 0.7 \text{ \AA}^{-1}$ appear in the sample with $\chi = 4.6$, as it can be seen in Fig. 5.9.

We report in Fig. 5.11 the broadening of the dominant mode in the composites, compared with the phonon mode in the amorphous sample from Damart et al. [82]. The presence of an inclusion with no rigidity contrast does not affect the phonon lifetime, while for $\chi = 4.6$ a lifetime reduction of about a factor of 2 is observed for $q > 0.3 \text{ \AA}^{-1}$.

We follow now the width of the phonon envelop in the two composites without deconvolution from the instrument resolution as reported in Fig. 5.12. We observe that while at low q the behavior is very similar between the two composites, the envelop for $\chi = 4.6$ is clearly larger for $q > 0.4 \text{ \AA}^{-1}$.

It is important to notice that even in the fully amorphous sample a breaking of the transverse mode in an envelop of modes was reported at high q [82]. So, this breaking is not related to the inclusion, but does correspond to the crossing of the Ioffe-Regel limit in the amorphous matrix. The inclusion effect appears only in the composite with a rigidity contrast, which exhibits a larger envelop FWHM when such breaking takes place. It is worth underlying that when we calculate the FWHM of the envelop, we neglect the lower intensity modes, which are shifted to much higher and lower frequencies, and thus would even increase the envelop FWHM in the composite with $\chi = 4.6$.

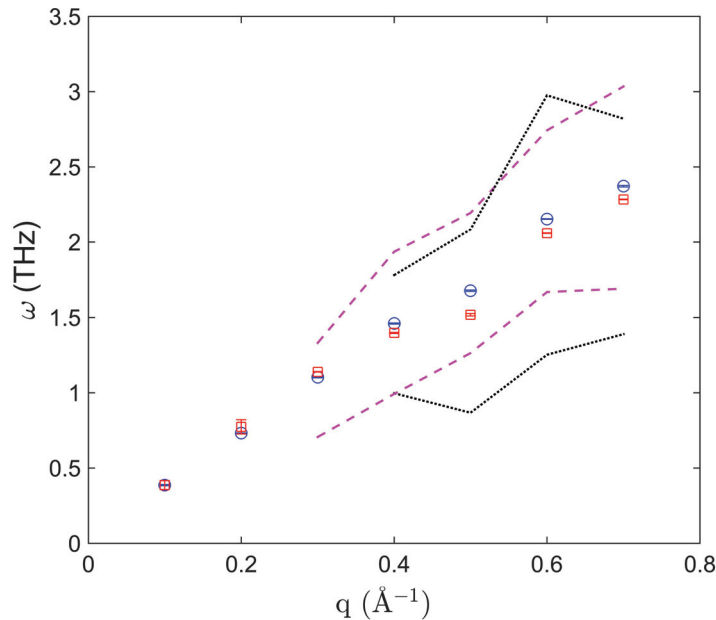


Figure 5.10: Transverse acoustic dispersion for the composite samples: $\chi = 1$ (blue circles) and $\chi = 4.6$ (red squares). The magenta dashed and black dotted lines denote the most intense higher and lower energy modes in the phonon envelop for $\chi = 1$ and $\chi = 4.6$, respectively

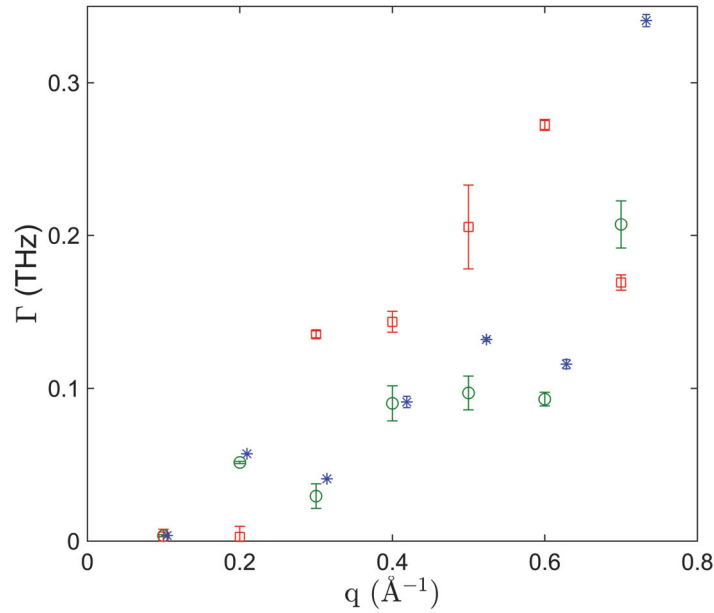


Figure 5.11: Transverse acoustic attenuation for the amorphous from Damart et al [82] (blue stars) and the composite samples with $\chi = 1$ (green circles) and $\chi = 4.6$ (red squares)

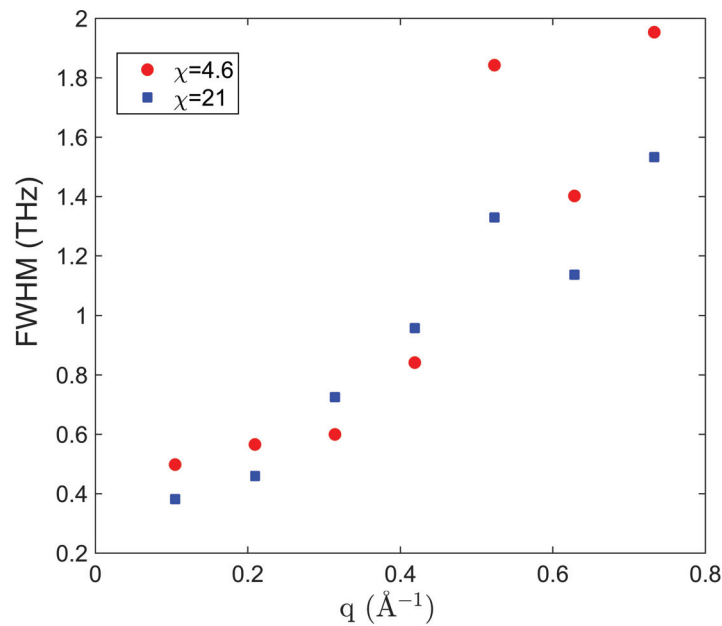


Figure 5.12: Full width at half maximum (FWHM) of the transverse phonon envelop as measured on the spectra convoluted with the instrumental resolution, in the two composite samples. As such, the FWHM is larger than the real envelop width, as there is still the broadening contribution from the experimental resolution.

5.2.3 Discussion

Summing up, we have seen different behaviors with the rigidity contrast in longitudinal and transverse phonons in the composites.

In absence of rigidity contrast, phonon dynamics is unperturbed: speed of sound and phonon damping

remain the same in the composite $\chi = 1$ with respect to the amorphous sample for both polarizations. In presence of a rigidity contrast, longitudinal dynamics is strongly perturbed as well: the single phonon breaks down in several modes since the smallest investigated q . Transverse dynamics however is very similar to the case $\chi = 1$, with no evident rigidity effect on the phonons dispersion. When looking at the dominant mode lifetime, the rigidity contrast reduces it by a factor of ~ 2 , for both polarizations. In both samples and polarizations therefore, dynamics remains dominated by the amorphous matrix, as the phonon envelop still moves on with the speed of sound determined by the amorphous sample, but the single phonon lifetime decreases of about a factor of 2 when the rigidity contrast increases by a factor of ~ 5 .

One can wonder where does the phonon splitting come from. As said, the breaking of the single mode in an envelop of modes was already reported in Damart et al [82] for the transverse polarization in the fully amorphous sample. This is likely the manifestation of the crossing of the Ioffe-Regel limit. The novelty in the composite with $\chi = 4.6$ is that the longitudinal mode splits as well in an envelop of modes, and this since the lowest q investigated, and the envelop generated by the transverse mode is much larger than in the composite without rigidity contrast. We can speculate that in presence of the inclusion, the splitting is larger because the amorphous phonon is projected onto new modes introduced by the inclusion, among the crystalline acoustic branches with different speeds of sound due to the elastic contrast.

Our observations thus suggest that the transport mechanism changes in presence of crystalline inclusions with high rigidity contrast due to a larger phonon splitting and single mode lifetime reduction. We would thus expect to observe a reduction of the thermal conductivity.

5.3 Propagation of a Wave-Packet

Successively, we have investigated the propagation of a longitudinal wave-packet centered at an energy of 5 THz, in the two composites, at 100 K. For this study we have chosen a box side of 60 Å, and a radius of the inclusion R of 10 and 25 Å, corresponding to crystalline volume fractions of 1.9 and 30% respectively. A series of 12 boxes aligned along the propagation direction has been used, in order to let the wave-packet well propagate without reflection effects from the end of the system.

First of all, we have followed the displacement of the wave-packet center of mass in the 4 systems ($R=10$ Å and $R=25$ Å with $\chi = 1$ and $\chi = 4.6$). We report it in Fig. 5.13: here it can be seen that for $R=10$ Å the center of mass position increases linearly with time whatever the value of χ , which corresponds to a propagation of the wave-packet. However, for $R=25$ Å and large rigidity contrast, the wave-packet is seen to move diffusively. We can analyze the propagation of the wave-packet at short times. Following the protocol described in Chapter 2, we calculate the repartition of the kinetic energy along the sample during the wave-packet propagation. The resulting kinetic energy envelopes are reported in Fig. 5.14 and Fig. 5.15 corresponding to the composites with inclusions radii $R=10$ Å and $R=25$ Å respectively. We fit the envelope of all energy profiles using the Beer-Lambert law [177], $E = A \exp(-x/l)$ where l is the mean free path of the wave-packet. All our results for the 4 systems are summarized in table 5.1.

	R=10 Å	R=25 Å
l (Å) for $\chi = 1$	594	477
l (Å) for $\chi = 4.6$	778	111

Table 5.1: Mean free path obtained from the fitting of the envelopes of propagating wave-packets with the Beer-Lambert Law for two composites with different radii and rigidity contrast (see text for details)

We notice that:

- For R=10 Å corresponding to a small inclusion volume fraction (1.9%), the phonon mean free path (MFP) l surprisingly increases by 30% from $\chi = 1$ to $\chi = 4.6$. As we don't see any reduction of l , as we would expect in case of an enhanced diffusion at the interface, we deduce that the inclusion is too small for giving a noticeable interface effect. The unexpected mean free path increase is likely related to the higher velocity of the longitudinal wave-packet in the composite with $\chi = 4.6$. Still, when we look at the velocity of the center of mass, we find that it increases only by 5% changing χ by a factor of 4.6. The wave-packet velocity alone cannot thus explain such MFP increase. At this stage, we don't have an explanation for it and further investigations are required.
- When the inclusion size increases giving rise to a larger volume fraction of crystal (30%) and in the absence of rigidity contrast, the MFP decreases by 24%. Such a crystalline fraction change would give, in the EMT approach, an increase of the sound velocity by 15%. The decrease of the MFP with the inclusion size is then due to a major importance of the interface, which is now able to scatter the wave-packet and reduce its lifetime, more than what would be in a fully amorphous sample.
This effect is more pronounced when $\chi = 4.6$ where the MFP decreases by a factor of 7, increasing the crystalline volume fraction, suggesting thus that the wave-packet is much more scattered at the interface in the presence of rigidity contrast.
- For R=25 Å, the effect is the most dramatic. Here we have 30% crystalline fraction and we find a decrease in l which approximately mimics the rigidity contrast increase, as it decreases by a factor of 4. In the case of $\chi = 4.6$, l corresponds in fact to an attenuation length, as the regime is totally diffusive. Using an EMT approach, we would expect a velocity increase of 34% with the rigidity contrast. Despite such higher velocity, the fact that l decreases indicates the presence of a strong interface scattering, dramatically decreasing the wave-packet lifetime.

We globally can conclude thus that the rigidity contrast plays indeed the major role, still the inclusion needs to be large enough for the interface to effectively scatter the wave-packet. At this point, we can wonder whether we can relate the results for the inclusion radius 25 Å to our results on the longitudinal dynamic structure factor reported in section 2 for the very same system. The longitudinal wave-packet with an energy of 5 THz corresponds to a longitudinal phonon with $q=0.6 \text{ \AA}^{-1}$. From the previous section, we know that at this q the single longitudinal phonon does not exist anymore in the $\chi = 4.6$ composite but is broken in an envelop of modes with higher and lower velocities. The single mode lifetime is reduced only by a factor of 2, which cannot explain the strong MFP reduction observed for the wave-packet here. However, when the phonon breaks into an envelop of modes, its energy is obviously spreaded all over them and will thus be carried with different velocities and in different directions, as

determined by the inclusion orientation. This is likely the real reason behind the strong reduction of the MFP of a propagating longitudinal wave-packet in presence of rigidity contrast.

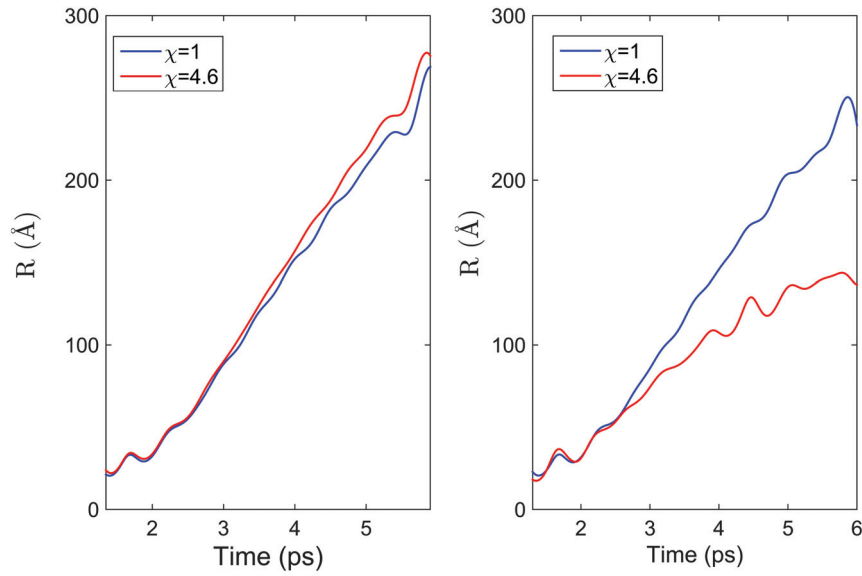


Figure 5.13: The center of mass $R(t)$ of a traveling wave-packet is reported as a function of time and rigidity contrast in a composite with an inclusion radius of 10 \AA (left) and $R=25 \text{ \AA}$ (right).

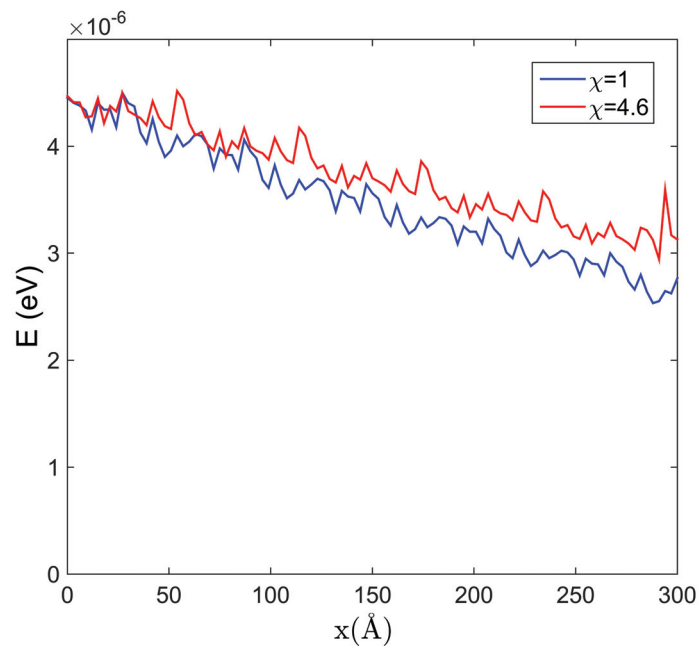


Figure 5.14: The evolution of the kinetic energy envelopes (E) along the direction x resulting from the propagation of waves in two composites with an inclusion radius $R=10 \text{ \AA}$ and different rigidity contrast.

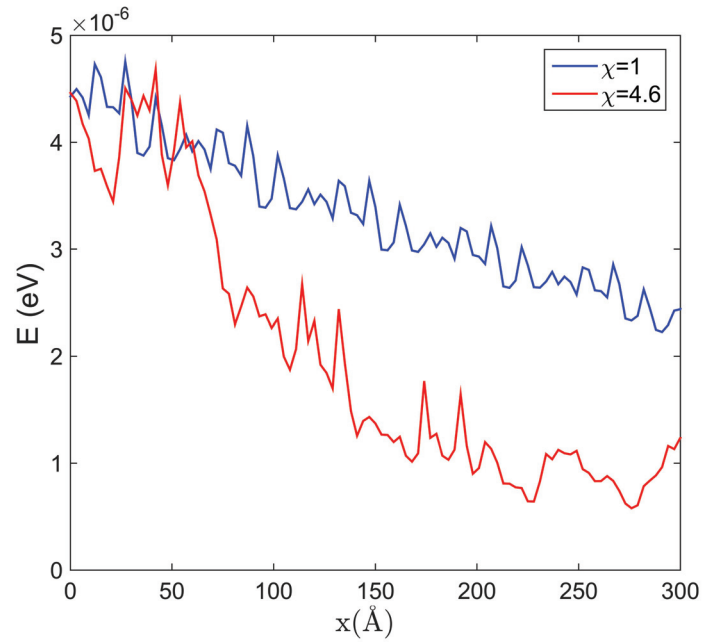


Figure 5.15: The evolution of the kinetic energy envelopes (E) along the direction x resulting from the propagation of waves in two composites with an inclusion radius $R=25 \text{ \AA}$ and different rigidity contrast.

5.4 Thermal conductivity

As described in chapter 2, we computed the thermal conductivity using the Green-Kubo formalism. The simulations were performed on composites made of a spherical inclusion embedded in a cubic amorphous matrix. As for the previous simulations, two rigidity contrasts have been investigated considering the case $\chi = 1$ and $\chi = 4.6$. In order to prepare samples with different crystalline fractions, we have modified both the box and inclusion sizes, the inclusion radius ranging from 5 to 30 \AA , and the box side from 30 to 100 \AA . One could wonder whether samples with different box sizes are comparable or whether finite size effects could appear in the smallest box. The consistency of all our results, independently on the box size, confirm that all data are indeed comparable and we don't have any finite size effect. This is consistent with Ref. [178], where a study of the thermal conductivity of amorphous silicon as a function of the box size has shown that the size effect is strong only for box size less than 30 \AA . Between 30 and 100 \AA , it is very weak, leading to an increase of k_T from 1.5 to 1.7 W/mK.

In Fig. 5.16, the thermal conductivity is plotted as a function of crystalline volume fraction at room temperature for the two configurations. The uncertainties are estimated by calculating the difference between the maximum and minimum values in the conductivity plateau. In the bulk amorphous sample, the thermal conductivity is $1.7 \pm 0.2 \text{ W K}^{-1} \text{ m}^{-1}$, which is in a good agreement with literature [179, 180]. Concerning the composite samples, the thermal conductivity increases linearly with the crystalline fraction for the two rigidity contrasts. Surprisingly, the rigidity contrast does not have any effect on the conductivity: the two curves exhibit indeed the same trend and are very close. We report in Fig. 5.17 the same data normalized to the amorphous thermal conductivity: here we can see that for a crystalline fraction of 43% the total change in the thermal conductivity is about 55% independently of the rigidity contrast.

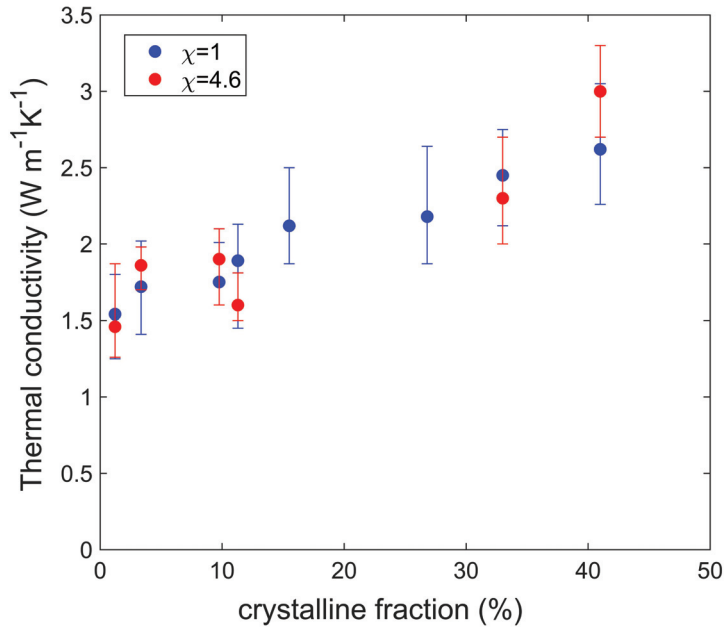


Figure 5.16: Thermal conductivity as a function of crystalline fraction, at room temperature

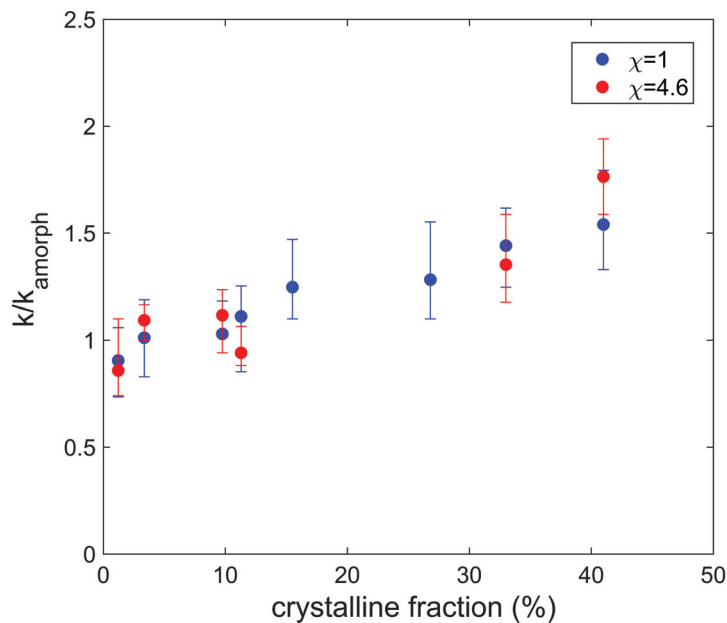


Figure 5.17: Thermal conductivity as reported in Fig. 5.16, normalized by the conductivity of the amorphous sample (k_{amorph}) plotted as a function of crystalline fraction, at room temperature

Generally speaking, we would expect two possible opposite cases:

- Due to the acoustic mismatch, the phonons lifetime should be reduced in the sample with $\chi = 4.6$, leading to a smaller thermal conductivity than in the sample with $\chi = 1$.
- Due to the increased speed of sound, the thermal conductivity in the sample with $\chi = 4.6$ should be higher than in the sample with $\chi = 1$.

We have seen that the DOS changes remarkably when the rigidity contrast is increased, even if only in the high frequency part of the vibrational spectrum. A slope change at low energy corresponds to a higher speed of sound in the composite with $\chi = 4.6$.

Concerning the speed of sound, when we look at our results on the dynamical structure factor $S(q, \omega)$, we see that in the sample with higher rigidity phonons lose very rapidly their propagative character, breaking down into an envelop of modes with different sound velocities, going from slower to faster with respect to the composite with no contrast. The envelop center of mass basically has the same speed of sound than in the amorphous sample. Concerning the single phonon lifetime, it strongly decreases in the sample with $\chi = 4.6$, and the propagative to diffusive crossover takes place much earlier than in the sample $\chi = 1$ and the amorphous alike, thus we would expect to see a thermal conductivity reduction in the sample with the higher rigidity contrast. It is true that the $S(q, \omega)$ simulations were carried out at low temperature ≈ 10 K, so that we do not have any certitude about expecting the same MFP reduction at room temperature. Still, it seems reasonable that the observed phonon lifetime reduction would hold at room temperature as well. It remains thus difficult to understand the lack of rigidity contrast in the results on the thermal conductivity when we look only to the acoustic dynamics.

We can instead understand it when we look at the relative acoustic and optic contributions to the thermal conductivity. Indeed, it has been reported ([180]) that the room temperature thermal conductivity in amorphous silicon is due to acoustic modes only for 30%, the main contribution coming from the diffusive optic modes. Therefore, even if the differences that we have observed on the acoustic modes propagation lead to different acoustic contributions, they will account only for 30% of the total thermal conductivity.

In presence of a diffusive transport mechanism, the thermal conductivity is not related to phonon lifetime or mean free path, but to the phonon diffusivity. We can thus understand our results assuming that the optic modes diffusivity is not strongly affected by the rigidity difference between the matrix and the inclusion.

We may expect to see a different behavior at low temperature, where optic modes are not thermally populated and the thermal conductivity only arises from acoustic modes. At this point, the effect of the rigidity contrast onto the phonon propagation will necessarily lead to an effect on the thermal conductivity. From Ref. [180] we see that already below $T = 100$ K the thermal conductivity is determined basically only by acoustic modes. Taking into account quantum effects in classical molecular dynamics simulations on disordered systems is however not trivial. Several techniques have been developed ([178, 180]), but we have not used them in this thesis work. This remains indeed as an interesting perspective of our study.

5.5 Summary

In this chapter, our results of numerical simulations of vibrational properties in composite systems have been presented. We have observed that the rigidity contrast causes a considerable modification of the vibrational density of states making evidence of the appearance of additional optic modes at high frequencies. In addition, our simulations of the dynamical structure factor and that of the propagation of a longitudinal wave-packet indicate that the sound velocity, the phonon lifetime and mean free path can be dramatically affected by the presence of a rigidity contrast between the inclusion and the amorphous matrix. Despite such strong effects reported in the acoustic dynamics, we don't have observed any effect of the rigidity contrast on the room temperature thermal conductivity. This is quite surprising, but could

be explained by the fact that at room temperature acoustic modes account for only 30% of the thermal conductivity. Future work should thus look at the effect of the rigidity contrast on optic modes and on their diffusivity in order to explain the thermal conductivity results, or to the thermal conductivity at low temperature. Indeed, acoustic dynamics dominates heat transport only at low temperature, $T < 100$ K. However, the calculation of the thermal conductivity at such temperatures requires the use of other molecular dynamics techniques, taking explicitly into account quantum effects.

Conclusion

This thesis presents a coupled experimental and theoretical investigation of the transport properties in amorphous/crystalline nanocomposites. Our work specifically focuses on the effect of the contrast of electric and elastic properties between the two phases on transport in the nanocomposite. To this aim, on the experimental side we have chosen 2 different composites, based on a metallic glass and a chalcogenide glass, going from no contrast to a great properties contrast. On the theoretical side, we have realized ideal silicon-based systems where we have artificially modified the elastic moduli of the crystalline nano-inclusion, from no contrast to a rigidity contrast of a factor of about 5.

All our results point to a relevant importance of the properties contrast, so that in absence of an important contrast of properties, electrical resistivity of the composite can be described by an effective medium theory, taking only into account the nanometric size of the crystalline grains, and phonon transport properties are essentially identical between the fully amorphous, fully nanocrystalline and composite samples. This is the case of the MG based composite, where the nanocrystalline grain nature of the fully crystalline sample, as well as the presence of minority crystalline phases, is responsible for an enhanced electron and phonon scattering, so that its electrical resistivity is only 20% smaller than in the glass, and its phonon attenuation is very similar.

As a consequence, we have found that the electrical resistivity linearly decreases from the glass to the polycrystal with no enhanced interface scattering effect. As for the phonon transport, we find that while phonon attenuation is not affected, the transverse velocity of the composite and the fully crystalline sample is higher than in the glass, on a macroscopic and mesoscopic lengthscale. Such shear hardening can be in fact related to the glass matrix structural relaxation, which takes place during the thermal protocol for preparing the composite. It affects thermal transport with an almost negligible increase of the vibrational component of only 2%.

More interesting is the case where there is contrast of properties between the two phases. This is the case of chalcogenide based composites. In particular, we have focused on carbon doped GeTe systems, GeTeC. Such system has allowed us to investigate two kinds of composites: the one made out of glassy GeTeC by partial crystallization, and the one represented by the fully crystallized GeTeC.

Indeed, during this thesis work, we have found out that crystallized GeTeC is in fact a nanocomposite made of core-shell nanograins: GeTe crystalline grains surrounded of amorphous carbon. As such, while the amorphous component is very small (a few percent in volume), it presents a huge contrast of properties between the two phases. The composite obtained by partial crystallization of GeTeC is still a composite with a good contrast of properties, as the electrical resistivity drops by orders of magnitude at the crystallization.

The core-shell nanoparticles composite is found to be the most interesting. Concerning electric transport,

we find that a metal-like to insulator-like transition takes place with the carbon addition, as a function of carbon content, which cannot be explained with the simple effective medium approach. Still, the Seebeck coefficient is apparently not affected by the carbon addition with respect to a pure GeTe polycrystalline film with larger grains. We have interpreted such observations as due to the electron localization at the amorphous grain boundaries, in agreement with many theoretical studies on nanocomposites and nanograins in polycrystalline chalcogenides. The lack of effect on the Seebeck coefficient is consistent with this picture, as its sensitivity to heterogeneities is reported to strongly depend on the potential barriers width and height at the grain boundaries.

Concerning thermal transport, the core-shell system has been reported to exhibit the same thermal conductivity as the fully amorphous GeTeC. This is extremely intriguing, and makes this system promising for thermoelectric applications, even if the Seebeck coefficient is unaffected by the nanostructuration. However, our results are in contradiction with such reports. Indeed, already the electronic contribution to thermal conductivity as calculated from our electric measurements, is larger than the reported total thermal conductivity, shedding thus a doubt on its reliability. Moreover, we have performed phonon measurements by inelastic x ray scattering and found that the phonon attenuation in a 30% crystallized sample is much larger than in the fully crystalline system. In this latter we are not measuring the intrinsic phonon broadening, due to the fact that we measure in fact a distribution of phonon branches, and thus the broadening of this latter. Still, we can assess an upper limit for the intrinsic phonon broadening, which results several times smaller than in the composite.

As the phonon broadening in the composite likely corresponds to a lower limit for the one in the fully amorphous sample, such result tells us that the core-shell system has phonons with much longer lifetime than the amorphous, and higher velocity as well. Our results point thus to a better vibrational thermal transport contribution than in the fully amorphous. As this is the conclusion from our electric data as well, we can only conclude that the thermal conductivity of the core-shell system is necessarily much larger than in the amorphous.

Concerning the electric properties of the second type of chalcogenide composite, the partially crystallized GeTeC, the electric transport is always insulator-like, with an increase of the insulating behavior with the amorphous content, as it can be expected.

Our experimental results can be fully understood at the light of our numerical simulations findings. Indeed we have found that in absence of rigidity contrast no effect is visible in the vibrational properties: phonon density of states, acoustic modes velocity and lifetime, are exactly the same as in the fully amorphous sample.

In presence of rigidity contrast we find that the vibrational dynamics is dramatically affected. Beside the mild changes of the density of states, both longitudinal and transverse phonons break down in an envelop of modes and the individual phonon lifetime is strongly reduced.

We can get a good insight on the changes in the thermal conductivity looking at the propagation of a phonon wave-packet in the system. For this, we have investigated the propagation of a longitudinal phonon wave-packet centered at 5 THz, with a wavelength smaller than the inclusion size. Here we can see that the introduction of the rigidity contrast dramatically affects the propagation of the wave-packet when the inclusion size is large enough to give rise to interface scattering. The mean free path is strongly reduced, and a diffusive regime appears in the wave-packet propagation. Unfortunately all these intriguing microscopic results do not reflect into a modified room temperature thermal conductivity, as simulated with the Green-Kubo formalism in composites with different volume fractions. We have understood such a lack of effects as probably due to the fact that at room temperature heat is mainly

assured by non propagating optic modes, while we have investigated only the acoustic dynamics, and only at low temperature.

The results obtained in the framework of this thesis have thus provided a combined macroscopic and microscopic point of view of the thermal and electronic transport in crystalline/amorphous nanocomposites.

Many aspects of this thesis require more investigations. In particular, an accurate measurement of thermal conductivity in crystalline GeTeC is necessary to solve the contradiction with our microscopic results and assess the potential of GeTeC for thermoelectricity. Furthermore, Hall mobility measurements in GeTeC would be needed in order to better understand the C-doping induced electronic localization. On the other hand, more work should be done in order to understand the effects of amorphous/crystalline heterogeneities on the Seebeck coefficient. In this perspective, theoretical investigations would be needed in order to shed more light on the role of the grain boundaries with tuning the geometry and size of energy barriers at crystalline/amorphous interfaces.

Beyond the specific systems here studied, the future experimental work should focus on the effect of the properties contrast on transport, spanning different systems, where the crystalline inclusions are not made of the same elements as the matrix. GeTeC represents indeed a first step in this direction, but the amorphous content is likely too small to really affect phonons. Larger C-contents should be thus investigated, despite the resistivity increase associated. Other systems, made ad hoc for getting strong contrast, are the natural continuation of this work, with inclusions harder and softer than the matrix, as well as more and less insulating.

Concerning our theoretical results, more numerical simulations require to be done, in particular thermal conductivity simulations at low temperature where we expect to see a considerable effect. As said in the manuscript, such calculations require corrections to the simulations, for taking into account the quantum effects for a reliable study at low temperature. The same kind of correction would allow to calculate the cumulative thermal conductivity and thus isolate the effects of the acoustic dynamics change onto thermal transport at room temperature as well.

During this thesis work, some trainees have started to investigate the same systems by finite elements modeling, which allows to simulate much larger systems, with very short simulation times. The first results on the propagation of a longitudinal wave-packet are in a very good agreement with ours.

This method will allow mapping the effect of rigidity contrast, inclusion size and spacial distribution on the propagation of a wave-packet much more rapidly than with molecular dynamics, then identifying the most interesting systems to be investigated with molecular dynamics for a microscopic view. This is indeed a very exciting perspective for the theoretical work.

Bibliography

- [1] C. A. Angell. Formation of glasses from liquids and biopolymers. *Science*, 267(5206):1924–1935, 1995.
- [2] P. G. Debenedetti and F. H. Stillinger. Supercooled liquids and the glass transition. *Nature*, 410:259, 2001.
- [3] H. Euchner, S. Pailhès, L. T. K. Nguyen, W. Assmus, F. Ritter, A. Haghighirad, Y. Grin, S. Paschen, and M. de Boissieu. Phononic filter effect of rattling phonons in the thermoelectric clathrate $\text{Ba}_8\text{Ge}_{40+x}\text{Ni}_{6-x}$. *Phys. Rev. B*, 86:224303, 2012.
- [4] P.-F. Lory, S. Pailhès, V. M. Giordano, H. Euchner, H. D. Nguyen, R. Ramlau, H. Borrmann, M. Schmidt, M. Baitinger, M. Ikeda, P. Tomes, M. Mihalkovic, C. Allio, M. R. Johnson, H. Schober, Y. Sidis, F. Bourdarot, L. P. Regnault, J. Ollivier, S. Paschen, Y. Grin, and M. de Boissieu. Direct measurement of individual phonon lifetimes in the clathrate compound $\text{Ba}_{7.81}\text{Ge}_{40.67}\text{Au}_{5.33}$. *Nat. Comm*, 8:491, 2017.
- [5] B. Allen and J. L. Feldman. *Phys. Rev. B*, 48:12581, 1993.
- [6] G. Baldi, V. M. Giordano, G. Monaco, F. Sette, E. Fabiani, A. Fontana, and G. Ruocco. Thermal conductivity and terahertz vibrational dynamics of vitreous silica. *Phys. Rev. B*, 77:214309, 2008.
- [7] R. C. Zeller and R. O. Pohl. Thermal conductivity and specific heat of noncrystalline solids. *Phys. Rev. B*, 4:2029, 1971.
- [8] W. A. Phillips. Two-level states in glasses. *Rep. Prog. Phys*, 50:1657, 1987.
- [9] U. Buchenau, N. Nucker, and A. J. Dianoux. Neutron scattering study of the low-frequency vibrations in vitreous silica. *Phys. Rev. Lett*, 53:2316, 1984.
- [10] S. N. Taraskin, Y. L. Loh, G. Natarajan, and S. R. Elliott. Origin of the boson peak in systems with lattice disorder. *Phys. Rev. B*, 86:1255, 2001.
- [11] W. Schirmacher. Thermal conductivity of glassy materials and the "boson peak". *Europhysics. Lett*, 73:892, 2006.
- [12] M. I. Klinger. Separation of soft-mode and acoustic dynamics in the boson peak of glasses: vast difference in high-pressure effects. *J. Non-Cryst. Solids*, 293-295:345–347, 2001.
- [13] V. L. Gurevich, D. A. Parshin, and H. R. Schober. Pressure dependence of the boson peak in glasses. *Phys. Rev. B*, 71:014209, 2005.

- [14] E. Duval, A. Boukenter, and T. Achibat. Vibrational dynamics and the structure of glasses. *J. Phys.: Cond. Matt*, 2:10227, 1990.
- [15] B. Rossi, G. Viliiani, E. Duval, L. Angelani, and W. Garber. Temperature-dependent vibrational heterogeneities in harmonic glasses. *Europhysics. Lett*, 71:256, 2005.
- [16] F. Leonforte, R. Boissie, A. Tanguy, J. P. Wittmer, and J. L. Barrat. Continuum limit of amorphous elastic bodies. iii. threedimensional systems. *Phys. Rev. B*, 72:224206, 2005.
- [17] F. Leonforte, A. Tanguy, J. P. Wittmer, and J. L. Barrat. Inhomogeneous elastic response of silica glass. *Phys. Rev. Lett*, 97:055501, 2006.
- [18] A.-I. Chumakov, G. Monaco, A. Fontana, A. Bosak, R.-P. Hermann, D. Bessas, B. Wehinger, W.-A. Crichton, M. Krisch, R. Ruffer, G. Baldi, G. Carini Jr., G. Carini, G. D'Ángelo, E. Gilioli, G. Tripodo, M. Zanatta, B. Winkler, V. Milman, K. Refson, M.-T. Dove, N. Dubrovinskaia, L. Dubrovinsky, R. Keding, and Y.-Z. Yue. Role of disorder in the thermodynamics and atomic dynamics of glasses. *Phys. Rev. Lett*, 112:025502, 2014.
- [19] T. Otomo, M. Arai, Y. Inamura, J.-B. Suck, S. Bennington, and K. Suzuki. Observation of collective excitations in the amorphous alloy $\text{Ni}_{67}\text{Zr}_{33}$. *J. Non-Cryst. Solids*, 613:232, 1998.
- [20] T. Scopigno, J.-B. Suck, R. Angelini, F. Albergamo, and G. Ruocco. High-frequency dynamics in metallic glasses. *Phys. Rev. Lett*, 96:135501, 2006.
- [21] G. Monaco and V. M. Giordano. Breakdown of the debye approximation for the acoustic modes with nanometric wavelengths in glasses. *PNAS*, 106:3659, 2009.
- [22] G. Baldi, V. M. Giordano, G. Monaco, and B. Ruta. Sound attenuation at terahertz frequencies and the boson peak of vitreous silica. *Phys. Rev. Lett.*, 104:195501, 2010.
- [23] B. Ruta, G. Baldi, V. M. Giordano, F. Scarponi, D. Fioretto, and G. Monaco. Acoustic excitations in glassy sorbitol and their relation with the fragility and the boson peak. *J. Chem. Phys.*, 137:214502, 2012.
- [24] G. Monaco and S. Mossa. Anomalous properties of the acoustic excitations in glasses on the mesoscopic length scale. *PNAS*, 106(40):16907, 2009.
- [25] H. Mizuno, S. Mossa, and J.-L. Barrat. Measuring spatial distribution of the local elastic modulus in glasses. *Phys. Rev. E*, 87:042306, 2013.
- [26] H. Mizuno, S. Mossa, and J.-L. Barrat. Elastic heterogeneity, vibrational states, and thermal conductivity across an amorphisation transition. *EPL*, 104:56001, 2013.
- [27] H. Mizuno, S. Mossa, and J.-L. Barrat. Acoustic excitations and elastic heterogeneities in disordered solids. *PNAS*, 111:11949–11954, 2014.
- [28] H. Mizuno, S. Mossa, and J.-L. Barrat. Beating the amorphous limit in thermal conductivity by superlattices design. *Sci. Rep*, 5:14116, 2015.
- [29] T. Ichitsubo, S. Hosokawa, K. Matsuda, E. Matsubara, N. Nishiyama, S. Tsutsui, and A. Q. R. Baron. Nanoscale elastic inhomogeneity of a pd-based metallic glass: Sound velocity from ultrasonic and inelastic x-ray scattering experiments. *Phys. Rev. B*, 76:140201, 2007.

- [30] T. Ichitsubo, W. Itaka, E. Matsubara, H. Kato, S. Biwa, S. Hosokawa, K. Matsuda, J. Saida, O. Haruyama, Y. Yokoyama, H. Uchiyama, and A. Q. R. Baron. Elastic inhomogeneity and acoustic phonons in pd-, pt-, and zr-based metallic glasses. *Phys. Rev. B*, 81:172201, 2010.
- [31] U. Mizutani, M. Tanaka, and H. Sato. Studies of negative TCR and electronic structure of non-magnetic metallic glasses based on y and la. *Journal of Physics F: Metal Physics*, 17:131–141, 1987.
- [32] U. Mizutani. Electron transport properties of non-magnetic metallic glasses. *Materials Science and Engineering*, 99:165–173, 1988.
- [33] U. Mizutani. *Introduction to the electron theory of metals*. Cambridge University Press, 2001.
- [34] NF. Mott. Conduction in glasses containing transition metal ions. *Journal of Non-Crystalline Solids*, 1:1, 1968.
- [35] N. F. Mott. Localized states in a pseudogap and near extremities of conduction and valence bands. *Philosophical Magazine*, 19(160):835, 1969.
- [36] M. H. Cohen, H. Fritzsche, and S. R. Ovinsky. Simple band model for amorphous semiconducting alloys. *Phys. Rev. Lett*, 22(20):1065, 1969.
- [37] M. Kastner, D. Adler, and H. Fritzsche. Valence-alternation model for localized gap states in lone-pair semiconductors. *Phys. Rev. B*, 37:1504, 1976.
- [38] R. M. Hill. Poole-frenkel conduction in amorphous solids. *Philosophical magazine*, 23:59–86, 1971.
- [39] D. Ielmini. Analytical model for subthreshold conduction and threshold switching in chalcogenide-based memory devices. *J. Appl. Phys*, 102:054517, 2007.
- [40] J. Frenkel. On pre-breakdown phenomena in insulators and electronic semi-conductors. *Phys. Rev*, 54:647, 1938.
- [41] Octavi E. Semonin, Joseph M. Luther, Sukgeun Choi, Hsiang-Yu Chen, Jianbo Gao, Arthur J. Nozik, and Matthew C. Beard. Peak external photocurrent quantum efficiency exceeding 100% via meg in a quantum dot solar cell. *Science*, 334(6062):1530–1533, 2011.
- [42] C. Fan and A. Inoue. Improvement of mechanical properties by precipitation of nanoscale compound particles in Zr-Cu-Pd-Al amorphous alloys. *Materials transactions*, 38(12):1040–1046, 1997.
- [43] K. Hajlaoui, A.R. Yavari, A. LeMoulec, W.J. Botta, F.G. Vaughan, J. Das, A.L. Greer, and A. K. Kvick. Plasticity induced by nanoparticle dispersions in bulk metallic glasses. *Journal of Non-Cryst. Solids*, 353:327–331, 2007.
- [44] S-W. Lee, M-Y. Huh, E. Fleury, and J-C. Lee. Crystallization-induced plasticity of Cu-Zr containing bulk amorphous alloys. *Acta Materialia*, 54:349–355, 2006.
- [45] H. Chen, Y. He, G. J. Shiflet, and S. J. Poon. Mechanical properties of partially crystallized Aluminum based metallic glasses. *Scripta Metallurgica et Materialia*, 25:1421, 1991.

- [46] Y. H. Kim, A. Inoue, and T. Masumoto. Ultrahigh tensile strengths of $\text{Al}_{88}\text{Y}_2\text{Ni}_9\text{M}_1$ (M=Mn or Fe) amorphous alloys containing finely dispersed fcc-Al particles. *Mater. Trans. JIM*, 31:747, 1990.
- [47] W. Liu, X. Yana, G. Chen, and Z. Rena. Recent advances in thermoelectric nanocomposites. *Nano Energy*, 1:42–56, 2012.
- [48] Z. Wang, J. E. Alaniz, W. Jang, J. E. Garay, and C. Dames. Thermal conductivity of nanocrystalline silicon: Importance of grain size and frequency-dependent mean free paths. *Nano. Lett.*, 11:2206, 2011.
- [49] Y. Nakamura, M. Isogawa, T. Ueda, S. Yamasaka, H. Matsui, J. Kikkawa, S. Ikeuchi, T. Oyake, T. Hori, J. Shiomi, and A. Sakai. Anomalous reduction of thermal conductivity in coherent nanocrystal architecture for silicon thermoelectric material. *Nano. Energy*, 12:845–851, 2015.
- [50] A. Miura, S. Zhou, T. Nozaki, and J. Shiomi. Crystalline-amorphous silicon nanocomposites with reduced thermal conductivity for bulk thermoelectrics. *Applied Materials and Interfaces*, 7:13484–13489, 2015.
- [51] T.J. Zhu, F. Yan, X.B. Zhao, S. N. Zhang, Y. Chen, and S. H. Yang. Preparation and thermoelectric properties of bulk in situ nanocomposites with amorphous/nanocrystal hybrid structure. *J. Phys. D: Appl. Phys.*, 40:6094–6097, 2007.
- [52] K. Pietrak and T. S. Wisniewski. A review of models for effective thermal conductivity of composite materials. *Journal of Power Technology*, 95(1):14–24, 2015.
- [53] W. J. Abbe. A note on the kapitza resistance. *Nuovo Cimento*, 56:187, 1968.
- [54] D. Checke and H. Ettinger. The kapitza resistance and phonon reflectivity between solids and liquid helium. *Journal of Low Temperatures Physics*, 36:121–137, 1979.
- [55] W. Eisenmenger. *Phonon Scattering in Condensed Matter V*, volume p. 194. Springer, 1986.
- [56] H. Y. Bai, C. Z. Tong, and P. Zheng. Electrical resistivity in $\text{Zr}_{48}\text{Nb}_8\text{Cu}_{12}\text{Fe}_8\text{Be}_{24}$ glassy and crystallized alloys. *Journal of Applied Physics*, 95(3):1269, 2004.
- [57] Y. K. Kuo, K. M. Sivakumar, C. A. Su, C. N. Ku, S. T. Lin, A. B. Kaiser, J. B. Qiang, Q. Wang, and C. Dong. Measurement of low-temperature transport properties of Cu-based Cu-Zr-Ti bulk metallic glass. *Phys. Rev. B*, 74:014208, 2006.
- [58] J. Z. Jiang, W. Roseker, C. S. Jacobsen, and G. F. Goya. Low-temperature electrical resistivity of as-cast glassy, relaxed, and crystallized $\text{Pd}_{40}\text{Cu}_{30}\text{Ni}_{10}\text{P}_{20}$ alloys. *J. Phys. Cond. Matter*, 15:8713–8718, 2003.
- [59] D. Z. Hu, X. M. Lu, J. S. Zhu, and F. Yan. Study on the crystallization by an electrical resistance measurement in $\text{Ge}_2\text{Sb}_2\text{Te}_5$ and N-doped $\text{Ge}_2\text{Sb}_2\text{Te}_5$ films. *J. Appl. Phys.*, 102:1135507, 2007.
- [60] J. B. Vaney, G. Delaizir, E. Alleno, O. Rouleau, A. Piarristeguy, J. Monnier, C. Godart, M. Ribes, R. Escalier, A. Pradel, A. P. Gonçalves, E. B. Lopes, G. J. Cuello, P. Ziolkowski, E. Muller, C. Candolfi, A. Dauscher, and B. Lenoira. A comprehensive study of the crystallization of Cu-As-Te glasses: microstructure and thermoelectric properties. *Journal of Materials Chemistry A*, 1:8190, 2013.

- [61] J. Lingner, M. Letz, and G. Jakob. SrTiO₃ glass-ceramics as oxide thermoelectrics. *J. Mater. Sci*, 48:2812–2816, 2013.
- [62] M. Jost, J. Lingner, M. Letz, and G. Jakob. Thermoelectric properties of p-type Bi₂Sr₂Ci₂O₉ glass-ceramics. *Semicond. Sci. Technol*, 29:124011, 2014.
- [63] S.V. Novikov, A.T. Burkov, and J. Schumann. Enhancement of thermoelectric properties in nanocrystalline M-Si thin film composites (M = Cr, Mn). *Journal of Alloys and Compounds*, 557:239–243, 2013.
- [64] A.T. Burkov, S.V. Novikov, V.V. Khovaylo, and J. Schumann. Energy filtering enhancement of thermoelectric performance of nanocrystalline Cr_{1-x} Si_x composites. *Journal of Alloys and Compounds*, 691:89–94, 2017.
- [65] B. Liu, N. Zuo, and F. Ye. Abnormal change of electrical resistivity in the Cu₄₆Zr₄₆Al₈ bulk metallic glass during crystallization. *Materials Letters*, 171:285–288, 2016.
- [66] Y. C. Dou, X. Y. Qin, D. Li, L. L. Li, T. H. Zou, and Q. Q. Wang. Enhanced thermopower and thermoelectric performance through energy filtering of carriers in (Bi₂Te₃)_{0.2}(Sb₂Te₃)_{0.8} bulk alloy embedded with amorphous SiO₂ nanoparticles. *J. Appl. Phys*, 114:044906, 2013.
- [67] R. Landauer. The electrical resistance of binary metallic mixtures. *J. Appl. Phys.*, 23(7):779, 1952.
- [68] S. Gravier, P. Donnadieu, S. Lay, B. Doisneau, F. Bley, L. Salvo, and J.J. Blandin. Evaluation of the crystal volume fraction in a partially nanocrystallized bulk metallic glass. *Journal of Alloys and Compounds*, 504:226–229, 2010.
- [69] E. G. Fu, J. Carter, M. Martin, G. Xie, X. Zhang, Y.Q. Wang, R. Littleton, S. McDeavitt, and L. Shao. Ar-ion-milling-induced structural changes of Cu₅₀Zr₄₅Ti₅ metallic glass. *Nuclear Instruments and Methods in Physics Research B*, 268:545, 2010.
- [70] D. Nagahama, T. Ohkubo, T. Mukai, and K. Hono. Characterization of nanocrystal dispersed Cu₆₀Zr₃₀Ti₁₀ metallic glass. *Materials Transactions*, 46(6):1264, 2005.
- [71] T. Brink, M. Peterlechner, H. Risner, K. Albe, and G. Wilde. Influence of crystalline nanoprecipitates on shear-band propagation in Cu-Zr-based metallic glasses. *Phys. Rev. B*, 5:054005, 2016.
- [72] E. Alleno. Mesure des coefficients de transport thermique et électrique dans les matériaux thermoélectriques massifs : principes et pratiques. *Ecole thématique "Thermoélectricité" - Carcans-Maubuisson*, 2008.
- [73] CC Williams and HK Wickramasinghe. Scanning thermal profiler. *Applied Physics Letters*, 49:1587, 1986.
- [74] B. Cretin, S. Gomes, N. Trannoy, and P. Vairac. *Scanning thermal microscopy, Microscale and nanoscale heat transfer*, volume 107. Springer, 181-238 edition, 2007.
- [75] S. Gomès, A. Assy, and P-O. Chapuis. Scanning thermal microscopy: A review. *Phys. Status Solidi A*, 212(3):477, 2015.

- [76] <http://www.esrf.eu/UsersAndScience/Experiments/DynExtrCond/ID28/BeamlineLayout>.
- [77] L. Verlet. Computer "experiments" on classical fluids. i. thermodynamical properties of lennard-jones molecules. *Physical Review B*, 159(1):98, 1967.
- [78] Frank H. Stillinger and Thomas A. Weber. Computer simulation of local order in condensed phases of silicon. *Physical Review B*, 31(8):5262–5271, 1985.
- [79] L. Pizzagalli, J. Godet, J. Guérolé S. Brochard, E. Holmstrom, K. Nordlund, and T. Albaret. A new parametrization of the stillinger-weber potential for an improved description of defects and plasticity of silicon. *Journal of Physics: Condensed Matter*, 25(5):055801, 2013.
- [80] Neil W. Ashcroft and N. David Mermin. *Solid state physics*. 1976.
- [81] Y. M. Beltukov, V. I. Kozub, and D. A. Parshin. The ioffe-regel criterion and diffusion of vibrations in random lattices. *Physical Review B*, 87:134203, 2013.
- [82] T. Damart, V. M. Giordano, and A. Tanguy. Nanocrystalline inclusions as a low-pass filter for thermal transport in a-si. *Physical Review B*, 92:094201, 2015.
- [83] P. K. Schelling, S. R. Phillpot, and P. Keblinski. Comparison of atomic-level simulation methods for computing thermal conductivity. *Physical Review B*, 65(14):144306, 2002.
- [84] K. Termentzidis and S. Merabia. Molecular dynamics simulations and thermal transport at the nano-scale. *Intech Editor*.
- [85] R. Kubo. The fluctuation-dissipation theorem. *Reports on Progress in Physics*, 29(1):255, 1966.
- [86] A. Inoue. Stabilization of metallic supercooled liquid and bulk amorphous alloys. *Acta Mat.*, 48:279–306, 2000.
- [87] C. A. Schuh, T. C. Hufnagel, and U. Ramamurty. Mechanical behavior of amorphous alloys. *Acta Mat.*, 55:4067–4109, 2007.
- [88] W.H. Wang, C. Dong, and C.H. Shek. Bulk metallic glasses. *Materials Science and Engineering R*, 44:45–89, 2004.
- [89] W. Klement, R. H. Willens, and P. Duwez. Non-crystalline structure in solidified gold-silicon. *Nature*, 187:869–870, 1960.
- [90] A. Inoue, K. Ohtera, K. Kita, and T. Masumoto. New amorphous Mg-Ce-Ni alloys with high strength and good ductility. *Japanese Journal of Applied Physics*, 27:2248–2251, 1988.
- [91] A. Inoue, T. Zhang, and T. Masumoto. Zr-Al-Ni amorphous alloys with high glass transition temperature and significant supercooled liquid region. *Materials Transactions*, 31:177, 1990.
- [92] A. L. Peker and W. L. Johnson. A highly processable metallic glass: $Zr_{41.2}Ti_{13.8}Cu_{12.5}Ni_{10}Be_{22.5}$. *Appl. Phys. Lett*, 63:2342, 1993.
- [93] A. Inoue, N. Nishiyama, and H. M. Kimura. Preparation and thermal stability of bulk amorphous $Pd_{40}Cu_{30}Ni_{10}P_{20}$ alloy cylinder of 72 mm in diameter. *Mater. Trans. JIM*, 38:179, 1997.

- [94] A. Inoue, T. Zhang, and T. Itoi. New Fe-Co-Ni-Zr-B amorphous alloys with wide supercooled liquid regions and good soft magnetic properties. *Mater. Trans. JIM*, 38:359, 1997.
- [95] M. Yamasaki, S. Kagao, Y. Kawamura, and K. Yoshimura. Thermal diffusivity and conductivity of supercooled liquid in $Zr_{41}Ti_{14}Cu_{12}Ni_{10}Be_{23}$ metallic glass. *Appl. Phys. Lett.*, 84(23):4653, 2004.
- [96] U. Harms, T. D. Shen, and R. B. Schwarz. Thermal conductivity of $Pd_{40}Ni_{40-x}Cu_xP_{20}$ metallic glasses. *Scripta Materialia*, 47:411–414, 2002.
- [97] R. Y. Umetsu, R. Tu, and T. Goto. Thermal and electrical transport properties of Zr-based bulk metallic glassy alloys with high glass-forming ability. *Materials Transactions*, 53(10):1721–1725, 2012.
- [98] J.I. Langford and A.J.C. Wilson. Scherrer after sixty years: A survey and some new results in the determination of crystallite size. *J. Appl. Cryst.*, 11:102–113., 1978.
- [99] Z. Zhou, C. Uher, D. Xu, W. L. Johnson, W. Gannon, and M. C. Aronson. On the existence of Einstein oscillators and thermal conductivity in bulk metallic glass. *Appl. Phys. Lett.*, 89:031924, 2006.
- [100] P. J. Cote and L. V. Meisel. *Electrical Transport in Glassy Metals*, volume 46 of *Topics in Applied Physics*. Springer, 1981.
- [101] H. Gleiter. Nanocrystalline materials. *Progress in Materials Science*, 33:223–315, 1989.
- [102] V. M. Giordano and G. Monaco. Fingerprints of order and disorder on the high-frequency dynamics of liquids. *PNAS*, 107:21985, 2010.
- [103] A. Bosak, M. Krisch, I. Fischer, S. Huotari, and G. Monaco. Inelastic x-ray scattering from polycrystalline materials at low momentum transfer. *Phys. Rev. B Condens. Matter Mater. Phys.*, 75:064106, 2007.
- [104] T. Ichitsubo, H. Kato, E. Matsubara, S. Biwa, S. Hosokawa, K. Matsuda, H. Uchiyama, and A.Q.R. Baron. Static heterogeneity in metallic glasses and its correlation to physical properties. *J. Non-Cryst. Sol.*, 357(2):494–500, 2011.
- [105] D. Crespo, P. Bruna, A. Valles, and E. Pineda. Phonon dispersion relation of metallic glasses. *Phys. Rev. B*, 94:144205, 2016.
- [106] M. Idriss, F. Célarié, Y. Yokoyama, F. Tessier, and T. Rouxel. Evolution of the elastic modulus of Zr-Cu-Al BMGs during annealing treatment and crystallization: Role of Zr/Cu ratio. *J. Non-Cryst. Sol.*, 421:35–40, 2015.
- [107] G. E. Abrosimova, N. P. Kobelev, E. L. Kolyvanov, and V. A. Khonik. The influence of heat treatment on the ultrasonic velocity and elastic moduli of a Zr-Cu-Ni-Al-Ti bulk metallic glass. *Physics of the Solid State*, 46(10):1859–1862, 2004.
- [108] G. E. Abrosimova, N. P. Kobelev, E. L. Kolyvanov, V. A. Khonik., V. M. Levin, and Yu. S. Petronyuk. Effect of heat treatment on the elastic characteristics of a bulk amorphous Zr-Cu-Ni-Al-Ti alloy. *Physics of the Solid State*, 48(11):2091–2094, 2006.

- [109] H. F. Poulsen, J. A. Wert, J. Neuefeind, V. Honkimaki, and M. Daymond. Measuring strain distributions in amorphous materials. *Nat. Mat.*, 4:33, 2005.
- [110] T. C. Hufnagel and R. T. Ott. Structural aspects of elastic deformation of a metallic glass. *Phys. Rev. B*, 73:064204, 2006.
- [111] Charles Kittel. *Introduction to Solid State Physics*. 1996.
- [112] B. Rufflé, M. Foret, E. Courtens, R. Vacher, and G. Monaco. Observation of the onset of strong scattering on high frequency acoustic phonons in densified silica glass. *Phys. Rev. Lett.*, 90:095502, 2003.
- [113] B. Rufflé, G. Guimbretière, E. Courtens, R. Vacher, and G. Monaco. Glass-specific behavior in the damping of acousticlike vibrations. *Phys. Rev. Lett.*, 96:045502, 2006.
- [114] Y. Li, P. Yu, and H. Y. Bai. Study on the boson peak in bulk metallic glasses. *J. Appl. Phys.*, 104:013520, 2008.
- [115] M. Wuttig and N. Yamada. Phase-change materials for rewriteable data storage. *Nat. Mat.*, 6:824, 2007.
- [116] T. Tuma, A. Pantazi, M. Le Gallo, A. Sebastian, and E. Eleftheriou. Stochastic phase-change neurons. *Nature Nanotechnology*, 11:693, 2016.
- [117] N. Yamada, E. Ohno, N. Akahira, K. Nishiuchi, K. Nagata, and Masatoshi Takao. High-speed overwritable phase-change optical disk material. *Jpn. J. Appl. Phys.*, 26:61–66, 1987. Part 1.
- [118] S. Raoux. Phase change materials. *Annu. Rev. Mater. Res.*, 39:25–48, 2009.
- [119] J. Orava, A. L. Greer, B. Gholipour, D.W. Hewak, and C. E. Smith. Characterization of supercooled liquid $\text{Ge}_2\text{Sb}_2\text{Te}_5$ and its crystallization by ultrafast-heating calorimetry. *Nat. Mat.*, 11:279, 2012.
- [120] G.C. Sosso, G. Miceli, S. Caravati, F. Giberti, J. Behler, and M. Bernasconi. Fast crystallization of the phase change compound GeTe by large scale molecular dynamics simulations. *J. Phys. Chem. Lett.*, 4:4241–4246, 2013.
- [121] D. Lencer, M. Salinga, B. Grabowski, T. Hickel, J. Neugebauer, and M. Wuttig. A map for phase-change materials. *Nat. Mat.*, 7:972, 2008.
- [122] D. Lencer, M. Salinga, and Matthias Wuttig. Design rules for phase-change materials in data storage applications. *Adv. Mater.*, 23(18):2030–2058, 2011.
- [123] S. Caravati and M. Bernasconi. Coexistence of tetrahedral- and octahedral-like sites in amorphous phase change materials. *Appl. Phys. Lett.*, 91:171906, 2007.
- [124] A. V. Kolobov, P. Fons, A. I. Frenkel, A. L. Ankudinov, J. Tominaga, and T. Uruga. Understanding the phase-change mechanism of rewritable optical media. *Nat. Mater.*, 3:703–708, 2004.
- [125] S. Kohara, K. Kato, S. Kimura, H. Tanaka, T. Usuki, K. Suzuya, H. Tanaka, Y. Moritomo, T. Matsunaga, N. Yamada, Y. Tanaka, H. Suematsu, and M. Takata. Structural basis for the fast phase change of $\text{Ge}_2\text{Sb}_2\text{Te}_5$: Ring statistics analogy between the crystal and amorphous states. *Appl. Phys. Lett.*, 89:201910, 2006.

- [126] T. Nonaka, G. Ohbayashi, Y. Toriumi, Y. Mori, and H. Hashimoto. Crystal structure of GeTe and $\text{Ge}_2\text{Sb}_2\text{Te}_5$ meta-stable phase. *Thin Solid Films*, 370:258–261, 2000.
- [127] T. Chattopadhyay, J. X. Boucherlet, and H. G. Von Schnering. Neutron diffraction study on the structural phase transition in GeTe. *J. Phys.C: Solid Phys*, 20:1431, 1987.
- [128] J-L. F. Da Silva, A. Walsh, and H. Lee. Insights into the structure of the stable and metastable $(\text{GeTe})_m(\text{Sb}_2\text{Te}_3)_n$ compounds. *Phys. Rev B*, 78:224111, 2008.
- [129] A. V. Kolobov and J. Tominaga. Local structure of crystallized GeTe films. *Appl. Phys. Lett*, 82:382, 2003.
- [130] A. V. Kolobov, P. Fons, J. Tominaga, A. I. Frenkel, A. L. Ankudinov, S. N. Yannopoulos, K. S. Andrikopoulos, and T. Uruga. Why phase-change media are fast and stable: A new approach to an old problem. *Jpn. J. Appl. Phys., Part 1*, 44:3345, 2005.
- [131] G. B. Beneventi, E. Gourvest, A. Fantini, L. Perniola, V. Sousa, S. Maitrejean, J.C. Bastien, A. Bastard, A. Fargeix, B. Hyot, C. Jahan, J.F. Nodin, A. Persico, D. Blachier, A. Toffoli, S. Loubriat, A. Roule, S. Lhostis, H. Feldis, G. Reibold T. Billon, B. De Salvo, L. Larcher, P. Pavan, D. Bensahel, P. Mazoyer, R. Annunziata, and F. Boulanger. On carbon doping to improve GeTe-based phase-change memory data retention at high temperature. *IEEE International Memory Workshop*, pages 1–4, 2010.
- [132] U. D. Wdowik, K. Parlinski, S. Rols, and T. Chatterji. Soft-phonon mediated structural phase transition in GeTe. *Phys. Rev. B*, 89:224306, 2014.
- [133] E.F. Steigmeier and G. Harbeke. Soft phonon mode and ferroelectricity in GeTe. *Solid State Comm*, 8:1275–1279, 1970. Pergamon Press.
- [134] P. Fons, A. V. Kolobov, M. Krbal and J. Tominaga, K. S. Andrikopoulos, S. N. Yannopoulos, G. A. Voyiatzis, and T. Uruga. Phase transition in crystalline GeTe: Pitfalls of averaging effects. *Phys. Rev. B*, 82:155209, 2010.
- [135] G. E. Ghezzi, J. Y. Raty, S. Maitrejean, A. Roule, E. Elkaim, and F. Hippert. Effect of carbon doping on the structure of amorphous GeTe phase change material. *Appl. Phys. Phys. Lett*, 99:151906, 2011.
- [136] R. Fallica, E. Varesi, L. Fumagalli, S. Spadoni, M. Longo, and C. Wiemer. Effect of nitrogen doping on the thermal conductivity of GeTe thin films. *Phys. Status Solidi RRL*, 7(12):1107–1111, 2013.
- [137] J.Y Raty, P. Noé, G. Ghezzi, S. Maitrejean, C. Bichara, and F. Hippert. Vibrational properties and stabilization mechanism of the amorphous phase of doped GeTe. *Phys.Rev B*, 88:014203, 2013.
- [138] G. B. Beneventi, L. Perniola, V. Sousa, E. Gourvest, S. Maitrejean, J.C. Bastien, A. Bastard, B. Hyot, A. Fargeix, C. Jahan, J.F. Nodin, A. Persico, A. Fantini, D. Blachier, A. Toffoli, S. Loubriat, A. Roule, S. Lhostis, H. Feldis, G. Reibold, T. Billon, B. De Salvo, L. Larcher, P. Pavan, D. Bensahel, P. Mazoyer, R. Annunziata, P. Zuliani, and F. Boulanger. Carbon-doped GeTe: A promising material for phase-change memories. *Solid-State Electronics*, 65-66:197–204, 2011.

- [139] E. Gourvest. *Développement et élaboration par MOCVD de matériaux à changement de phase é base d'alliages GeTe: applications aux mémoires embarquées par la microélectronique*. PhD thesis, Université de Grenoble, 2010.
- [140] A. Kusiak, J.L. Battaglia, P. Noé, V.Sousa, and F. Fillot. Thermal conductivity of carbon doped GeTe thin films in amorphous and crystalline state measured by modulated photo thermal radiometry. *Journal of Physics: Conference Series*, 745:032104, 2016.
- [141] J. H. Park, S.-W. Kim, J. H. Kim, Z. Wu, S. L. Cho, D. Ahn, D. H. Ahn, J. M. Lee, S. U. Nam, and D.-H. Ko. Reduction of reset current in phase change memory devices by carbon doping in GeSbTe films. *J. Appl. Phys*, 117:115703, 2015.
- [142] Y. G. Fedorenko, M. A. Hughes, J. L. Colaux, C. Jeynes, R. M. Gwilliam, K. P. Homewood, J. Yao, D. W. Hewak, T-H. Lee, S. R. Elliott, B. Gholipour, and J. Curry. Electrical properties of amorphous chalcogenide/silicon heterojunctions modified by ion implantation, 2014.
- [143] K. L. Chopra and S. K. Bahl. Thermopower behavior of amorphous versus crystalline Ge and GeTe films. *Thins Solid Films - Elsevier Sequoia S. A, Lausanne*, page 211, 1972.
- [144] D. Ielmini. Threshold switching mechanism by high-field energy gain in the hopping transport of chalcogenide glasses. *Phys. Rev. B*, 78:035308, 2008.
- [145] G. C. Vezzoli, P. J. Walsh, and L. W. Doremus. Threshold switching and the on-state in non-crystalline chalcogenide semiconductors: An interpretation of threshold-switching research. *Journal of Non-Crystalline Solids*, 18:333–373, 1975.
- [146] A. E. Owen and J. M. Robertson. Electronic conduction and switching in chalcogenide glasses. *IEEE Transaction on Electron Devices*, 20:105, 1973.
- [147] K. E. Petersen and D. Adler. A model for the on state of amorphous chalcogenide threshold switches. *J. Appl. Phys*, 50:925, 1979.
- [148] J. A. V. Diosdado, P. Ashwin, K. I. Kohary, and C. D. Wright. Threshold switching via electric field induced crystallization in phase-change memory devices. *Appl. Phys. Lett*, 100:253105, 2012.
- [149] F. Zipoli, D. Krebs, and A. Curioni. Structural origin of resistance drift in amorphous GeTe. *Phys. Rev B*, 93:115201, 2016.
- [150] M. Boniardi, D. Ielmini, S. Lavizzari, A. L. Lacaita, A. Redaelli, and A. Pirovano. Statistics of resistance drift due to structural relaxation in phase-change memory arrays. *IEEE Transactions on Electron Devices*, 57(10):2690–2696, 2010.
- [151] A.H. Edwards, A.C. Pineda, P.A. Schultz, M.G. Martin, A.P. Thompson, and H.P. Hjalmarson. Electronic structure of intrinsic defects in crystalline germanium telluride. *Phys.Rev B*, 73:045210, 2006.
- [152] S. K. Bahl and K. L. Chopra. Amorphous versus crystalline GeTe films. ii. optical properties. *J.Appl.Phys*, 40:4940, 1969.

- [153] Y. Gelbstein, O. Ben-Yehuda, E. Pinhas, T. Edrei, Y. Sadia, Z. Dashevsky, and M.P. Dariel. Thermoelectric properties of (Pb,Sn,Ge)Te-based alloys. *Journal of ELECTRONIC MATERIALS*, 38(7):1478, 2009.
- [154] J. L. Bosse, M. Timofeeva, P. D. Tovee, B. J. Robinson, B. D. Huey, and O. V. Kolosov. Nanothermal characterization of amorphous and crystalline phases in chalcogenides thin films with scanning thermal microscopy. *J. Appl. Phys*, 116:134904, 2014.
- [155] R. Lan, R. Endo, M. Kuwahara, Y. Kobayashi, and M. Susa. Electrical and heat conduction mechanisms of GeTe alloy for phase change memory application. *J. Appl. Phys*, 112:053712, 2012.
- [156] K. S. Andrikopoulos, S. N. Yannopoulos, G. A. Voyiatzis, A. V. Kolobov, M. Ribes, and J. Tomimaga. Raman scattering study of the a-GeTe structure and possible mechanism for the amorphous to crystal transition. *J. Phys. Condens. Matter*, 18:965–979, 2006.
- [157] P. B. Pereira, I. Sergueev, S. Gorsse, J. Dadda, Ec. Muller, and R. P. Hermann. Lattice dynamics and structure of GeTe, SnTe and PbTe. *Phys. Status. Solidi B*, 250(7):1300–1307, 2013.
- [158] D. Campi, L. Paulatto and G. Fugallo, F. Mauri, and M. Bernasconi. First-principles calculation of lattice thermal conductivity in crystalline phase change materials: Gete, sb2te3, andge2sb2te5. *Phys. Rev B*, 95:024311, 2017.
- [159] J. R. Sootsman, Duck Y. Chung, and M. G. Kanatzidis. New and old concepts in thermoelectric materials. *Angewandte Chemie International Edition*, 48(46):8616–8639, 2009.
- [160] S. Gorsse, P. Bauer Pereira, R. Decourt, and E. Sellier. Microstructure engineering design for thermoelectric materials: An approach to minimize thermal diffusivity. *Chem. Mater*, 22:988–993, 2010.
- [161] Y. Rosenberg, Y. Gelbstein, and M. P. Dariel. Phase separation and thermoelectric properties of the $\text{Pb}_{0.25}\text{Sn}_{0.25}\text{Ge}_{0.5}\text{Te}$ compound. *J. Alloys. Compd*, 526:3138, 2012.
- [162] J. Schwan, S. Ulrich, V. Batori, and H. Ehrhardt. Raman spectroscopy on amorphous carbon films. *J. Appl. Phys*, 80:440, 1996.
- [163] M. Iwaki. Estimation of the atomic density of amorphous carbon using ion implantation, SIMS and RBS. *Surface and Coatings Technology*, 158-159:377–381, 2002.
- [164] J.-B. Vaney, A. Piarristeguy, V. Ohorodniichuck, O. Ferry, A. Pradel, E. Alleno, J. Monnier, E. B. Lopes, A. P. Goncalves, G. Delaizir, C. Candolfi, A. Dauscher, and B. Lenoir. Effective medium theory based modeling of the thermoelectric properties of composites: Comparison between predictions and experiments in the glass-crystal composite system $\text{Si}_{10}\text{As}_{15}$. *Journal of Materials Chemistry C*, 3:11090–11098, 2015.
- [165] T. Siegrist, P. Jost, H. Volker, M. Woda, P. Merkelbach, C. Schlockermann, and M. Wuttig. Disorder-induced localization in crystalline phase-change materials. *Nat. Mat*, 10:202, 2011.
- [166] P. Nukala, R. Agarwal, X. Qian, M. H. Jang, S. Dhara, K. Kumar, A. T. C. Johnson, J. Li, and R. Agarwal. Direct observation of metal-insulator transition in single-crystalline germanium telluride nanowire memory devices prior to amorphization. *Nano. Letters*, 14:2201–2209, 2014.

- [167] P. Nukala, C-C. Lin, R. Composto, and R. Agarwal. Ultralow-power switching via defect engineering in germanium telluride phase-change memory devices. *Nat. Comm*, 7(10482), 2016.
- [168] D. Narducci, E. Selezneva, G. Cerofolini, S. Frabboni, and G. Ottaviani. Impact of energy filtering and carrier localization on the thermoelectric properties of granular semiconductors. *Journal of Solid State Chemistry*, 193:19–25, 2012.
- [169] J. H. Mooij. Electrical conduction in concentrated disordered transition metal alloys. *Phys. Stat. Sol*, 17:521–530, 1973.
- [170] M. A. Park, K. Savran, and Y.-J. Kim. Weak localization and the Mooij rule in disordered materials. *Phys. Stat. Sol*, 237:500–506, 2003.
- [171] H-S. Kim, Z. M. Gibbs, Y. Tang, H. Wang, and G. J. Snyder. Characterization of Lorenz number with Seebeck coefficient measurement. *APL Materials*, 3:041506, 2015.
- [172] J.-Y. Raty. *Private communication*.
- [173] T. Albaret C. Fusco and A. Tanguy. Role of local order in the small-scale plasticity of model amorphous materials. *Phys. Rev. E*, 82:066116, 2010.
- [174] S. N. Taraskin and S. R. Elliott. Determination of the ioffe-regel limit for vibrational excitations in disordered materials. *Philosophical Magazine B*, 79(11-12):1747–1754, 1999.
- [175] B. Qi, J. Absi, and N. Tessier-Doyen. Experimental and numerical study of the Young’s modulus vs temperature for heterogeneous model materials with polygonal inclusions. *Computational Materials Science*, 46:996–1001, 2009.
- [176] Salvatore Torquato. *Random heterogeneous materials: microstructure and macroscopic properties*. Springer Science & Business Media, 2013.
- [177] D. F. Swinehart. The beer-lambert law. *Journal of Chemical Education*, 39(7):333, 1962.
- [178] K. Sääskilahti, J. Oksanen, J. Tulkki, A. J. H. McGaughey, and S. Volz. Vibrational mean free paths and thermal conductivity of amorphous silicon from non-equilibrium molecular dynamics simulations. *AIP Advances*, 6:121904, 2016.
- [179] J. M. Larkin and A. J. H. McGaughey. Thermal conductivity accumulation in amorphous silica and amorphous silicon. *Phys. Rev. B*, 89:144303, 2014.
- [180] W. Lv and A. Henry. Direct calculation of modal contributions to thermal conductivity via green-kubo modal analysis. *New J. Phys*, 18:013028, 2016.

L'effet d'une nanocrystallisation partielle sur les propriétés de transport dans les composites amorphe/cristal

Les besoins technologiques toujours grandissants dans la société moderne suscitent la nécessité de développer des matériaux multifonctionnels innovants. Ceci est vrai surtout dans des domaines de pointe, tels que la microélectronique et la conversion d'énergie, où on demande aux matériaux de limiter la dissipation de chaleur tout en ayant de bonnes propriétés électroniques.

L'optimisation d'un tel type de matériaux est toutefois complexe: une forte réduction de la conductivité thermique se fait en général aux dépenses de la conductivité électrique. Une stratégie qui a été récemment introduite est de développer des matériaux hétérogènes à l'échelle nanométrique, dits "nanocomposites". Malgré le potentiel dont ils ont déjà fait preuve, à ce jour la compréhension fondamentale de leurs propriétés reste encore limitée.

Dans cette thèse nous présentons une étude fondamentale des propriétés de transport dans des composites basés sur une matrice amorphe contenant des inclusions cristallines de tailles nanométriques, afin d'acquérir une compréhension microscopique des mécanismes en jeu.

Pour ce faire, nous avons effectué une étude expérimentale dans deux composites intermétalliques, un verre métallique et un verre chalcogénure, obtenus par cristallisation directe du verre. Nous avons pu mettre en évidence un comportement fortement dépendant du contraste de propriétés entre la matrice vitreuse et les inclusions cristallines. Nos conclusions ont trouvé confirmation dans des simulations numériques par dynamique moléculaire que nous avons effectué sur des systèmes modèles, qui ont en effet permis de mettre en évidence l'effet d'un contraste de rigidité sur les propriétés vibrationnelles de ce type de composite.

The effect a partial nanocrystallization on the transport properties of amorphous/crystalline composites

Face to the growing technological needs in the modern society, the need has arisen of developing novel multifunctional materials, able to simultaneously assure different functions.

This is especially important in advanced technologies, such as microelectronics and energy harvesting, where heat dissipation reduction is essential, while keeping good electrical properties.

Optimizing such materials represents however a challenging task: lowering thermal conductivity generally implies lowering the electrical conductivity as well. A new strategy has recently aroused consisting in exploiting heterogeneous materials at the nanoscale, so-called "nanocomposites". Despite their great potential, the fundamental understanding of their properties is still lacking.

In this thesis, we present a fundamental investigation of the transport properties in composites made of nano-inclusions embedded in an amorphous matrix, aimed to get a microscopic insight into the mechanisms ruling transport in such materials.

To this purpose, we have carried on an experimental study in two intermetallic composites, based on a metallic glass and a chalcogenide glass, where crystalline inclusions were directly obtained from the glass temperature-induced recrystallization.

We find that transport behavior is strongly dependent on the properties contrast between the amorphous matrix and the crystalline inclusions.

Our findings are comforted by our theoretical results, obtained by molecular dynamics simulations on a model composite system, which highlight the effect of the rigidity contrast on the vibrational properties of such material, and thus on thermal transport.